



HAL
open science

Airborne wind energy system : Control and experimentation

Yashank Gupta

► **To cite this version:**

Yashank Gupta. Airborne wind energy system : Control and experimentation. Automatic. Université Grenoble Alpes, 2018. English. NNT : 2018GREAT094 . tel-02113723v1

HAL Id: tel-02113723

<https://theses.hal.science/tel-02113723v1>

Submitted on 29 Apr 2019 (v1), last revised 28 May 2019 (v2)

HAL is a multi-disciplinary open access archive for the deposit and dissemination of scientific research documents, whether they are published or not. The documents may come from teaching and research institutions in France or abroad, or from public or private research centers.

L'archive ouverte pluridisciplinaire **HAL**, est destinée au dépôt et à la diffusion de documents scientifiques de niveau recherche, publiés ou non, émanant des établissements d'enseignement et de recherche français ou étrangers, des laboratoires publics ou privés.

THÈSE

pour obtenir le grade de

**DOCTEUR DE LA COMMUNAUTÉ UNIVERSITÉ
GRENOBLE ALPES**

Spécialité : **Automatique-Productique**

Arrêté ministériel : le 6 janvier 2005 – 25 mai 2016

Présentée par

Yashank GUPTA

Thèse dirigée par **Dr. Ahmad Hably** et
Co-dirigée par **Jonathan Dumon**

Préparée au sein du

**Laboratoire GRENOBLE IMAGES PAROLE SIGNAL
AUTOMATIQUE (GIPSA-LAB)**

dans **L'ECOLE DOCTORALE ELECTRONIQUE,
ELECTROTECHNIQUE, AUTOMATIQUE, TRAITEMENT DU
SIGNAL (EEATS)**

Magnus Based Airborne Wind Energy Systems

Thèse soutenue publiquement le **29 novembre 2018**,
devant le jury composé de:

M. Frederic BOYER, Président

Professeur, IMT Atlantique Bretagne-Pays de la Loire, Nantes, France

M. Alexandre TROFINO, Rapporteur

Professeur, Universidade Federal de Santa Catarina,
Florianópolis, Brazil

M. Lorenzo FAGIANO, Rapporteur

Professore Associato, Politecnico di Milano, Milan, Italy

M. Mazen ALAMIR, Examineur

Directeur de Recherche, CNRS, France

M. Ahmad HABLY, Directeur de Thèse

Maître de Conférences, Grenoble-INP, Grenoble, France

M. Jonathan DUMON, Co-directeur de Thèse

Ingénieur d'études, CNRS, Grenoble, France



Dedicated to Mummy and Papa,

ACKNOWLEDGEMENT

My Ph.D. journey started on 16th November 2015. This bittersweet journey had been one of the most intriguing and challenging experience of my life so far. I believe the past three years have not only provided me more clarity but also have bestowed upon me the most intangible insights that would help me steer through this ocean of life. It definitely was, is, and will be a turning point in my life. This journey would not have been possible without the inherent support of my parents. I would like to thank my mum and dad from the deepest core of my heart for their constant support and their belief in me. I thank my lovely sister, for being a part of my life and her amazing will and support.

I would like to thank Ahmad, my supervisor, for offering me this position. I would also like to thank Jonathan, my co-supervisor, without his guidance and support this thesis wouldn't have been possible. Discussions with him, his help and perseverance is the sole reason this thesis work was able to take its current form and shape. From him, I have learned lessons which I would always cherish all my life.

Like the twist and turns of a hilly road, no journey is complete without its share of sun and shade. On this path, I met some amazing people, forged some of the strongest bonds. I would like to thank Miguel, my best buddy in this journey, for being brutally rational, illogically logical and a good shepherd. The two years spent sitting next to him and his friendship made this journey much more fun. The cliched routine discussions about almost everything gave this PhD journey its cliched meaning. Agathe, was another star of this journey, her unusual, weird, adventurous, and sometimes dangerous liaisons added flavor to my otherwise lame days sitting next to Miguel. As she put it correctly we are three musketeers. Swann and Roserio, two of the bluntest person I have ever met. I shall miss the cigarettes with Swann and Bruno. I shall miss our outrageous, out of the world, deeply disturbing, indecent and beyond the realm of politically incorrect, humor and afternoon conversations in the lab. The time spent with them is something I would never forget. I thank Asif, his camaraderie and companionship, was an essential part in this journey. Our painstakingly long unnecessary, meaningless, thought-provoking intellectual discussions added another dimension to this experience. I thank Nicolas, my first friend in the lab, I would miss the time we spent grazing around. I thank Sebin for being a great friend and labmate. I thank some new friends I made in the last leg of this journey, Antoine and Michelle. Antoine's bizarre one-liners, the late afternoon chess, and his unapologetic political wit is something I will always cherish. The routine coffees with Michelle made the late summer of 2018 more memorable, and her 50's American housewife peculiarities added more spice to this potpourri. I earnestly thank some other friends, Margaux and Ludivine, for sparing their time and helping me explore Grenoble and Paris. Susie, Lucie, Songzi, Gabrielle, Ahuitz, Madeline, Louie, Valentin, and Laure are some other people who unknowingly became part of this journey. I thank some old pals for sticking by my side, Amit, Naman, Bineet, Ranjoy, Ankit, Ayan, Arjun, and Badal.

Above all, I would like to thank the cafes for tolerating my peculiar coffee habits. French

coffee shop (at place claveyson and champoinnet), Pain et Cie and Express bar are some places where a greater part of my days and weekends have been spent, and where this thesis was written. The pubs, Copans des abord, Subway, La nat, Harper, O'champillon and Boit de sardine, where my evenings and late nights went. In all, I thank all the people who made a difference and thank god for this bittersweet journey.

RÉSUMÉ

Le siècle dernier a été le siècle de la révolution technologique, et les combustibles fossiles ont alimentés cette révolution technologique. Les défis auxquels notre société est confrontée, que ce soit le changement climatique, la situation énergétique mondiale ou l'épuisement des réserves de combustibles fossiles, sont les défis les plus graves que l'homme n'ait jamais rencontrés. L'énergie renouvelable est considérée comme la clé des problématiques énergétiques de notre société et de nombreuses technologies innovantes se font concurrence pour alimenter la prochaine révolution énergétique. Les sources d'énergies renouvelables telles que l'énergie solaire, l'énergie éolienne, la biomasse, l'énergie hydroélectrique, l'énergie géothermique, etc, bien que prometteuses, en raison du coût économique élevé et de la disponibilité limitée des gisements, doivent encore prouver leur pertinence à grande échelle. Presque tous sont saisonniers, et sont donc des sources d'énergie discontinues et non uniformes. Elles ont également une limitation en termes de choix des sites de production et, en général, nécessitent de grandes étendues de terre pour les implanter, ce qui conduit à une faible densité de puissance par unité de surface. Néanmoins, les énergies éolienne et solaire ont beaucoup attiré l'attention au cours des dernières décennies. Cependant, pour que le monde passe complètement des énergies fossiles et nucléaires à l'énergie éolienne et solaire, il est nécessaire de développer de nouveaux types de systèmes capables de générer de l'énergie à moindre coût et avec moins de contraintes d'implantation.

Dans cette quête de sources d'énergies pérennes, notre société se tourne vers la communauté scientifique pour trouver des solutions innovantes et cette thèse en est une étape. Les systèmes d'énergie éolienne à haute altitude (HAWE), plus communément appelés systèmes éoliens aéroportés (AWES) sont considérés comme l'une des solutions aux besoins énergétiques des générations futures. L'énergie éolienne aéroportée (AWE) est un concept innovant visant à utiliser l'énergie du vent à haute altitude, car ces systèmes sont plus faciles à installer sur terre et en mer. De plus, le vent à haute altitude est plus fort et plus stable. Enfin, les systèmes AWE proposés nécessitent moins de matériaux de structure et devraient donc être beaucoup moins chers que toute autre source d'énergie disponible. L'énergie du vent à haute altitude est donc une perspective prometteuse dans cette quête pour trouver une solution à nos problèmes énergétiques.

Dans ce travail, la faisabilité des systèmes d'énergie éolienne aéroportés basés sur l'effet Magnus est explorée. Le travail présente un bref historique des systèmes d'énergie éolienne aéroportés et des concepts de base nécessaires pour développer une compréhension de la technologie AWE. Il examine en détail les systèmes aéroportés basés sur l'effet Magnus et donne une perspective historique sur les machines basées sur cet effet. Il examine en détail les propriétés aérodynamiques de l'effet Magnus et présente un modèle aérodynamique pour ces systèmes, la modélisation étant un aspect important de toute technologie. Ce travail présente un modèle détaillé des systèmes AWE basés sur l'effet Magnus ainsi que les algorithmes de contrôle nécessaires au fonctionnement de tels systèmes. Les courbes de puissance sont des outils couramment utilisés pour analyser les systèmes d'énergie éolienne. Ce travail présente une

approche pour la conception de courbes de puissance pour les systèmes AWE afin d'analyser les capacités de production d'énergie des éoliennes aéroportées.

ABSTRACT

Last century has been the century of the technology revolution. Fossil fuels have fueled this technology revolution. The challenges faced by our society, be it the climate change or the world energy situation or the depletion of fossil fuel reserves, are the most grievous challenges faced by any generation. Renewable energy is believed to be the key to energy problems of our society. There are many innovative technologies competing against each other to fuel the next energy revolution. Renewables sources of energies such as solar, wind, biomass, hydropower, geothermal etc. Though promising but due to the high economic cost and limited availability of the sites, they are yet to prove their mass scale applicability. Almost all of them are seasonal, hence, are discontinuous and non-uniform sources of energy. They also have a limitation in terms of choice of plant sites, and generally, require large tracts of land for plants which lead to low power density per unit area. Nonetheless, Wind and Solar energy have attracted a lot of attention in the last few decades. However, for the world to fully shift from fossil fuels and nuclear energy to wind and solar power, it is necessary to develop new kind of systems which can generate continuous power at a lower cost with fewer site selection constraints.

In the quest to find the perennial clean source of energy our society is looking towards the scientific community for innovative solutions. This thesis is one such step towards finding innovative solutions to our energy problems. High altitude wind energy systems (HAWES) or more commonly known as Airborne wind energy systems (AWES) are believed to be one of the solution to the energy needs of the future generations. Airborne wind energy (AWE) is an innovative concept aiming at utilizing the energy of the high altitude wind currents, as they are easier to install both on shore and off-shore, and also the high altitude wind currents are more uniform across the globe. Also, the proposed AWE systems require less structural material. Thus, they are expected to be much cheaper than any other available energy source.

In this work, the feasibility of Magnus-based airborne wind energy systems is explored. The work presents in detail a brief history of Airborne wind energy systems and the basic concepts needed to develop an understanding about the AWE technology. It discusses in detail Magnus-based airborne systems and gives a historical perspective on the Magnus-effect based machines. In this work the aerodynamical properties of the Magnus effect including the aerodynamic model for such systems is discussed in detail. Since modeling is an important aspect of any technology, this work presents a detailed model of the Magnus-based AWE systems along with the control algorithms required for the operation of such systems. A common tool used to analyze wind-based energy systems is power curves. This work presents an approach to design power curves for AWE systems in order to analyze the power producing capabilities of Airborne wind energy systems.

Contents

ACKNOWLEDGEMENT	iii
RÉSUMÉ	v
ABSTRACT	vii
LIST OF FIGURES	xiv
LIST OF TABLES	xv
LIST OF ACRONYMS	xvii
1 Introduction	1
1.1 Motivation	1
1.2 Background	3
1.3 Context of the Thesis Work	4
1.4 Background of Thesis Work	5
1.5 Aims and Scope of Thesis Work	5
1.6 Thesis Overview	5
2 State of the Art	7
2.1 Airborne Wind Energy (AWE)	7
2.2 Basic Concepts	20
2.3 Challenges	28
3 Magnus-Based AWE Systems	31
3.1 Introduction	31
3.2 Magnus Effect	32

3.3	Aerodynamic Characteristics of Magnus Effect	37
3.4	Aerodynamic Model	44
3.5	Gipsa-lab Experimental Setup	49
3.6	Conclusion	56
4	Modelling of Magnus-Based AWE Systems	57
4.1	Introduction	57
4.2	System Model	58
4.3	Moments acting on Magnus-based AWE System	68
4.4	Control Strategy	77
4.5	Simulation Results	82
4.6	Conclusion	88
5	Analysis of Power Curves for AWE Systems	89
5.1	Introduction	89
5.2	Modelling of Power Curves	91
5.3	Ground Station Architecture	97
5.4	Control and Optimization of Output Power	101
5.5	Numerical Application	104
5.6	Conclusion	114
6	General Conclusions	115
6.1	Conclusions	115
6.2	Perspectives	116
	Publications	119
	Appendix A	121
	Bibliography	131

List of Figures

2.1	Charvolant - Kite Buggy by George Pecoock [13].	8
2.2	Laddermill Concept by Webb Ockels [16].	9
2.3	Distribution of Airborne Wind Energy Community around the World [27].	10
2.4	TwingTec Prototype [21].	11
2.5	Altaeros Prototype [31].	12
2.6	Makani 600 KW prototype [17].	13
2.7	Kite Types from the survey presented in [33].	14
2.8	3.5 MW Skysail Wind Farm Concept [28].	14
2.9	55 KW Skysail Demonstrator [28].	15
2.10	20 KW Kitepower demonstrator [29].	16
2.11	Enerkite 30 KW demonstrator [24].	16
2.12	Different UAV based AWE systems (figure borrowed from [33]).	17
2.13	(Google-X) Makani Power 600 KW M600 Prototype[17].	17
2.14	(Google-X) Makani Power 600 KW M600 Prototype[17].	18
2.15	Ampyx AP2 Prototype [23].	19
2.16	Altaeros Prototype [31].	19
2.17	Omnidea Prototype [25].	20
2.18	Kite based AWE System.	22
2.19	Straight line rope model taken from [55].	23
2.20	Multi-mass rope model taken from [55].	23
2.21	Winch model taken from [55].	24
2.22	Ground station driveline taken from [61].	25
2.23	Operating cycles of AWE.	27
2.24	Power cycle for AWE system.	27

3.1	Gustave Magnus's experimental setup [79],[80].	32
3.2	Magnus Effect.	33
3.3	Maximum coefficient of Lift (C_L) for different lift generating devices [81].	34
3.4	MS Buckau (Baden-Baden) [85].	34
3.5	Barbara Ship [86].	34
3.6	Flettner Rotor Aircraft [86].	35
3.7	Flettner F1 282 Kolibri [86].	35
3.8	Alcyone vessel [88].	35
3.9	E-Ship 1 operated by Enercon [90].	36
3.10	Maserk tanker with installed rotor propulsion system by Norsepower [89].	36
3.11	Conceptual Wind Turbine, [91].	37
3.12	Prototype of Magnus based MAV as proposed by Badalamenti, [92].	37
3.13	Lift, Drag and Moment Coefficient, C_L , C_D and C_m for $Re = 5 \times 10^5$ (dash line), $Re = 10^6$ (solid line) and $Re = 5 \times 10^6$, α is the spin ratio [101].	40
3.14	Lift, Drag and Moment Coefficient, C_L , C_D and C_m , [51].	41
3.15	C_D curves preseneted in Borg-Luther report [111].	42
3.16	C_L curves preseneted in Borg-Luther report [111].	42
3.17	Flow past cylinder without Thom disc (a) and with Thom disc (b).	44
3.18	The lift coefficient C_L as a function of X . Data is taken from Milutinovic ([50]), Reid ([108]), Borg-luther ([111]), Bergeson ([109]), Betz ([113]), Badalamenti ([92]) for different Reynolds number as detailed in table 3.2.	46
3.19	The drag coefficient C_D as a function of X . Data is taken from Milutinovic ([50]), Reid ([108]), Borg-luther ([111]), Bergeson ([109]), Betz ([113]), Badalamenti ([92]) for different Reynolds number as detailed in table 3.2.	47
3.20	The Matlab/Simulink real-time setup used in the experiments.	50
3.21	The Ground station to which the Magnus cylinder was tethered.	51
3.22	The Magnus cylinder used as ABM in the wind tunnel experiments.	51
3.23	Flight trajectory of the small-scale Magnus cylinder on the vertical plane	52

3.24	Wind speed measurement from the wind tunnel and estimates obtained from the filter.	53
3.25	Estimated spin ratio of the Magnus cylinder	53
3.26	Estimated lift coefficient of the system	53
3.27	Estimated drag coefficient of the system	54
3.28	Comparison of the lift and equivalent drag coefficients estimated during the pumping cycles and identification experiments for $v_w = 7m/s$ and $Re = [12.5]$ with the values predicted by the polynomial model proposed in [50].	55
4.1	Forces acting on the Magnus Cylinder.	59
4.2	Magnus-based AWE systems.	62
4.3	Apparent Wind velocity in different phases	66
4.4	The forces acting on the Magnus cylinder.	67
4.5	Various moments acting on the Magnus-based AWE system.	69
4.6	The lift coefficient C_{Lrud} as a function of angle of attack	71
4.7	The lift coefficient C_{Drud} as a function of angle of attack.	72
4.8	Yaw moment due to rudder	74
4.9	An overview of the control strategy. The Magnus rotor moves from minimum radial position r_{min} to a maximum radial position r_{max}	79
4.10	Figure eight guidance law.	80
4.11	Circular orbit guidance law.	81
4.12	Trajectories of the Magnus rotor in $(x_i - z_i)$ and $(y_i - z_i)$ planes for 3 cycles.	85
4.13	Reference and state variable for tether length (r_t, r_{tref}) , tether tension F_r proportional to winch torque T_c , angular speed of the Magnus rotor $(\omega_{cyl}, \omega_{cylref})$, and yaw angle (γ, γ_{ref}) , as function of time for the 3 cycles.	85
4.14	Eight figure corsswind trajectory of ABM in $(x_i - z_i)$ plane.	86
4.15	Swept area comparision of Magnus-based AWE and conventional wind turbine in $(y_i - z_i)$ plane.	87

4.16	The output power simulated P_g during production and recovery phases for the 3 cycles with a comparison with the simplified model under the static assumption. The mean output power is 1469 kW for dynamic simulation and 1674 kW for the simplified model.	87
5.1	Weibull Distribution.	92
5.2	Power curve of a conventional wind turbine.	93
5.3	Magnus-based AWE system.	94
5.4	Power cycles defined by complete production and recovery phases.	97
5.5	Ground station using two separate electrical actuators and a storage device . .	99
5.6	Ground Station using hydraulic stage	99
5.7	Detail of high level algorithm for controlling on-ground AWE system, regarding \dot{r}_{prod} and \dot{r}_{rec} variables. Experienced wind speed can than be modified by controlling altitude z , elevation angle θ_T , and/or azimuthal angle ϕ_T	105
5.8	Power curves: Power production comparison between HAWT Vestas V150 and case 1 and case 2 of MW-size MGAWES. P_{cycle} is decomposed into production and recovery contributions for case 1. Dotted line denotes P_{cycle} when control of elevation angle is not used	109
5.9	High level control variables of case 1, 90m span MGAWES. Top: reel-out speed during production phase (black) and reel-in speed during recovery phase (red) in function of wind speed. Dotted line represents variables when control of elevation angle is not used. Down: Traction force during production (black) and recovery (red) phases.	110
5.10	Power curves: Power production comparison between 12kW HAWT (magenta) and 6m span MGAWES (blue). The dotted line denotes P_{cycle} when the kite stays at altitude 10m and control of elevation angle is not used	112
5.11	High-level control variables for 6m span MGAWES. Top: reel-out speed during production phase (black) and reel-in speed during the recovery phase (red) in function of wind speed. Down: Traction force during production (black) and recovery (red) phases. The dotted line represents variables when the kite stays at altitude 10m and control of elevation angle is not used	113

List of Tables

3.1	List of Past researches considered in Borg-Luther report [111]. Here $\frac{d_c}{d^*}$ refers to the ratio of the diameter of Thom disc to the Magnus cylinder, and sheet no. refers to the curves presented on pages of the report.	43
3.2	Different references used in the study of C_L and C_D . Aspect ratio (AR) and Reynolds number (Re) are given.	45
3.3	Parameters of the Experiments	52
4.1	Simulation parameters for a 500 m^2 Magnus-based AWE system.	84
5.1	Parameters of HAWT VESTAS V150 – 4.2MW TM	106
5.2	Parameters of the 90m span MGAWES.	107
5.3	Considered actuators configurations and corresponding theoretical annual production and capacity factor	108
5.4	Parameters of 12kW HAWT.	109
5.5	Parameters of the 6m span MGAWES.	111
5.6	Considered actuators configurations and corresponding theoretical annual production and capacity factor for considered kW-sized systems	112

List of Acronyms

AWE	Airborne Wind Energy
AWES	Airborne Wind Energy Systems
HAWE	High Altitude Wind Energy
MGAWES	Magnus-based Airborne Wind Energy Systems
UNFCCC	United Nations Framework Convention on Climate Change
EU	European Union
EFSI	European Fund for Strategic Investments
SYSCO	SYStèmes non-linéaires et COmplexit
UAV	Unmanned Aerial Vehicles
H2020	Horizon 2020
LCOE	Levelized Cost of Energy
CWT	Conventional wind turbines
EKF	Extended Kalman Filter
ABM	Airborne Magnus cylinder
IEA	International energy agency
HAWT	Horizontal axis wind turbine

Introduction

1.1 Motivation

Energy is the engine of society. About 1.9 million years ago prehistoric man learned to control the fire. Fire fueled the human evolution and cultural growth. It was the first energy source controlled by us. Thus, can be regarded as the first engine driving the story of our evolution.

Today and since the last century, fossil fuels have been the engine of our evolution. However, this engine is running out of fuel. With the depletion of fossil fuel reserves and the threat of global warming, there is a push to find clean sources of energy. This search for the next ubiquitous energy source that would fuel the next epoch of human evolution has become the goal of our society. In this endeavor, there are two promising technologies nuclear energy and renewable energy. However, due to the high-risk factor and limited applicability of nuclear energy, today the world is looking with a promising eye towards the renewable sources of energy.

Of all the renewable sources of energy, solar and wind have emerged as the most promising alternative. To facilitate the development of clean sources of energy and thwart the threat of climate change, in the recent past there have been many agreements signed both on the international and national level. In particular:

- **United Nations Framework Convention on Climate Change:** UNFCCC is an international treaty on climate change signed on 9 May 1992 in Rio de Janeiro [1]. The main objective of the treaty is to stabilize the greenhouse gases in the atmosphere. And as a part of the action plan, a direct emphasis was given to the development of clean sources of energy.
- **Koyoto Protocol:** As an extension of the UNFCCC, Kyoto protocol was adopted on 11 December 1997 in Kyoto, Japan [2]. The protocol aimed at working on the common goal of fighting climate change. And as an implementing measure, it further boosted the research on renewable sources of energy. The first commitment period was from 2008-2012. The second commitment period started from 2012 by the signing of Doha agreement in 2012 negotiations on which culminated in the signing of the Paris agreement.
- **Paris Agreement:** Signed on 12 December 2015 with 195 signatories and with 180 countries party to it [3]. The agreement aims at the long-term goal of keeping the global

increase in temperature below 2 degrees. Under this agreement, each country is required to determine and design an action plan to mitigate the effects of global warming.

- **Other Accords and agreements:** In addition to these, there have been several other accords signed on the international level. Of which some noteworthy accords are Bali Action Plan (2007) [4], the Copenhagen Accord (2009) [5], the Cancún agreements (2010) [6], and the Durban Platform for Enhanced Action (2012) [7].

One of the salient features of all the environmental agreements and accords is the commitment towards the development and commercial deployment of clean sources of energy. Thanks to these international accords there is a constant push towards financing clean energy research and projects both on the international and national level. In Europe, some of the main funding schemes are part of the European Union's (EU) action plan to reduce the greenhouse gas emission. Some noteworthy funding schemes in Europe are:

- Horizon 2020
- NER 300
- ETS Innovation Fund
- InnovFin
- European Fund for Strategic Investments (EFSI), etc.

In this context, there has been rapid growth in the renewable energy infrastructure and technologies. Despite this as of 2017 [8], renewable energy contribution to global energy consumption was 19.3%. A major part of which is contributed by hydroelectric power. And of 19.3% only 2.2% accounts for electricity consumption coming from emerging renewables which includes solar, geothermal, wind, biomass, and other clean energy sources. According to International energy agency's (IEA) energy status report 2017 [9], renewables contributed total 25% to global electricity generation with the rest coming from fossil fuels and nuclear energy. Of this 25%, Hydro-power was the largest contributor with a share of 65% of overall renewable output. Of all the emerging renewables, wind energy is regarded as one of the most promising sources of clean energy. As of 2017, the total installed capacity of wind power was around 539 GW [8], with record growth in Europe and India, and 5.6% estimated contribution to the world power production in the year 2017.

Wind energy with its huge untapped potential, and still a small market size, backed by a favourable political environment; a global effort is being made to improve the wind turbines in order to increase their market penetration. This calls for an increase in the power capacity of the wind turbines. However, the conventional wind turbines pose a structural and design limitation. Furthermore, globally, wind flow is not uniform at lower altitudes and varies seasonally, which limits the number of potential sites across the globe. Thus, to overcome these major limitations, the research community is looking at other innovative ways to harness the wind energy. One such promising concept is High altitude wind energy systems (HAWE).

1.2 Background

High altitude wind energy systems or more commonly known as Airborne Wind Energy (AWE) targets to harvest the winds at an altitude range of 200 m - 10000 m. Airborne Wind Energy systems aim at overcoming the main limitations of conventional wind turbines, namely:

- Limited swept area and size,
- Intermittent availability of wind flow,
- Limitation of number of potential sites,
- Regulatory and implementation constraints.

Airborne Wind Energy by using wind currents flowing at higher altitudes (as they are more uniform and constant) can lead to more stable power production all around the year at lower cost and can be more easily installed theoretically almost anywhere. In addition to this, the innovative design proposes a higher swept area with lesser structural material, and thus, greater energy production at a lower cost.

A typical AWE system consists of an airborne platform flying at high altitude and using wind currents to drive the on-board turbine or ground-based turbine by means of tether connected to the platform. The concept was first proposed by Miles Loyd in 1980 [10]. In his work, he analyzed the dynamics of such a system and also the maximum yield of such systems. But with the advent of other novel technologies in renewable energy, the idea of AWE systems was forgotten. The concept once again attracted the interest of researchers in mid-nineties. Currently, there are many research groups and companies developing their prototype around the world, and working on different aspects of AWE technology. Projects on AWE systems have also attracted a steady source of funding from various government bodies as well as private sector. According to [11], there were 20 patents on AWE systems till 2003 which rose to 172 by 2013, and thus, indicating the interest and advancement in research on AWE.

In the last 10 years, many issues regarding the AWE systems have been solved. At present, the research community is focused on achieving a fully automated 24x7 operational system. The main focus of the research is on the design and control of AWE systems. Simultaneously, other aspects of AWE systems are also being researched upon such as aerodynamics of airborne platform, landing & take-off strategy, economic viability, structural design of AWE components, optimization of power, use of other innovative designs, etc.

This thesis work is our effort to supplement and contribute to the on-going research on the development of Airborne wind energy systems (AWES), particularly, the systems based on the innovative design concept of Magnus effect.

1.3 Context of the Thesis Work

The thesis work has been carried out at GIPSA-lab, Grenoble, France, from 16th November 2015 to 15th November 2018. The research work was accomplished under the supervision of Dr. Ahmad Hably, associate professor at Grenoble-INP, and co-supervision of Jonathan Dumon, CNRS engineer. The research work was financed by Grenoble-INP.

The thesis work has been part of the EOFLY, a multi-disciplinary research group of GIPSA-lab, with former Ph.D. students:

1. Rogelio Lozano, Grenoble-INP, Ph.D. on the design, control, and validation of AWE systems. Currently founder of the start-up "*Bladetips Energy*", working on an innovative off-shore rotary AWE system.
2. Mariam Ahmed, Grenoble-INP, Ph.D. on grid connection of AWE systems, in collaboration with G2Elab.

Gipsa-lab is a research unit of CNRS, Grenoble-INP (Grenoble Institute of Technology), and University Grenoble-Alpes, and is in agreement with INRIA. It is headed by Jerome Mars. As of 2018, the lab consists of 350 people, which includes about 150 doctoral students. The lab conducts multi-disciplinary research on complex signals and systems. It is recognized internationally for its research contributions on Automatic Control, Signal and Images processing, Speech and Cognition. The research unit of the lab is responsible for both developing and undertaking projects in the fields of energy, environment, communication, intelligent systems, robotics, life sciences, and language engineering. Gipsa-lab maintains an active link with the companies and also engages in the incubation activities for burgeoning technology start-ups. Bladetips energy, Ebike labs, Drone interactive, Amiral technologies, etc. are few spin-offs from the lab. Apart from this, the researchers at Gipsa-lab also engage in teaching activities and are associated with various universities across Europe.

The lab consists of 12 research teams grouped under three departments, namely:

- Automatic control,
- Images-signal,
- Speech-cognition.

The thesis research work was part of the SYSCO team (SYStèmes non-linéaires et COMplexité) under the department of automatic control. The team is headed by Gildas Besançon and Mirko Fiacchini. The main research interest of the team lies in the field of control of nonlinear and complex systems, from both theoretical and application points of view.

The experiments involved in this thesis work were performed at the in-house wind tunnel at Gipsa-lab. All the prototypes were fabricated at Gipsa-lab using the in-house 3-D printers available at Gipsa-lab.

1.4 Background of Thesis Work

Previously, there have been two doctoral studies conducted on AWE systems at Gipsa-lab under the joint supervision of Dr. Ahmad Hably and other researchers from Gipsa-lab.

In April 2014, Rogelio Lozano Jr. defended his doctoral research work on the flight dynamics of a kite-based AWE system under the supervision of Dr. Mazen Alamir and co-supervision of Dr. Ahmad Hably. He contributed towards the development of the in-house wind tunnel at the Gipsa-lab and tested several prototypes of kite-based AWE systems. His work culminated into a start-up Bladetips energy.

In February 2014, Mariam Ahmad defended her doctoral research work on the grid connection of AWE systems under the supervision of Dr. Seddik Bacha and co-supervision of Dr. Ahmad Hably. The work was conducted in collaboration with the G2E-lab and aimed at the grid integration for AWE systems.

1.5 Aims and Scope of Thesis Work

Taking the previous work done on AWE systems forward. A study of the AWE systems using the innovative concept of Magnus effect was envisaged by Dr. Ahmad Hably with Jonathan Dumon as co-supervisor. The main objectives of the thesis work were:

- Study and validation of the aerodynamic model of the Magnus Effect.
- Development of a 3-D Mathematical model for Magnus-based AWE systems.
- Design of guidance control for Magnus-based AWE systems.
- Study of operational strategies for maximum power production by an AWE system.
- Development of the power curves for AWE systems.

1.6 Thesis Overview

This thesis manuscript is structured into six chapters. The second chapter, '*State of the art*', introduces the concept of Airborne wind energy systems. It presents in detail the historical perspective of AWE. It further discusses the advancement in AWE and presents the different types of AWE systems. A short overview of different research teams and start-ups working on AWE systems around the world is also presented. The chapter then discusses the basic concepts of AWE systems with an emphasis on ground-based AWE systems. It presents the classical mathematical models used in literature to model various AWE components such as the tether, airborne platform and ground station. The chapter also states the basic functional phases and power generation by AWE systems. Moreover, the chapter also presents some major challenges faced by AWE technology.

The third chapter, '*Magnus-based AWE systems*', introduces the innovative concept of the Magnus effect. It discusses in detail the aerodynamic model of the Magnus effect. It presents some of the past application of the Magnus effect. It then discusses the two-step approach adopted to validate the aerodynamic model of Magnus effect and presents our results on it.

The fourth chapter, '*Modelling of Magnus-based systems*', discusses in detail the mathematical model of Magnus-based AWE systems. It describes the modelling approach adopted from flight dynamics and gives detailed expressions for all the forces and moments acting on such type of systems and their effects. It then presents the control & guidance algorithm adopted in this work to perform crosswind maneuvers and discusses the simulation results obtained.

The fifth chapter, '*Analysis of Power Curves for AWE Systems*', presents a theoretical approach to develop power curves for AWE systems. It presents some operational strategies required for the maximization of the power generation. Furthermore, it presents an optimization technique to optimize the variables for maximum power generation. It also discusses two ground station configurations which are considered for developing the power curves for a MW and KW sized Magnus-based airborne wind energy system. The chapter also draws some comparisons with the conventional wind turbine in order to highlight the advantages of AWES over conventional wind turbines.

The thesis ends with some conclusions and perspectives presented in sixth chapter, '*General Conclusions*'.

State of the Art

Contents

2.1 Airborne Wind Energy (AWE)	7
2.1.1 Historical Perspective of Airborne Wind Energy	7
2.1.2 Classification of Airborne Wind Energy (AWE) Systems	9
2.2 Basic Concepts	20
2.2.1 Configuration of AWE Systems	21
2.2.2 Power Generation	24
2.2.3 AWE Operational Cycles	26
2.3 Challenges	28

2.1 Airborne Wind Energy (AWE)

Since the dawn of civilization, the human mind has always been captivated by the idea of flight. At the beginning of 20th century, the Wright brother's first flight was the declaration of the beginning of space age, where sky was no more a limit. With the advances in technology, the gap between imagination and reality has shrunk. Thus, fueling the human will to find more formidable and innovative solutions to our existing problems. Airborne wind energy (AWE), or High altitude wind energy (HAWE), is one such human endeavor to subjugate the power of high altitude winds. The concept consists of an airborne platform attached to the ground by a tether and depending on the type of system the generator can be located on the ground or on-board.

2.1.1 Historical Perspective of Airborne Wind Energy

Since antiquity, kite flying has been a hobby in several cultures and they are believed to be invented in China around 5th century BC. For several thousand years, they were the only known man-made airborne object. Over the centuries, kites have been used in many applications such as measuring distance, pulling loads, weather forecasting etc. The famous experiment by Benjamin Franklin in 1752 [12], used kites to understand lightning and electricity. In 1826, the English inventor and a pioneer in kite traction, George Pocock, invented a carriage

named Charvolant driven by kite as shown in figure 2.1. His work on the lifting capabilities and traction power of kites published in 1827 is considered one of the first major scientific attempts to harness the kite power [13]. The second half of the 19th century saw major advances in the airborne platforms such as zeppelins, hot air balloons, etc. However, with the invention of airplanes, the interest in airborne platforms such as kites, balloons, zeppelin, etc. diminished.

The second half of the 20th century saw the re-emergence of research on airborne platforms and their usage. In 1976, Peter Payne and Charles McCutchen, patented their invention of

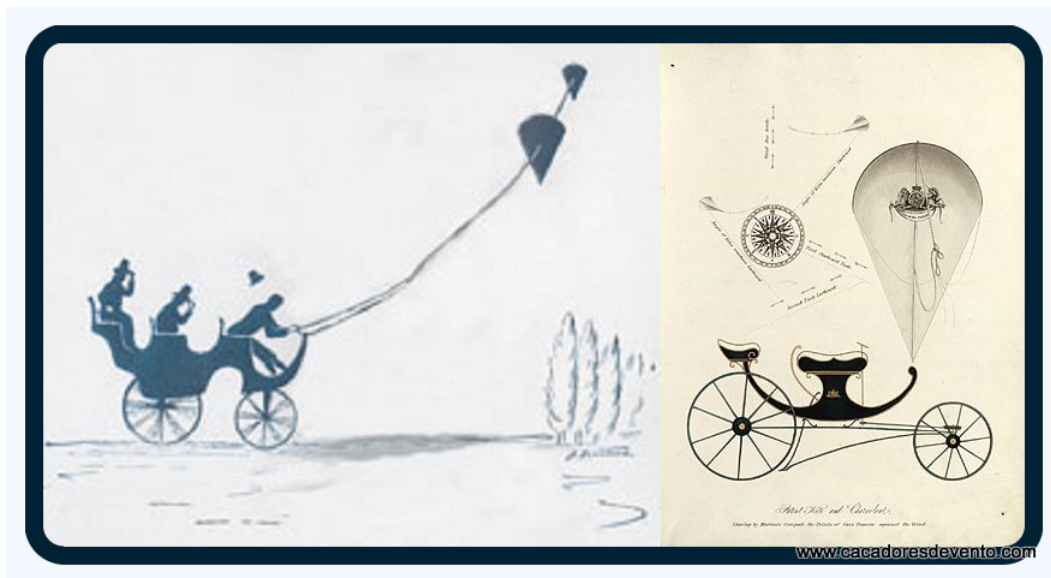


Figure 2.1: Charvolant - Kite Buggy by George Pecoock [13].

‘self-erecting windmill’ [14]. In 1979, an Australian engineer, Bryant Roberts, conducted first experiments to harness high altitude wind energy [15]. In 1980, Miles L. Loyd published a paper [10] on the concept of using kites or an Unmanned Aerial Vehicles (UAV) to produce electricity by using the forces developed in the kite tether to drive a generator located on the ground. This work by Loyd is regarded by AWE researchers as the beginning of research on Airborne Wind Energy. In his work, he defined the maximum theoretical power that can be extracted from such systems by following crosswind trajectory (explained in detail in section 2.2.2) which is now considered as a benchmark in AWE community.

However, for the following two decades there was very little research done to explore the applicability of the concept. In late 1990’s with a global push towards the green energy, the concept once again attracted the attention of research community. In 1997, the Dutch astronaut and TU Delft professor, Wubbo Ockels, proposed the concept of ‘Laddermill’ [16], as shown in figure 2.2, a multi-kite system driving a generator located on ground through a tether. In the following decade, a number of innovative startups and research teams were established across Europe and USA to explore the commercial usefulness of the concept. In 2001, the German startup Skysails started working on the commercial kite systems to provide cheap energy to cargo ships. In 2006, Makani power, a startup founded by Corwin Hardham,

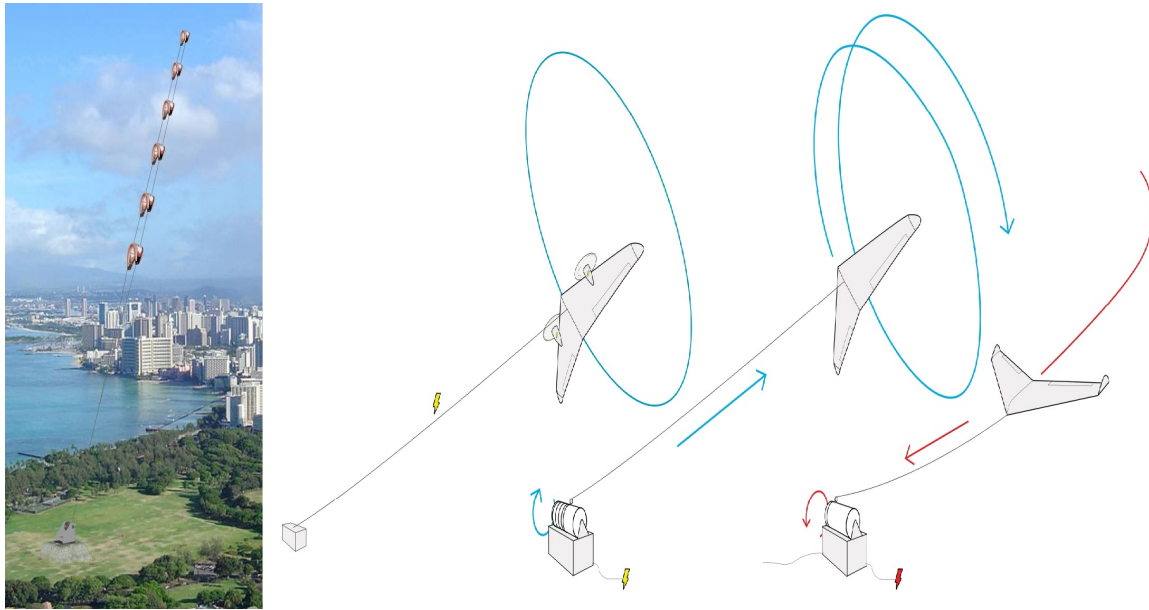


Figure 2.2: Laddermill Concept by Webb Ockels [16].

started exploring the concept using UAV as an airborne platform [17]. Simultaneously, other companies such as WindLift in US [18], NTS in Germany [19], Kitegen in Italy [20], Twingtec in Switzerland [21], and other research teams around the world, started working on the concept. To organize the efforts on airborne wind energy, the first conference on the concept of AWE was held in California in 2005. In 2008, with the combined efforts of a startup Joby energy and researchers across the globe, a society on High altitude wind energy known as Airborne Wind Energy Consortium (AWESCO) was officially established in 2009 [22]. Its first official conference was held at Stanford University, USA, in 2010. The latest conference being organized at University of Freiburg, Germany in October 2017. Currently, there are many startups and research teams all around the world working on the subject, as shown in figure 2.3, with companies such as X Development LLC. (formerly Google-X) [17], Ampyx power [23], Enerkite [24], Omnidea Lda.[25], etc. experimenting with their operational prototypes ranging from few kW to 600 kW. AWE has also attracted the attention of many leading energy companies such as E.On, Engie, GE, etc. Several AWE projects are part of EU's eighth framework programme, commonly referred to as H2020 initiative, under which many projects related to research, technological development, and innovation are being funded [26], such as Ampyx Power, and 14 doctoral thesis under the AWESCO initiative, etc.

2.1.2 Classification of Airborne Wind Energy (AWE) Systems

With growing interest in the AWE, a number of innovative concepts are being proposed and are developed to generate electricity in the most optimal way. Classically, AWE systems are classified based on the location of turbine .i.e. into two main categories: Ground-based systems and On-board power generation systems. In this work, a new basis of classification is

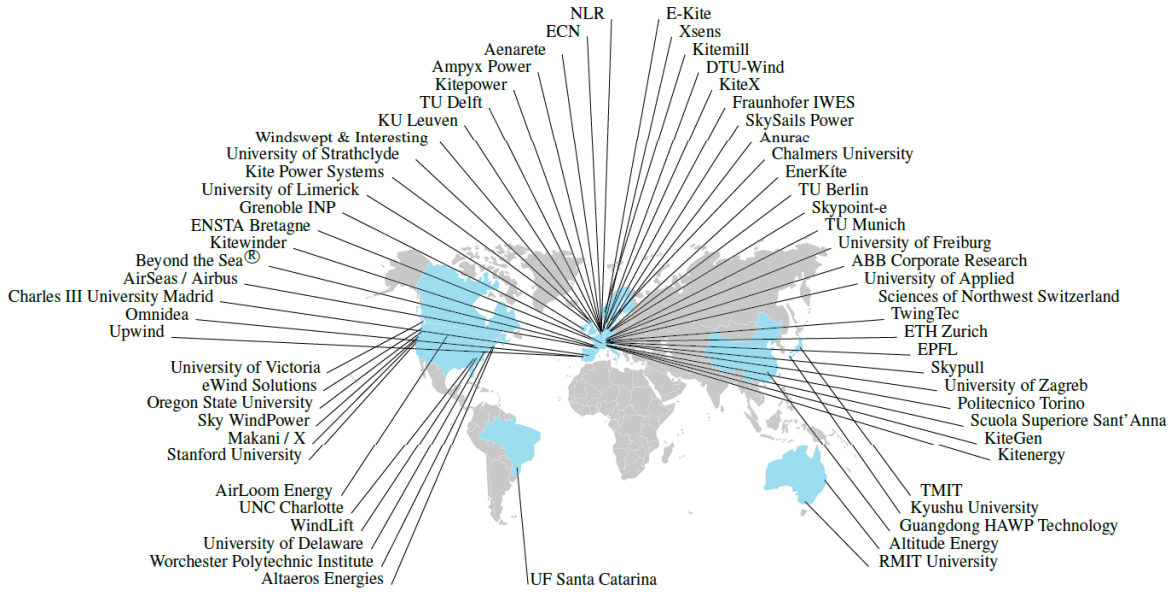


Figure 2.3: Distribution of Airborne Wind Energy Community around the World [27].

introduced i.e. based on the type of airborne platform. Thus, in this work AWE systems are classified into three categories, namely:

1. Ground-based AWE systems,
2. On-board power generation systems,
3. Type of Airborne platform.

In ground-based systems, electricity is produced by the turbine located on the ground. They use the traction force developed in the tether attached to the airborne platform to drive the generator located on ground as shown in figure 2.4.

On the other hand in on-board power generation systems, the electricity is produced by the turbine mounted on the airborne platform as shown in figure 2.5. The power is then transferred through conducting cables inside the tether to a ground station.

Another way of classifying the AWE systems is on the basis of choice of airborne platform. Historically, the AWE design concepts have focused on the application of soft wings as an airborne platform [28],[20],[24],[19],[29]. With the advancement in technology and growing interest in the field, many innovative designs applying different airborne strategies are being developed such as usage of Unmanned aerial vehicle's (UAV) by [23],[21],[17], Magnus-effect based aerostats by [25],[30], lighter than air aerostat by [31], multiple wing systems as used by [32], etc.

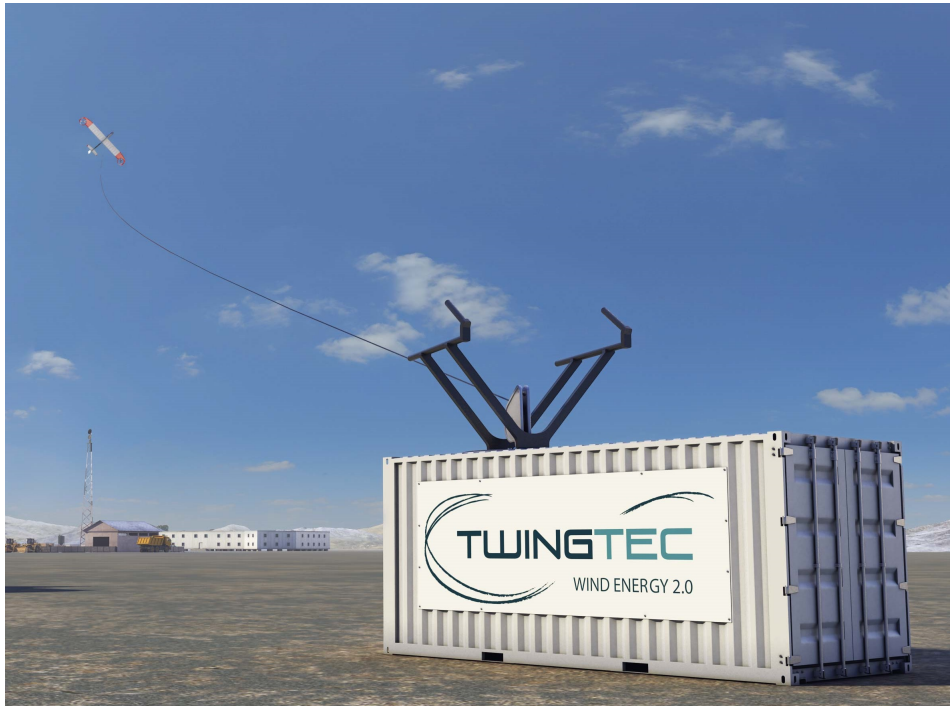


Figure 2.4: TwingTec Prototype [21].

2.1.2.1 Ground-based AWE Systems

The ground-based AWE systems generate electricity by driving the turbine located at the ground. They utilize the tether traction to drive the electric generator. Thus, tether traction plays a vital role in such systems which in turn is related to the lift generating capability of the airborne platform.

In all such systems, electricity generation is characterized by two operation cycles, namely, generation phase and retraction phase. In the generation phase, the airborne platform follows a predefined trajectory in the sky. Thus, gaining altitude and unwinding the tether from the drum located on the ground. On the other hand, the retraction phase comprises of rewinding of the tether on to the drum, which leads to consumption of a portion of the electricity produced. As the power produced is related to the lift generated by the airborne platform, the choice of airborne platform and the trajectory followed are key elements in the design of such platforms.

In order to maximize the traction force developed in the tether cable, the two most common adopted trajectories are circular orbits and eight-figure loop. As the airborne platform moves on the predefined path, it encounters strong relative winds which generate high lift which in turn produces high traction force in the tether. Hence, the choice of the airborne platform and the trajectory is an area of constant innovation.

2.1.2.2 On-board Power Generation

In the on-board generation, the turbine is mounted on the airborne platform. As it moves in the air, it uses the power of high altitude winds to drive the turbine. Such systems usually make use of the lighter than air airborne platforms and are usually heavier in comparison to the ground-based generation systems. They also experience higher drag forces. One particular advantage of such systems over the ground-based generation is that they can take off and land using classical methods such as vertical take-off and landing (VTOL), planar vertical take-off and landing (PVTOL), etc. Also, as the turbines are mounted directly on the airborne platform, the on-board systems can harness the power of relative winds better than their counterparts. They also require a tether capable to transmit high current and voltage to the ground station which leads to a tether of larger diameter. Thus, increasing the tether drag. Makani Power is testing its 600 KW prototype on-board generation system as shown in figure 2.6 [17].



Figure 2.5: Altaeros Prototype [31].

2.1.2.3 Classification based on the type of Airborne Platform

Apart from the location of the turbine, the other possible way to classify the AWE systems is based on the choice of airborne platform. The choice of an airborne platform determines the lift force generated which in turn determines the traction force developed in the rope, especially in the case of ground-based systems. Hence, over the past decade, a variety of concepts using different types of airborne platforms have been proposed. They can be divided broadly into four main categories:

1. Kite based airborne platform,



Figure 2.6: Makani 600 KW prototype [17].

2. Unmanned Aerial Vehicles (UAV),
3. Lighter than air systems,
4. Other Innovative concepts.

1. Kite based airborne platform:

Kite-based airborne platforms are used in ground-based generation. They can further be divided into Soft kites and Rigid kites. Figure 2.7 (from the survey presented in [33]) presents the various kite designs being used by the AWE research teams and startups.

- **Soft Kite:**

Soft kites make use of the leading edge inflatable kite. First proposed by Wubbo Ockels in the year 1997 [16], they are one of the most widely researched design concept with the teams from TU Delft, University of Freiburg leading research in development of such systems.

Soft kites are lighter in mass. They have good lift over drag ratio ($\frac{C_L}{C_D}$), which measures the lifting capability of any airborne surface. Thus, making them a suitable choice for ground-based AWE systems. They consist of a multi-line tether with a control unit located at the bridle point. The control is performed by changing the direction of leading edge of the kite. This is done by changing the angle between the two tether lines attached to the two extremes of the kite. Reference [34], gives a detailed control oriented input model for soft kites. They are usually made to perform an eight-figure orbit in crosswind to generate maximum lift and traction force in the tether. Wubbo Ockel's Laddermill uses multiple kites as an airborne

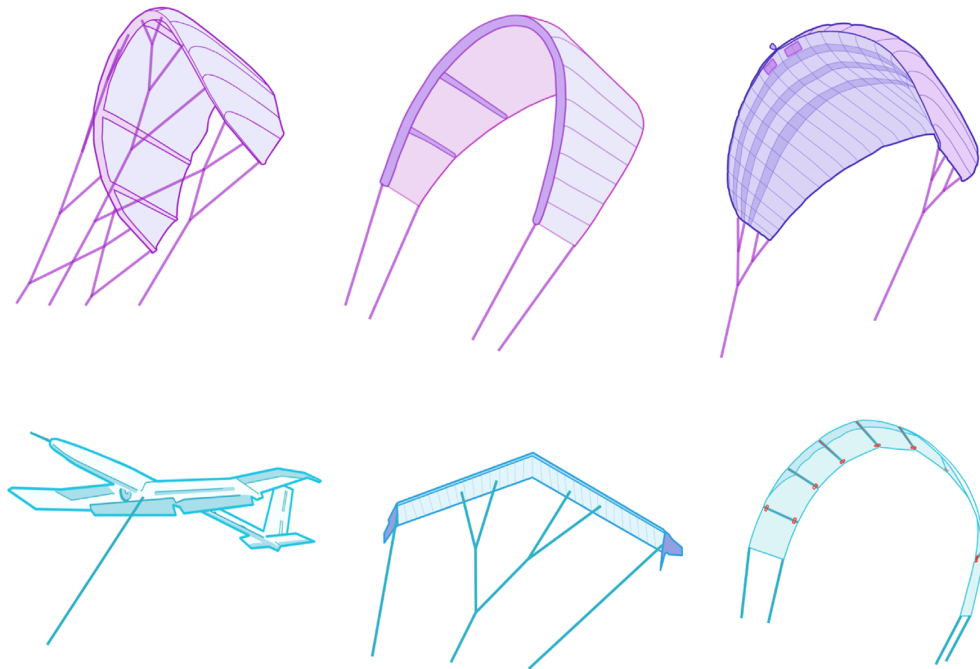


Figure 2.7: Kite Types from the survey presented in [33].

platform to maximize the energy produced [16]. However, one of the most challenging and practical problems is making sure the multi-line tether does not entangle. Though their lighter mass and simple configuration make them advantageous from the commercial point of view as the cost of maintenance and replacement are much smaller in comparison to other such platforms. However, this also makes them less durable and more susceptible to wear and tear. Also, the design constraints limit their size and scalability to large systems as beyond a certain aspect ratio mass increases cubically with respect to the wingspan.



Figure 2.8: 3.5 MW Skysail Wind Farm Concept [28].



Figure 2.9: 55 KW Skysail Demonstrator [28].

Skysails is currently the market leader in developing automated towing technology using soft kites [28]. They have been selling and developing soft kite-based products for marine application. SkySails Power, a subsidiary of SkySails, is developing AWE systems. They have a functional 55 KW AWE soft kite-based power system as shown in figure 2.9. They are currently developing a 1 MW prototype. The company aims to scale-up the technology to 3.5 MW AWE based wind farm as shown in figure 2.8.

Kite Power is the research group of TU Delft on AWES headed by Dr. Roland Schmehl [29]. In 2012, they developed a 20 KW demonstrator using soft kites of up to $50 m^2$ surface area as shown in figure 2.10. Its commercial spin-off Kitepower B.V is developing a 100 kW prototype with an aim to commercialize the system by the end of 2018 [35].

University of Freiburg with its Highwind and Awesco Project, is one of the leading research groups in the development of AWE systems under the leadership of Dr. Moritz Diehl [36]. They are currently researching on the aeroelastic behaviour of soft kites as a part of AWECO doctoral research group.

KiteGen is an Italian startup founded in 2007 [20]. In 2006, the team built their first 5 kW prototype. They are currently developing a 3 MW prototype in 'stem configuration', where the airborne platform is pulled by tether through pulleys.

- **Rigid Kite:**

Rigid kite systems utilises a semi-rigid wing and work similarly like the soft kites using multi-line tether to control it. One of the advantage of such systems over the



Figure 2.10: 20 KW Kitepower demonstrator [29].

soft kite is their better aerodynamic performance. Being made of rigid structure they are more durable and are more resistant to wear and tear. Also, they are expected to perform better in crosswind maneuver as they can withstand higher forces. However, the cost of replacement and maintenance are higher as compared to the soft kite.

Enerkite is one of the leading startups working on the rigid kites [24]. Founded in 2010, they demonstrated their 30 kW prototype EK30 mounted on a mobile platform at Berlin in 2013 as shown in figure 2.11. They are currently developing a 100 kW prototype with an aim to launch it by 2019 [37].



Figure 2.11: Enerkite 30 KW demonstrator [24].

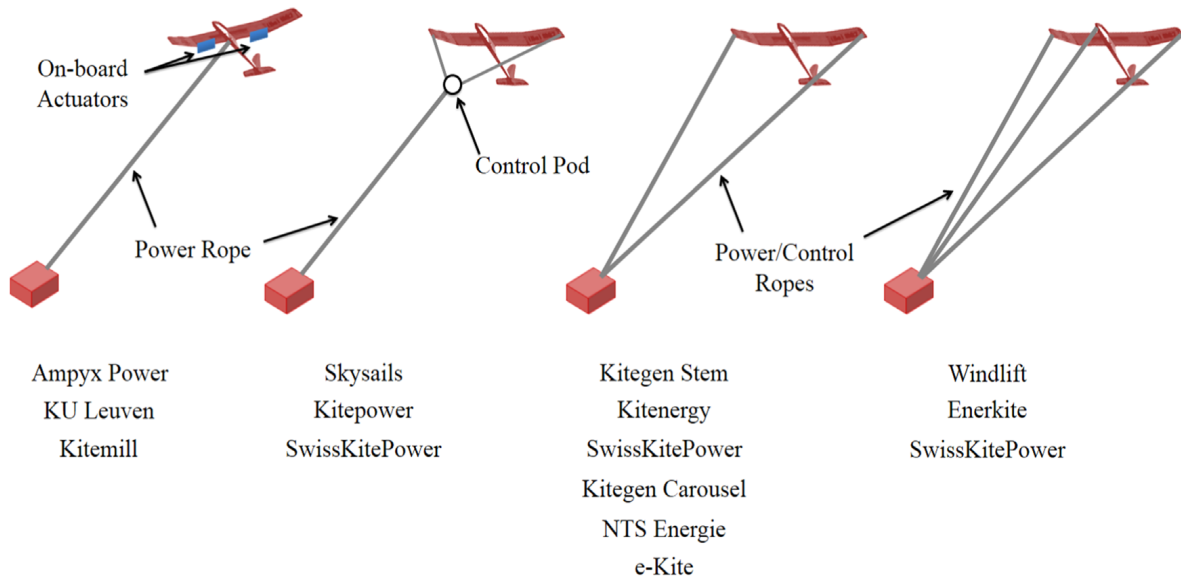


Figure 2.12: Different UAV based AWE systems (figure borrowed from [33]).

2. Unmanned Aerial Vehicles (UAV):

The use of UAV or a glider as an airborne platform was first imagined by Miles Lyod in his paper in 1980, [10]. In UAV based AWE systems, a UAV is connected by a tether to the ground station. They are used as an airborne platform for both ground-based, and on-board generation, [23], [17]. In the latter type of systems, a turbine is mounted on the wings or on the fuselage of the UAV. The advantage of good aerodynamic performance (i.e. high lift-to-drag ratio $\frac{C_L}{C_D}$ as detailed in section 2.2.2) and the availability of classical flight controls to control the trajectory makes UAV based systems a promising concept.

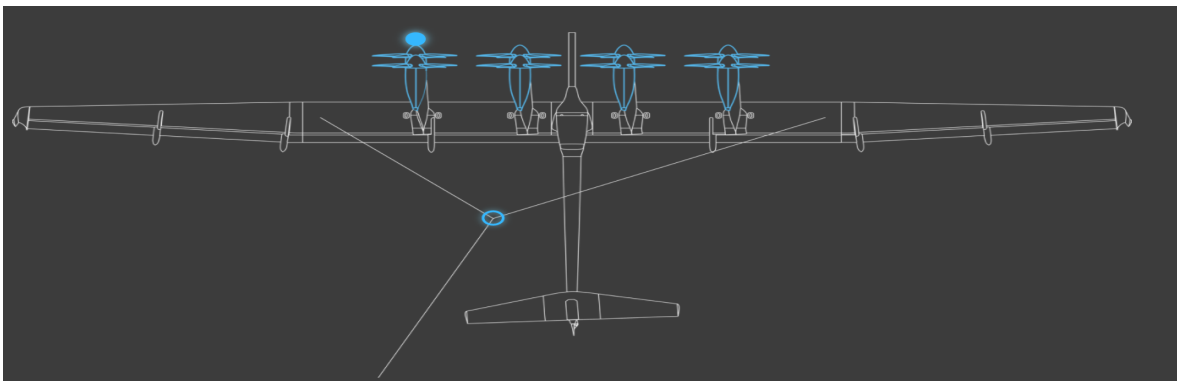


Figure 2.13: (Google-X) Makani Power 600 KW M600 Prototype[17].



Figure 2.14: (Google-X) Makani Power 600 KW M600 Prototype[17].

Makani Power founded in 2006 and acquired by X Development LLC. (formerly Google-X) in 2013, has been working on UAV based on-board power generation AWE system [17]. They developed a 10 kW prototype in 2010 and latest being a large-scale 600 KW M600 prototype released in 2016. M600 as shown in figure 2.13 and 2.14, has a wingspan of 26 m and consists of 8 rotors each driving a magnetic on-board generator while performing a circular trajectory in crosswind. It consists of a 500 m long tether and in take-off phase consumes a part of electricity to climb to the defined altitude. Makani is aiming to develop a 1 MW prototype by 2020.

Ampyx Power is a Dutch startup founded in 2008 [23]. They have developed functioning prototypes of UAV based ground generation systems performing eight-figure crosswind manoeuvres as shown in figure 2.15. They are currently developing a 2 MW AP3 prototype with an autonomous landing and take-off capability from a rotating platform. They aim to develop off-shore UAV based wind farms and are in an agreement with E.ON to test their planned AP3 and AP4 prototypes on E.ON testing sites.

3. Lighter than air:

There are several concepts using lighter than air airborne platform for both type of systems, on-board and ground-based generation. Lighter than air airborne platform consists of an inflatable aerostat filled with a lighter than air gas like Helium. Such systems due to their simple robust design have an advantage in terms of scalability. Also, they can take-off and land even when there is no wind.

Altaeros Energies is a US-based startup working on this concept by using balloon with a turbine mounted inside it [31]. The Altaeros design does not involve a crosswind motion and is a static system harnessing the high altitude wind power. Figure 2.16



Figure 2.15: Ampyx AP2 Prototype [23].

shows their ballon Torus with a turbine rotor mounted inside it.



Figure 2.16: Altaeros Prototype [31].

Omnidea Lda. founded in 2007, is a Portuguese company working on the ground-based generation system using lighter than air Magnus cylinders as an airborne platform [25]. The lift generated by the Magnus effect is used to make the cylinder perform a Yo-Yo cycle. The traction power developed in the tether is used to drive the ground-based generator. Figure 2.17 shows Omnidea's 16 m long Magnus-based prototype. The Magnus-based AWE systems are discussed in detail in Chapter 3 and 4.

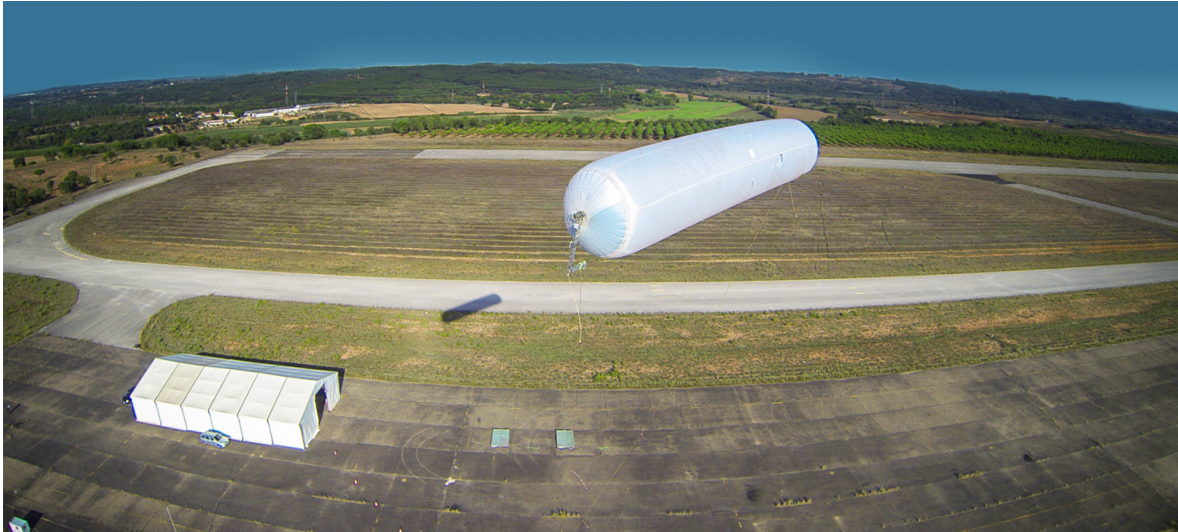


Figure 2.17: Omnidea Prototype [25].

4. Other Innovative concepts

Apart from the usage of conventional flying surfaces, there are many startups working on the different innovative concepts to achieve high lift. Bladetips energy is using fixed wing in rotary configuration as an airborne platform [38]. Dual Drone concept proposed by Antonello Cherubini uses two UAVs to maximize the lift [32]. Wind Fisher is working on the concept of using Magnus-based AWE systems for maritime applications [39]. There are several other innovative design concepts and applications which are currently being researched upon.

2.2 Basic Concepts

In general, irrespective of the type, each airborne wind energy system is governed by similar set of principles. In this section, some basic concepts of AWE technology are discussed, knowledge of which is necessary to understand the AWE technology. They can be broadly characterised as:

1. Configuration of AWE systems,
2. Power Generation,
3. AWE Operational Cycles.

2.2.1 Configuration of AWE Systems

Each type of AWE system consists of three main components, namely:

- Airborne platform,
- Tether or cable,
- Ground station.

There are various methodologies used in literature for the analysis and design of each of these components. To develop a better understanding of the basic concepts of AWE technology some general approaches and basic models most commonly used in literature are discussed in this section.

- **Airborne Platform:** Irrespective of the choice of the airborne platform used kite or UAV or lighter than air or any other innovative design. The modeling of the airborne platform of AWE system is performed by using the classical flight dynamics approach. M. Lyod presented a basic modeling approach in [10]. In [40], a simple model for the Laddermill AWE concept is presented. Reference [41] and [42], gives a detailed 6-DOF model adapted from the flight dynamics for modeling AWE kite systems. Reference [43],[44], present a 3-DOF model based on the spherical coordinate system for kite planes adapted from soft inflatable kites. Reference [45],[46], discusses the system model for a UAV based AWE systems derived from the lagrangian approach and [47] presents the 6 DOF model for UAV based systems derived from the first principles of flight dynamics. Reference [34],[48], [49], discusses a 3-DOF control-oriented modelling approach. In [50],[51],[52], modelling approach for Magnus-based AWE systems is discussed. All the approaches describe the system by using the Newtonian approach and considering two frames of reference, namely, an inertial frame fixed at the ground with respect to which the position of the airborne platform is described, and a body frame centered at the C_g of the airborne platform. In case of multi-line kite systems, when a control pod is used at the bridle-point [41], another intermediate frame centered at the bridle point is used to describe the movement of the bridle point, and in some cases attitude of the platform is then expressed with respect to this intermediate frame centered at the bridle point.

A common approach used to describe the motion of the kite or UAVs for designing the guidance laws or for optimization of the trajectory is by using spherical coordinate systems. Where in this work, the elevation angle is denoted by θ_T , and the azimuth angle is denoted by ϕ_T . These two angles are then used to describe the orientation of tether with respect to the ground as given by the equations below and shown in figure 2.18. Many control strategies are proposed in the literature based on this model such as [34] as used in this thesis work.

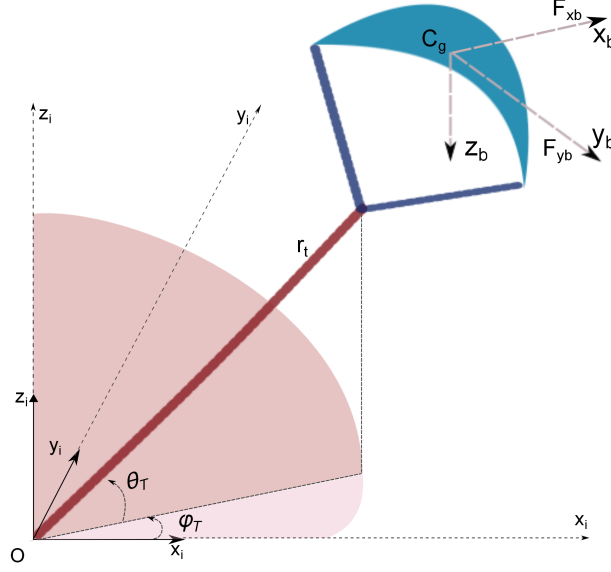


Figure 2.18: Kite based AWE System.

$$\vec{x} = \begin{bmatrix} r_t \cos(\phi_T) \cos(\theta_T) \\ r_t \cos(\phi_T) \sin(\theta_T) \\ r_t \sin(\theta_T) \end{bmatrix} \quad (2.1)$$

By applying Newtons law of motion:

$$\ddot{\theta}_T = \frac{\vec{F}_{x_b}}{r_t m} - \sin(\theta_T) \cos(\theta_T) (\dot{\phi}_T)^2 \quad (2.2)$$

$$\ddot{\phi}_T = \frac{\vec{F}_{y_b}}{r_t m \cos(\theta_T)} + 2 \tan(\theta_T) \dot{\theta}_T \dot{\phi}_T \quad (2.3)$$

Where, \vec{x} represents the position vector of the C_g , r_t is the tether length, m is the mass of the airborne platform. \vec{F}_{x_b} and \vec{F}_{y_b} presents the forces in the body frame centered at the C_g of the airborne platform. A detailed model can be found in [34],[48],[53],[54].

- **Tether:** In the ground-based systems, a tether is used to control the kite as well as to drive the generator. In on-board systems besides from control, the tether is used to transmit the electricity generated by the on-board generator. Thus, depending on the type of the system, the specifications of the tether vary. In general, the tether should be made of a material which can not only bear high loads but also is lighter in weight. Tether cables made of composite materials are generally used in the AWE prototypes. Tether dynamics play an important role in determining the efficiency of AWE system. To minimize the effects due to the drag, inertia and elastic properties of the tether, its diameter must be as small as possible.

In case of kite based AWE systems, there is also some debate about the optimal number of tethers that should be used for control purposes [56]. As less number of tether affects the controllability of the kite system whereas using more than one tether increases the

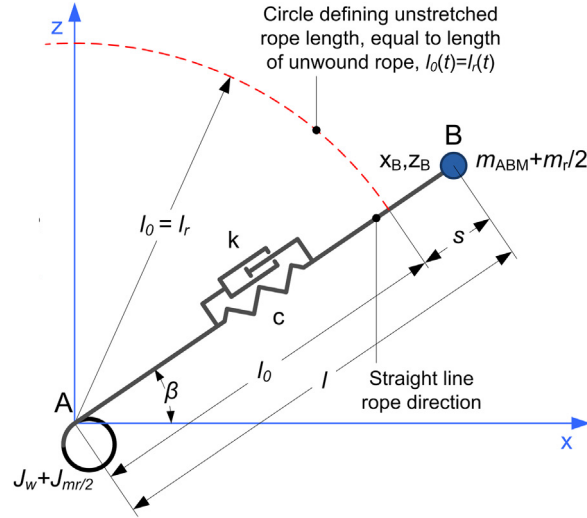


Figure 2.19: Straight line rope model taken from [55].

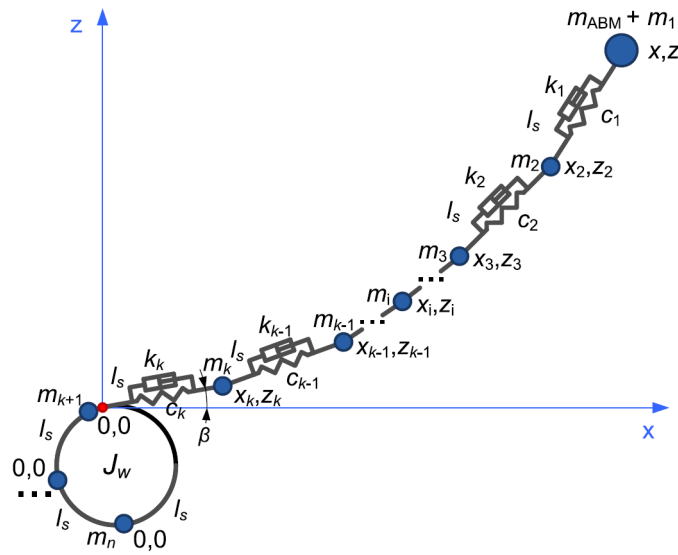


Figure 2.20: Multi-mass rope model taken from [55].

tether drag. Thus, decreasing the overall efficiency of the system. There are several models proposed in the literature for modelling the tether dynamics [57], [42],[58],[59]. Reference [55], presents two approaches to model the effects of tether for a Magnus-based system. The lumped mass model, as presented in figure 2.19, considers tether as a simple spring-damper system. In the multi-link model, the tether is modeled as a series of spring-damper point mass system, taking into account the sagging effect of the tether as shown in figure 2.20. A detailed analysis of the elastic properties of the tether is presented in [44]. In [59], a study of the effect of tether length on the flight is presented. The work also discusses the tether design methodology. Other similar modeling approaches are discussed in [42],[60].

- **Ground Station:** At ground station the tether is reeled-in and reeled-out. In case of ground-based systems, the ground station consists of a winch-generator system. Winch uses the traction force of the tether to drive the generator. In on-board systems, the winch is only used to pull down the airborne platform. Figure 2.22 presents the driveline components of a ground station. The choice of the ground station components depends on the specification of the AWE system and the maximum power generated. In [61], a design strategy for the ground station components for a 20 KW maximum power kite is discussed. Reference [55], discusses a simple winch dynamics model considering a lumped mass tether model. In [50], a simple approach for modelling the winch dynamics is presented as shown in figure 2.21 and given by equation 2.5.

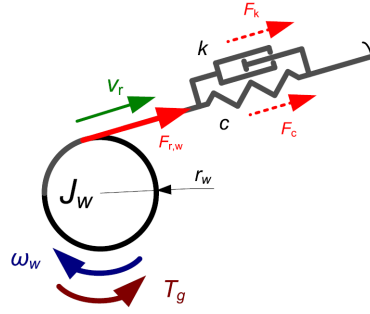


Figure 2.21: Winch model taken from [55].

$$\dot{l}_r = \vec{v}_r \quad (2.4)$$

$$\dot{\vec{v}}_r = r_w \dot{\vec{\omega}}_w = \frac{r_w}{J_w} (r_w \vec{F}_{r,w} - \vec{T}_g) \quad (2.5)$$

Where, l_r is the unwound tether length, J_z is the moment of inertia of the winch, v_r is the winding or unwinding speed of the tether, $F_{r,w}$ is the traction force sum of the tether elastic and damping forces (F_c and F_k), and T_g is the generator torque. There are several types of generators available in the market which can be used for the energy conversion. The choice of type of ground station has a big effect on the Levelized Cost of Energy (LCOE). Reference [62], discusses the effect of different energy conversion methods on the overall efficiency of the AWE system. In [63], the efficiency of two types of permanent magnetic generators for a small scale AWE system is discussed. Reference [64], compares the various driveline solutions for conventional wind turbines and based on the works of [65], [66], presents two ground station layout for kite based AWE systems. For each layout, LCOE is computed and respective power curves are presented.

2.2.2 Power Generation

The key idea behind the power generation is as the airborne platform moves around in the air, the electro-mechanical systems convert the high altitude wind speed into electricity. As

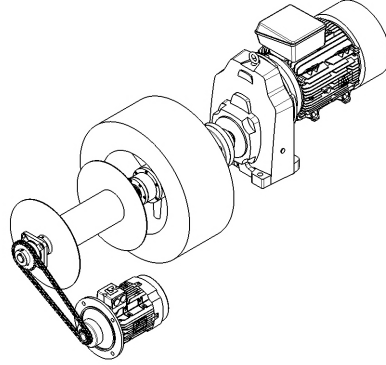


Figure 2.22: Ground station driveline taken from [61].

in the conventional wind turbines, the power produced depends on the relative wind speed experienced by the airborne platform, which in turn leads to higher lift and drag forces. Thus, in the case of ground-based systems, it leads to the production of higher traction force. In literature, power produced by the AWE systems is given by:

$$P = F_r v_a \quad (2.6)$$

Where, v_a is the apparent wind velocity faced by the airborne platform, and F_r is the total traction force developed in the tether. F_r directly depends on the aerodynamical forces F_a developed in the airborne platform.

$$F_a = \sqrt{F_L^2 + F_D^2} \quad (2.7)$$

$$F_L = \frac{1}{2} \rho S v_a^2 C_L \quad (2.8)$$

$$F_D = \frac{1}{2} \rho S v_a^2 C_D \quad (2.9)$$

Where, F_L and F_D represent the lift and drag force, C_L and C_D are the aerodynamic coefficient of lift and drag respectively, and S is the surface area. In [10], Lyod calculated the approximate theoretical power produced by such systems by:

$$P = \left(\frac{4}{27}\right) \rho S (v_w)^3 C_L \left(\frac{C_L}{C_D}\right)^2 \quad (2.10)$$

Where, v_w is the wind speed experienced by the airborne platform and ρ is the air density. The equation 2.10 is derived by assuming for the maximum power generation the apparent wind velocity v_a must be maximized. It is further detailed in [10] and explained in chapter 5. As observed from the above equation the power produced is a function of surface area, relative wind velocity v_a , and aerodynamic coefficients $\left(\frac{C_L}{C_D}\right)^3$. Thus, higher they are higher is the power produced. These parameters can be maximized by:

- Crosswind Motion,
- Lift-to-drag ratio,

- Surface area.

Crosswind Motion: One way to maximize the power is to maximize the wind experienced by the airborne platform. Doubling the average wind speed results in an eightfold increase in the energy output of the AWE system and tripling the wind speed leads to 27 times increase in the power. Crosswind motion maximizes the experienced average wind speed, thus, leading to higher power production. Basically, in crosswind motion, the airborne platform flies transverse to the direction of the apparent wind .i.e. having a component of wind perpendicular to the line of travel. As the lift force is a square function of the apparent wind, this results in higher lift which leads to higher power generation. This is primarily because in crosswind flight the airborne platform traverses a higher volume of the wind field, also known as swept area. In other words, it harvests wind energy from an area exceeding its own size. This ability of AWE systems gives it an edge over the conventional wind turbines where the swept area is limited by the fixed size of the blades. The two main trajectories to achieve crosswind motion is eight-figure loops and circular orbit both of which are explained in detail in chapter 4.

Lift-to-drag ratio: Another way to increase the power produced is by increasing the C_L and decreasing the C_D . As doubling the lifting capabilities leads to a direct increase in the power generated as expressed by the expression $(\frac{C_L}{C_D})^3$. However, higher lift force also leads to higher drag force. This is partly because higher volume of wind fluid is disrupted which results in higher frictional forces, thus, higher drag. The ratio of $\frac{C_L}{C_D}$ called as Lift-to-drag ratio presents the effectiveness of any surface in a fluid medium (which in case of AWE systems is the atmosphere) and is used to quantify the performance of any lifting surface in a fluid medium. As power produced is proportional to the square of $\frac{C_L}{C_D}$, the lift-to-drag ratio serves as a critical indicator in choosing the airborne platform such as soft kite, hard-wing, UAV, Magnus cylinder, etc. The choice of airborne platform with high $\frac{C_L}{C_D}$ directly affects the power generation capability of the system. The power production and performance of AWE system are discussed in detail in chapter 5.

Surface Area: The other way of achieving higher power is simply by increasing the size of the AWE system. Thus, scalability also plays an important role in the choice of airborne platform.

2.2.3 AWE Operational Cycles

Generally, the operation of ground-based AWE system is characterized by two operating phases as shown in figure 2.23. The power is generated in the power generation phase, also called the production phase, where the airborne platform gains altitude while performing the crosswind motion or following any other specified trajectory. This phase is characterized by the reeling out of the tether from the drum.

When the airborne platform attains the maximum altitude, it is required to be pulled back. This marks the beginning of the recovery phase when the drum motors pull back the airborne platform .i.e. the reeling-in of the tether. In this case, the drum consumes a part of the energy

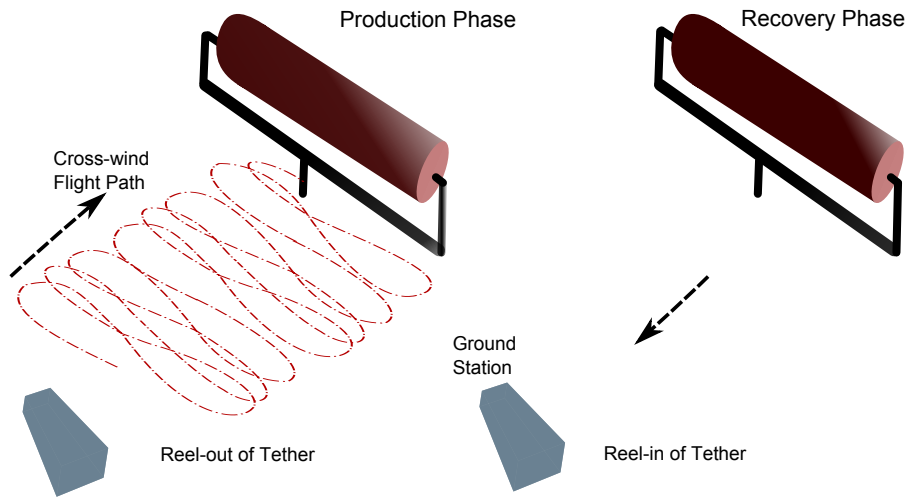


Figure 2.23: Operating cycles of AWE.

produced during the production phase. Hence, one complete cycle of operation comprises of power production and consumption phase. The net power produced in one complete cycle is then the sum of the power produced and power consumed as shown in figure 2.24.

Several strategies have been proposed in the literature to minimize the power consumption during the recovery phase. The basic principle behind all such strategies is to deliberately decrease the lift produced by the airborne platform before starting the reeling in of the tether. Thus, decreasing the resistive forces and the energy consumed during the recovery phase. One way of achieving this objective is by deploying the lift-reducing control surfaces such as

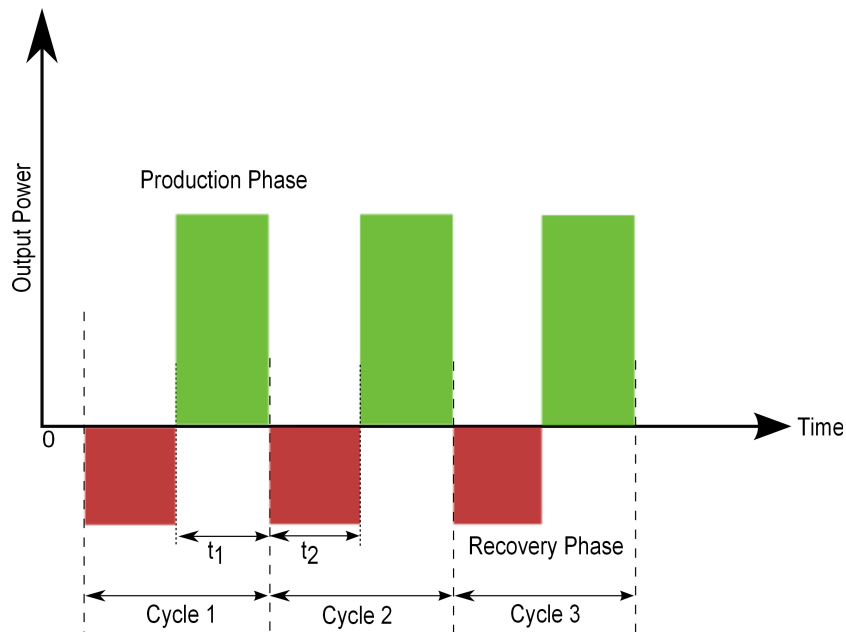


Figure 2.24: Power cycle for AWE system.

spoilers in case of UAV base AWE systems. Another way is by carrying out certain manoeuvres which leads to a fall in lift such as by increasing angle of attack greater than the stall angle as in the case of soft kites.

2.3 Challenges

There are several major challenges in front AWE community before a full-scale AWE wind farm can be established. Various research teams and startups around the world are working to solve them.

1. Landing and Take-off strategy:

Although several approaches have been proposed in the literature for the landing and take-off of AWE systems but still it is an open topic of research in AWE community. Reference [67] presents an analysis of four take-off approaches. Reference [68], presents a landing and take-off strategy for Multi-drone systems. Ampyx power is working on the landing and take-off approach from a rotating platform as discussed in [69]. Reference [70], presents in detail rotation start approach. In [20], an approach using artificial air blowers is proposed. The approach aims to create artificial wind during the take-off. Reference [71], presents a take-off approach using an aerostat. TU Delft team has patented an upside-down launching strategy in 2014 described in detail in [72]. Makani Power [17] uses the on-board turbine propellers as a motor for take-off and landing with power being supplied from the ground-based system for this phase transition. A similar approach is discussed in [73].

However, still there is no coherent strategy for the autonomous landing and take-off for AWE systems. Also, there are several open questions regarding the landing and take-off strategy which needs to be addressed such as landing and take off in situations when there is no wind or excess wind, bad weather, etc.

2. Autonomous Operation:

Despite the presence of many working prototypes, a 24x7 autonomous operation of an AWE system has not yet been attempted. The longest flight test is done by Makani which was for 3 days. Also, the performance and autonomous operation strategy for an AWE system in scenarios such as low wind or an excess wind, or bad weather conditions like rain, storm etc. are yet to be explored. In all such cases, the AWE system must be capable of autonomously landing and taking-off by itself.

3. Autonomous Control of Trajectory:

In literature there are plenty of control strategies available to achieve an optimized crosswind trajectory but due to the lack of flight test data and the limited number of functional prototypes many such control strategies are yet to be verified. Hence, there is no consensus on the best control practice needed for autonomous operation.

4. Tether Dynamics:

Tether drag is a big contributing factor to the efficiency of the AWE system. However, there is limited research done in this regard and there is even lesser experimental data available on the contribution of tether drag to the overall AWE system. In addition, most of the flight test done by the companies usually do not consider the effects of tether dynamics. To achieve an efficient AWE system, tether dynamics would play a key role. Thus, its contribution to the performance of the AWE system must be thoroughly studied.

5. Life Cycle Predictions:

As currently, the focus of AWE research teams and startups is to achieve a fully automated flight, for now there is very less information available on the life cycle of the various components involved in the AWE systems such as the tether, airborne platform etc. which will be a key factor in determining the LCOE of the AWE systems.

6. Ground station specification:

Although there are several off-the-shelf generators available in the market, but as there is a lack of data available about the performance of AWE systems there is still no coherence on the specifications of the ground station. Also, there are several strategies being proposed in the AWE community regarding the driveline and winch-generator design such as usage of a gearbox, hydraulic transmission, storage device, use of multiple electric motor/ generator, etc. which are needed to be verified.

7. Policy Regulations:

As the AWE system is a novel technology and requires an airborne platform to fly at high altitudes, there are several restrictions imposed on the usage of airspace which impedes the flight testing of the prototype. Also, for the development of AWE based wind farms, new policies need to be made which eases the usage of airspace as well as the ground site.

8. Economic Indicators:

AWE systems face a direct comparison with conventional wind turbines. There are several economic indicators which evaluate the performance of wind turbines like LCOE, capacity factor, power coefficient, etc. As for now, there are very less studies undertaken on the economic feasibility of the AWE system. Also, in the research community there is still a debate whether the classical performance indicators developed for conventional wind turbines can be applied to AWE systems or not.

The main objectives of the thesis work are:

- Study and validation of the aerodynamic model of the Magnus Effect.
- Development of a 3-D Mathematical model for Magnus-based AWE system.
- Design of guidance control for Magnus-based AWE system.

- Study of operating strategies for maximum power production of AWE system.
- Development of the power curves for Magnus-based AWE systems.

By achieving the above mentioned objectives, this thesis work aims to address the challenges and issues related to:

- Modelling and design of AWE systems,
- Autonomous operation of AWE systems,
- Ground station layout and configurations,
- Economic capability of AWE systems.

Magnus-Based AWE Systems

Contents

3.1	Introduction	31
3.2	Magnus Effect	32
3.3	Aerodynamic Characteristics of Magnus Effect	37
3.3.1	Aerodynamic Coefficients of Magnus Cylinder	39
3.4	Aerodynamic Model	44
3.4.1	Comparison of Experimental Aerodynamic Data	45
3.4.2	Estimation of Aerodynamic Coefficients using EKF	48
3.5	Gipsa-lab Experimental Setup	49
3.5.1	Wind tunnel	49
3.5.2	Ground station	49
3.5.3	Magnus cylinder	50
3.5.4	Results	50
3.6	Conclusion	56

3.1 Introduction

As discussed in chapter 2, a ground-based AWE system consists of a wing or a kite (flexible or rigid) attached to one or more cables connected to the electric generator on the ground. This type of system allows for the aerial part to be light and the use of conductive cable is avoided. A Magnus effect-based system as studied by Omnidea Lda. [25] consists of a lighter than air airborne platform. The operating principle of the platform is based on the traction force of a rotating cylindrical balloon employing both aerostatic as well as aerodynamic lift mechanism. The feasibility of concept has been studied in reference [51],[74],[75], etc. The authors of [50] have optimized control variables for a Magnus effect-based AWE system following optimal vertical trajectories. In [52], a strategy is proposed to control the power produced by the system by changing the tether length and the cycle period.

In order to develop a realistic simulation model and evaluate the performance of Magnus-based AWE system, it is necessary to have a very good understanding of the aerodynamic properties of Magnus effect, particularly the coefficient of lift and drag. However, as to be

discussed in detail in this chapter, very less research data is available in this regard. In this chapter, a detailed analysis of the aerodynamic properties is presented. To establish a good aerodynamic model for Magnus effect, a two-step approach comprising of the analysis of historical experimental data and an estimation strategy is presented. The results obtained from this two-step approach (which includes in-depth analysis of the past research on various Magnus based systems, including applications in naval engineering, aeronautics, renewable energy etc.) are our contribution to the research on Magnus effect. And to the best of our knowledge, this is the first comprehensive study undertaken with a focus on Magnus based AWE system. Thus, the results obtained about the aerodynamic properties of Magnus-based AWE systems are first of its kind in the literature on Magnus-based AWE systems.

In this chapter, a detailed description of the Magnus effect and its application is presented in section 3.2. In section 3.3, the aerodynamic properties of the Magnus cylinder are discussed. Section 3.4 presents the comparison of historical experimental data with an aerodynamic polynomial model for Magnus cylinders and an estimation strategy adopted to estimate and better understand the aerodynamic coefficients of a Magnus cylinder. Section 3.5 presents the experimental setup at GIPSA-lab as well as discusses the results obtained by the estimation approach. The chapter concludes with a conclusion presented in section 3.6.

3.2 Magnus Effect

Historically, the phenomenon of Magnus effect was first mentioned by Issac Newton in 1671 in his letter Oldenburg, where he explained the spinning motion of the tennis ball [76]. Subsequently, in the 19th century it was well known that the projectile motion of a bullet or a gun shell is described by a parabola and air resistance has a considerable effect on the path. In 1805, Benjamin Robins described the whirling motion and deflection of a bullet in the air in his paper [77], what can now be called as 'Robins effect', [78]. However, the phenomenon

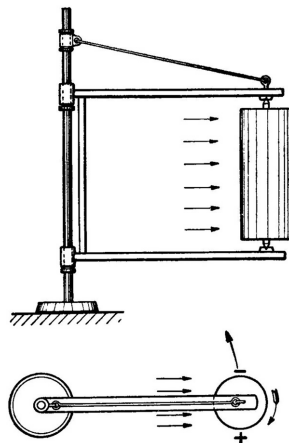


Figure 3.1: Gustave Magnus's experimental setup [79],[80].

was first defined by German scientist Gustav Magnus in 1852 [79], hence, the name Magnus

effect. In his experiments he noticed a lateral force arising due to the spin of the cylinder. He explained that the spin of the cylinder causes an unequal distribution of pressure around the top and bottom surface of the cylinder which results in a lift force similar to the one produced by airfoils when exposed to wind flow. This lift force is sometimes called as the Magnus force. Figure 3.1 presents his experimental setup.

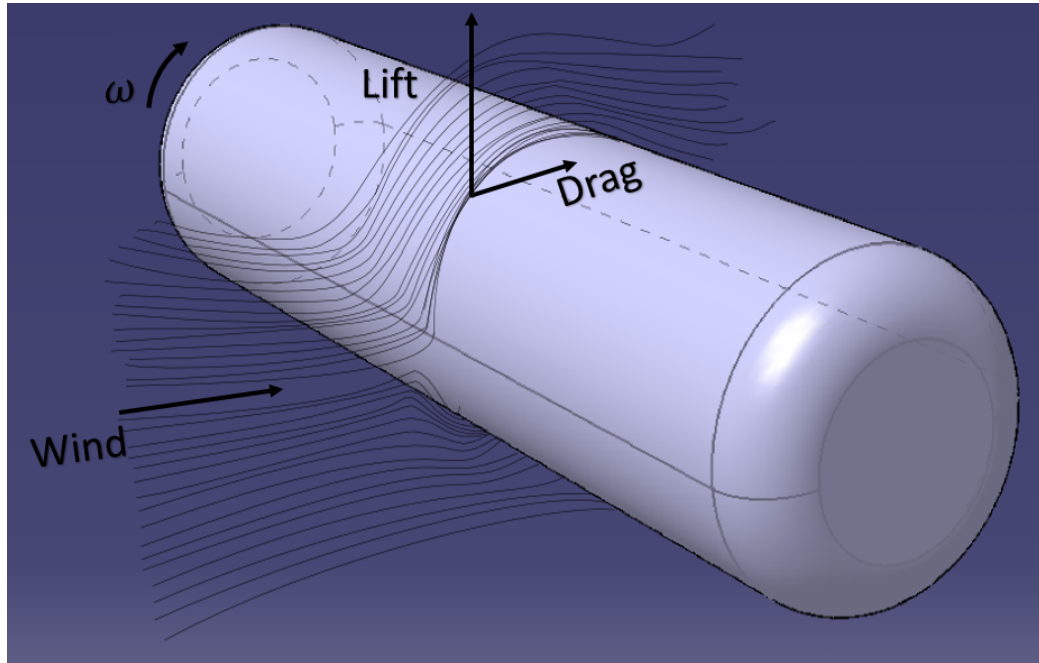


Figure 3.2: Magnus Effect.

The interest in the Magnus effect renewed in the last century particularly due to its advantage over classical lifting devices such as airfoils. Figure 3.3 presents the comparison of the maximum lift coefficient produced by different surfaces. As it can be observed from the figure 3.3 Magnus effect-based devices can achieve a very high coefficient of lift. This inspired many researchers, inventors, and engineers to explore its potential and to create systems tapping wind energy to steer ships, drive wind turbines, and develop high lifting devices for aeronautical applications. In 1877, Lord John Rayleigh in his work tried to explain the curved motion of a ball using Magnus effect [82]. Lafay in 1912 conducted experiments on the rotating cylinders at Ecole Polytechnique and successfully demonstrated the high lift force generated by it as compared to that by the airfoils of same projected area. Similar research works by Hermann Fottinger [83], and Prof. Gumbel [84], in 1918 and 1919 on rotating cylinders led to the development of propellers using rotating cylinders.

One of the most prominent research exploring the potential of the Magnus effect was done by Anton Flettner in the 1920s. Flettner attempted to use the Magnus effect to propel ships. He developed a propulsion system based on cylindrical rotors, now known as Flettner Rotor. Under his leadership, a ship named Buckau (renamed Baden-Baden shown in figure 3.4), using two large cylindrical rotors of about 15 meters height and 3 meters in diameter, was constructed in 1924, which in 1926 made a voyage to New York harbor via South America.

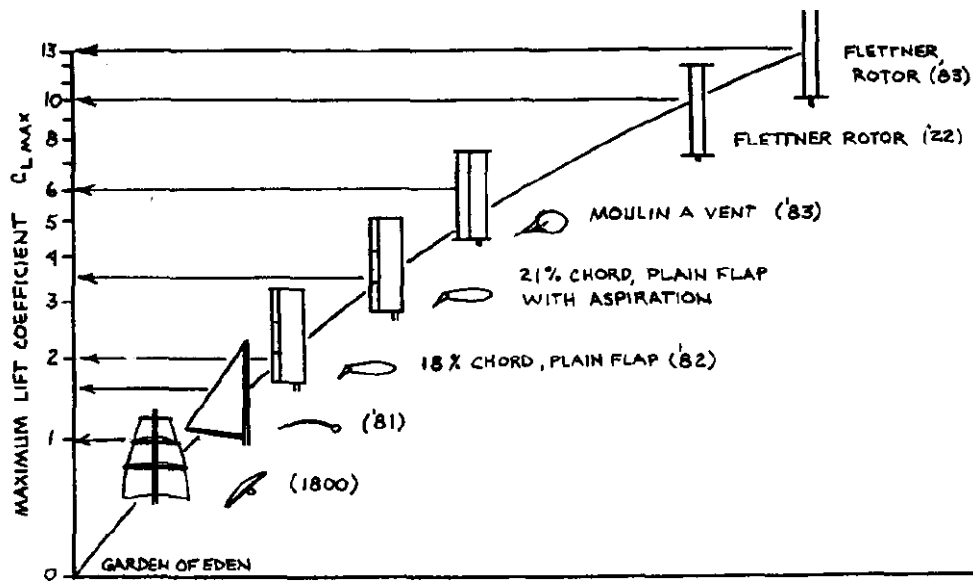


Figure 3.3: Maximum coefficient of Lift (C_L) for different lift generating devices [81].

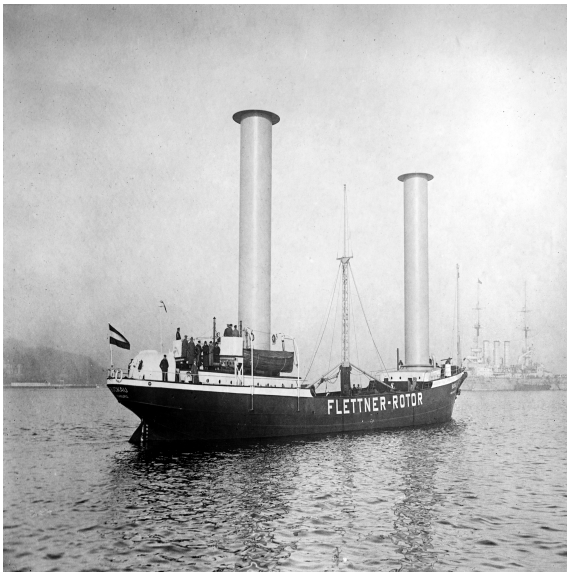


Figure 3.4: MS Buckau (Baden-Baden) [85].

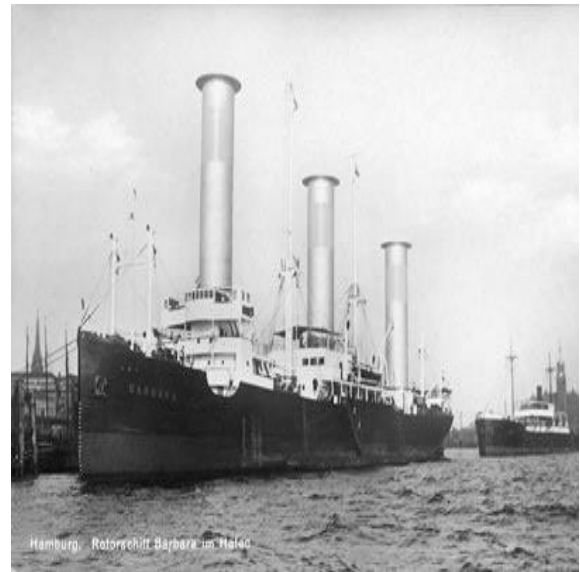


Figure 3.5: Barbara Ship [86].

During world war II, he headed Flettner Flugzeugbau GmbH, which developed helicopters and aircrafts using Magnus effect, as shown in figure 3.6 and 3.7. In the late 20th century with the renewed interest in the potential of Magnus effect, an attempt was made again to use it for naval propulsion. In 1980, Jacques-Yves Cousteau proposed Turbosail [87], a naval propulsion system inspired by Magnus effect with design similar to that of the ship Buckau. He commissioned a test vehicle Alcyone, shown in figure 3.8, using Turbosail propulsion system. E-ship 1, as shown in figure 3.9, is another vessel using the Magnus effect to propel the ship. It consists of four large Flettner rotors of about 27 meters height and 4 meters in diameter.

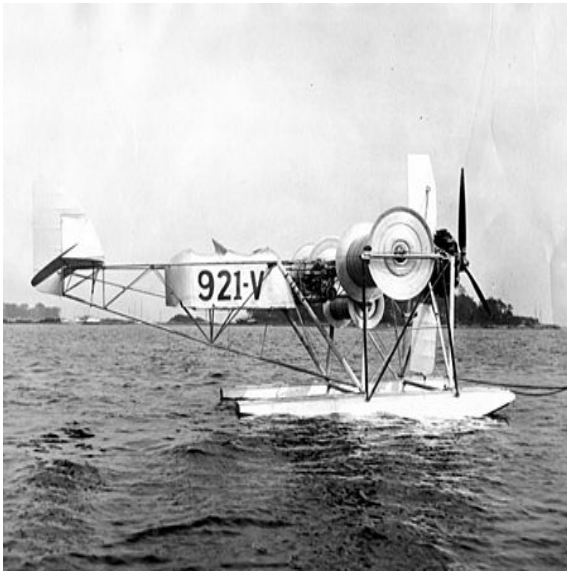


Figure 3.6: Flettner Rotor Aircraft [86].



Figure 3.7: Flettner F1 282 Kolibri [86].

The rotors via a mechanical linkage convert the wind energy and use it to propel the ship. It is operated by Enercon since 2010 as a cargo vessel for transporting wind turbine components.



Figure 3.8: Alcyone vessel [88].

Norsepower Ltd. is a Finnish clean technology company established in 2012 and funded under the EU's H2020 framework. They are pioneer in providing Magnus effect based rotor solution for ship propulsion [89]. Their rotor based propulsion system claims to be easy to use, low maintenance and promises to provide an average of 6% to 20% fuel savings in ship propulsion. Their installed rotor based systems on a Viking cruise ferry claims to provide an annual LNG fuel reduction by 300 tonnes. A Ro-Ro vessel Estraden is also using their rotor propulsion system with two 18 meter tall Magnus rotors leading to verifiable fuel savings by 5% and 460 kW average power boost. Recently in 2018, they have installed two 30 m long

Magnus cylinder on Maserk tanker as shown in figure 3.10, which are expected to reduce 7-10% of average fuel consumption. In 2012, Jost Seifert presented a paper describing in detail



Figure 3.9: E-Ship 1 operated by Enercon [90].



Figure 3.10: Maserk tanker with installed rotor propulsion system by Norsepower [89].

some Magnus effect-based technologies which had been researched upon in the last century including wind turbines, aircraft, etc., [80]. He also suggested that there is a lack of research on how to the design and model lifting devices using the Magnus effect.

In 2014, Sedaghat presented a novel concept of Magnus effect-based wind turbines [91]. He proposed a horizontal axis wind turbine consisting of Magnus cylinders as turbine blades, as shown in figure 3.11. The work concluded that the Magnus wind turbines have a merit over conventional wind turbines but for small-scale applications. However, for a large-scale wind turbine, a thorough experimental study of the aerodynamic properties of the Magnus effect is needed. In [92], a Magnus based MAV is studied.

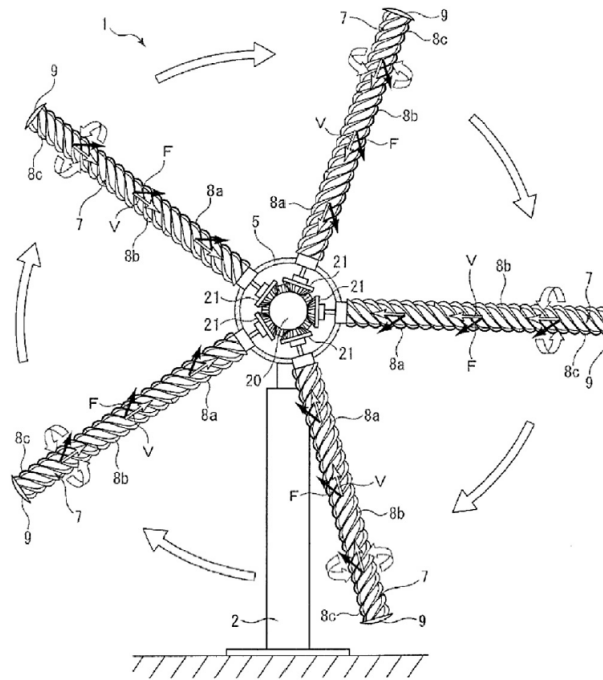


Figure 3.11: Conceptual Wind Turbine, [91].

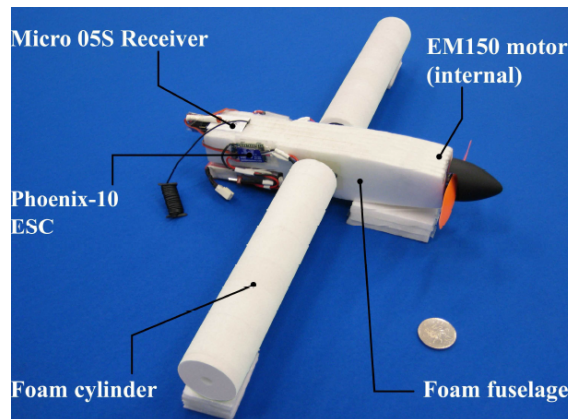


Figure 3.12: Prototype of Magnus based MAV as proposed by Badalamenti, [92].

3.3 Aerodynamic Characteristics of Magnus Effect

In order to establish a control oriented mathematical model for Magnus-based AWE systems and to approximate the power generated by them. It is imperative to study the aerodynamic characteristics of Magnus effect to determine the coefficient of lift, C_L , and drag, C_D . These dimensionless variables determine the lift and drag force generated by the Magnus cylinder which in turn determines the traction force available to drive the on-ground generator, as explained in later sections. This requires the study of flow past rotating cylinders in high Reynolds number regime. Similar to the airfoils, the lift and drag force acting on the Magnus

cylinder are expressed as:

$$F_L = \frac{1}{2}\rho S_{cyl}v_a^2 C_L, \quad F_D = \frac{1}{2}\rho S_{cyl}v_a^2 C_D \quad (3.1)$$

Where, v_a is the relative airflow impinging on the Magnus cylinder, ρ is the air density, and S_{cyl} is the projected surface area of the Magnus cylinder in the direction of the apparent wind velocity. C_L and C_D represent the coefficient of lift and drag respectively.

Apart from this, a torque (T_{motor}) is required to turn the Magnus rotor and it can be estimated by:

$$T_{motor} = \frac{1}{2}\rho S_{cyl}r_{cyl}^2 v_a^2 C_m \quad (3.2)$$

Where, r_{cyl} is the radius of the Magnus cylinder, ω_{cyl} is cylinder's angular spin velocity, and C_m is the aerodynamic torque coefficient of the rotor that depends mainly on spin ratio X and Reynolds number (explained below), geometry of the cylinder and, roughness of its surface. Generally, its value is determined by the wind tunnel testing or CFD analysis. It is further detailed in chapter 5 and section 5.2.3.3.

In particular, for Magnus effect, the aerodynamic coefficients, C_L , C_D , and C_m , depend on two dimensionless quantities namely, the Spin ratio (X) and Reynolds number (Re).

Spin ratio: Contrary to the airfoils, where C_L and C_D are primarily the functions of its angle of attack and shape, in case of Magnus effect these coefficients primarily depend on the dimensionless quantity, spin ratio X . The spin ratio X is defined as:

$$X = \frac{\omega_{cyl}r_{cyl}}{v_a} \quad (3.3)$$

Where, r_{cyl} is the radius of the Magnus cylinder. This gives Magnus-based AWE systems an advantage over other systems such as airfoils. The geometrical symmetry of the cylinder and independence from the angle of attack makes them insensitive to the apparent wind direction and, thus, more robust to the wind gusts. For Magnus-based AWE systems, the spin ratio is expected to be between $[0, 8]$.

Reynolds Number: Another parameter that influences the C_L and C_D coefficients is the dimensionless quantity Reynolds number (Re), which is the ratio of inertial forces to viscous forces within a fluid. It is used to quantify the flow characteristics in fluid mechanics. A low Reynolds number indicates that the fluid flow is laminar or streamline, whereas a high Reynolds number is indicative of turbulent flow. The critical Reynolds number is used to predict the transition from streamline to turbulent flow. The knowledge of the fluid characteristics, particularly, when the flow transitions from laminar to turbulent flow, plays an important role in engineering design. For instance, the design characteristics of an airfoil, such as length, width, etc., are chosen based on the knowledge of its critical Reynolds number. It is also used in scaling full-scale models to test models, or vice-versa, for different objects. It is expressed as:

$$Re = \frac{\rho u L}{\mu} \quad (3.4)$$

Where, u is the fluid velocity, μ is the dynamic viscosity of the fluid, ρ is the density of the fluid, and L is the characteristic length of the object. The operating Reynolds number for Magnus-based AWE systems is expected to lie in high Reynolds number regime between the range of 5×10^5 to 10^7 .

3.3.1 Aerodynamic Coefficients of Magnus Cylinder

There is a rich literature available on flow past rotating cylinders in low Reynolds number regime .i.e. $Re < 1000$ (in contrast to high Reynolds number), which provide an important insight about the flow characteristics past a rotating cylinder. However, these studies have been particularly focused on the application of rotating cylinders for the control of boundary layer. Some important studies for low Reynolds number regime from 5 to 200 are presented in papers [93], [94],[95], which discusses in detail the properties of the flow past rotating cylinder. The results presented by Ingham and Tang for Reynolds number 5 to 20, and spin ratio, 0 to 0.5 provide an important insight about the flow lines and fluid interaction with rotating surfaces [96].

As the Reynolds number rises the flow complexity increases which makes the experimental determination and validation of the aerodynamic coefficients very difficult. For moderate Reynolds number $1000 \leq Re \leq 10000$ there are some significant studies available in the literature. In Badr et al. [97], an experimental and numerical analysis for $10^3 \leq Re \leq 10^4$ is presented. Other similar studies such as [98], [99] and [100] present their results for moderate Reynolds number range. However, there is a lack of published data dealing with rotating cylinders in high Reynolds number regime. Primarily, because of the lack of interest of fluid dynamicists, and secondly, due to the turbulent nature of the flow which makes the problem more complex. For such type of flows, it is observed that the critical Reynolds number occurs around $Re = 3 \times 10^5$, [101].

In 1925, L. Prandtl conducted an early experimental study of flow past a rotating cylinder [102]. Prandtl performed experiments for low rotational speeds and due to flow separation in downstream, he concluded from his experiments that the maximum lift from a spinning cylinder cannot exceed 4π . In 1991, Tokumaru and Dimotakis contradicted the Prandtl's conclusion, [103]. In their study for Reynolds number, $Re = 3.8 \times 10^3$, and spin ratio, $X = 10$, they demonstrated that the lift forces higher than 4π can be achieved. Other similar studies have also validated Tokumaru and Dimotakis's findings.

In [104], it is concluded that the mean lift occurs around $Re = 2.8$ to 3.5×10^5 , and the phenomenon of Drag crisis, where drag coefficient (C_D) drops rapidly, comes into play in this Reynolds number range. And around $Re = 3.8 \times 10^5$ due to the increase in the shear stresses due to turbulence the drag coefficient increases again.

In [105], Karbelas published his results on flow past spinning cylinder for high Reynolds number $Re = 1.4 \times 10^5$ and spin ratio, 0 to 2. In [101], he investigated the flow for $Re = 5 \times 10^5$, 10^6 , 5×10^6 , and for spin ratio, $X = 0$ to 8. He concluded that the lift coefficient, C_L , increases linearly with respect to the spin ratio while the coefficient of drag, C_D , increases linearly from

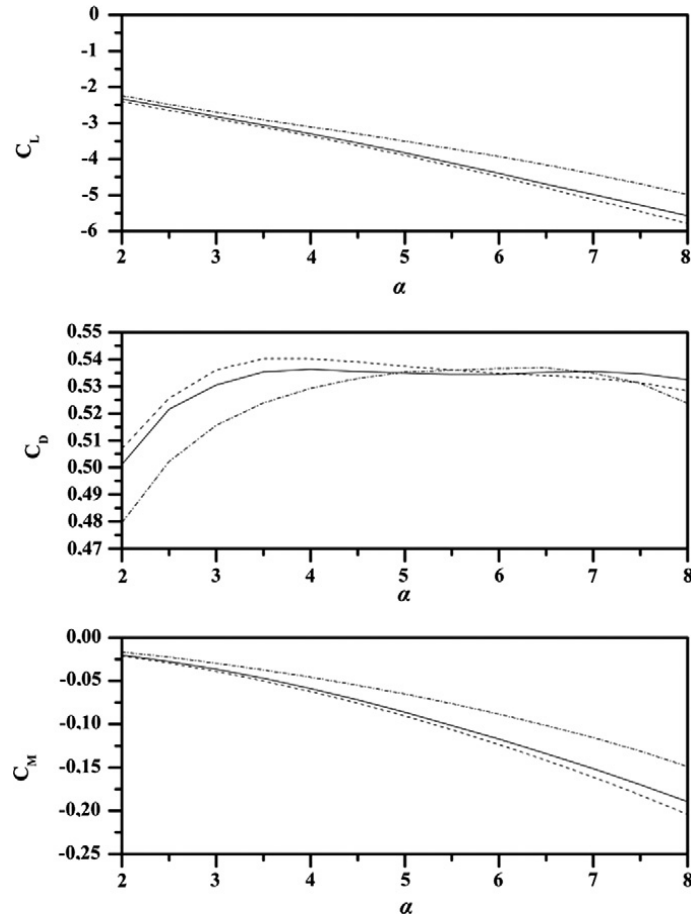


Figure 3.13: Lift, Drag and Moment Coefficient, C_L , C_D and C_m for $Re = 5 \times 10^5$ (dash line), $Re = 10^6$ (solid line) and $Re = 5 \times 10^6$, α is the spin ratio [101].

$X = 0$ to 4, after which it reaches a plateau, and then decreases around $X = 7.5$. Figure 3.13 presents his results.

In [51], Luka Perkovic et al. presented the results of CFD analysis of a Magnus-based AWE systems for $Re = 10^6$, 5×10^6 , 10^7 , and spin ratio, $X = 0$ to 7. They considered a cylinder of radius 3 m and 30 m in length. Figure 3.14 presents their results for different Reynolds number. In [106], [107] an analysis of the aerodynamics of Flettner rotor for high Reynolds number is presented. Elliott G. Ried in 1924 conducted a study of the Magnus effect for NACA, erstwhile NASA [108]. To our knowledge, this is one of the first experimental studies on the Magnus rotor. Ried observed the appearance of the hysteresis loop for smaller spin ratio and obtained lift coefficient $C_L = 9.5$.

In 1979, L. Bergeson and Greenwald founded the company Wind Ship exploring the wind propulsion for ships [81]. In 1985, Wind Ship published their report on the usage of Magnus based rotor for ships, which was an extension of their work on wind propulsion done in 1974 [109]. Wind Ship tested a 27.432 m^2 Magnus rotor at the sea. The report discusses the ship's performance, mathematical, economic and aeroelastic models. Figure 3.3 presents their

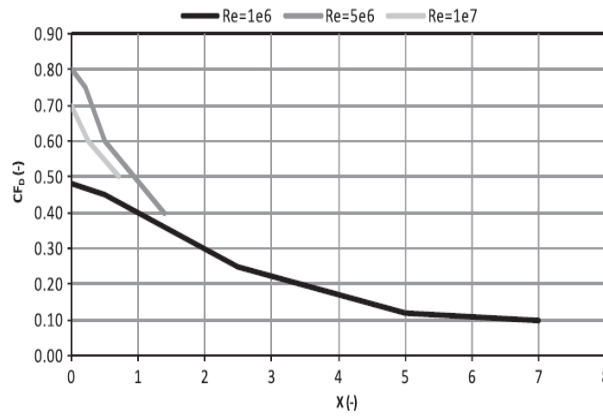


Fig. 12. Drag coefficient vs. spin ratio with Re number as parameter.

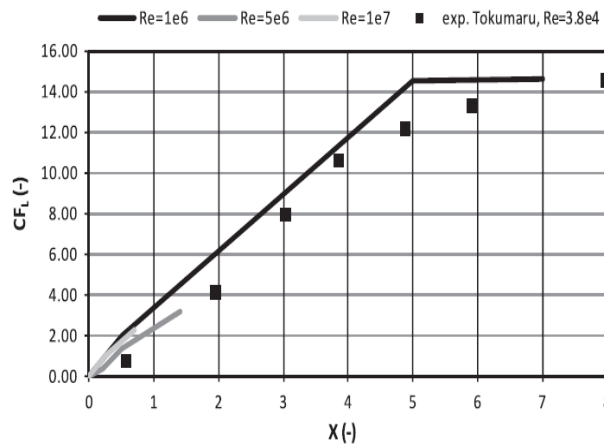


Figure 3.14: Lift, Drag and Moment Coefficient, C_L , C_D and C_m , [51].

results about the lifting capabilities (C_L) of Magnus cylinder in comparison to that of other such devices. In 2010, C. Badalamenti for his doctoral thesis conducted experiments on the feasibility of Magnus-based micro air vehicles (MAV) as shown in figure 3.12, [110], [92]. He considered a cylinder of 0.15 m in length to explore the lifting capabilities of the rotating cylinder. He conducted wind tunnel tests for Reynolds number, $1.6 \times 10^4 \leq Re \leq 9.5 \times 10^4$, and for spin ratio, $X \leq 4$. His test results were in line with the previously available data and concluded the effectiveness of the Magnus rotors in aeronautics.

In 1986, a California based Borg-Luther Group conducted a literature review for US Navy applications, [111]. Their report presented the known experimental data for Magnus effect devices from 1850 to 1985. The first volume presented a detailed analysis of the experimental data on coefficient of lift, drag and moment, C_L, C_D , and C_m , for different spin ratios. It can be considered as a handbook for Magnus cylinders. Table 3.1 presents the list of data considered in the Borg-Luther report. Figure 3.16 and 3.15 present one of the C_L and C_D curves from Borg-Luther report.

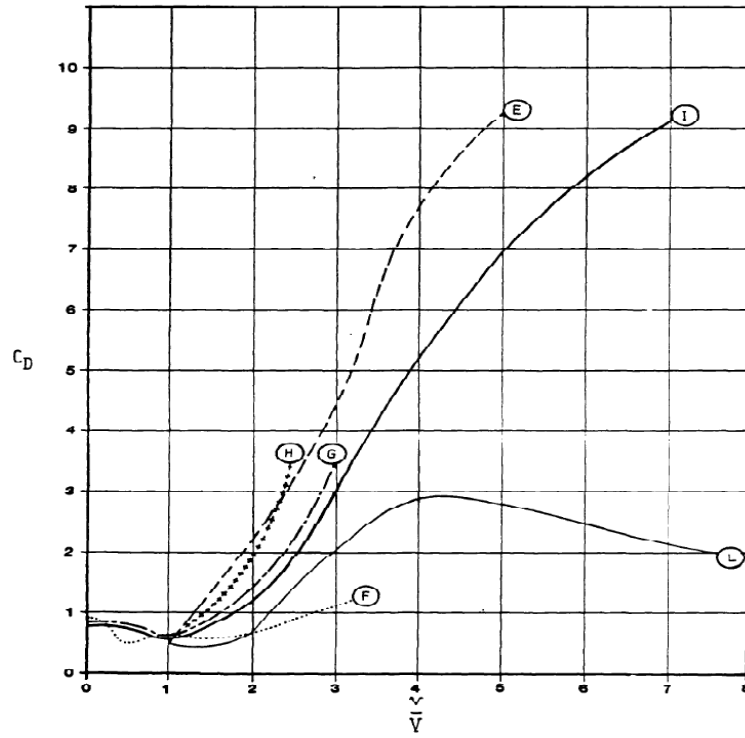


Figure 3.15: C_D curves presented in Borg-Luther report [111].

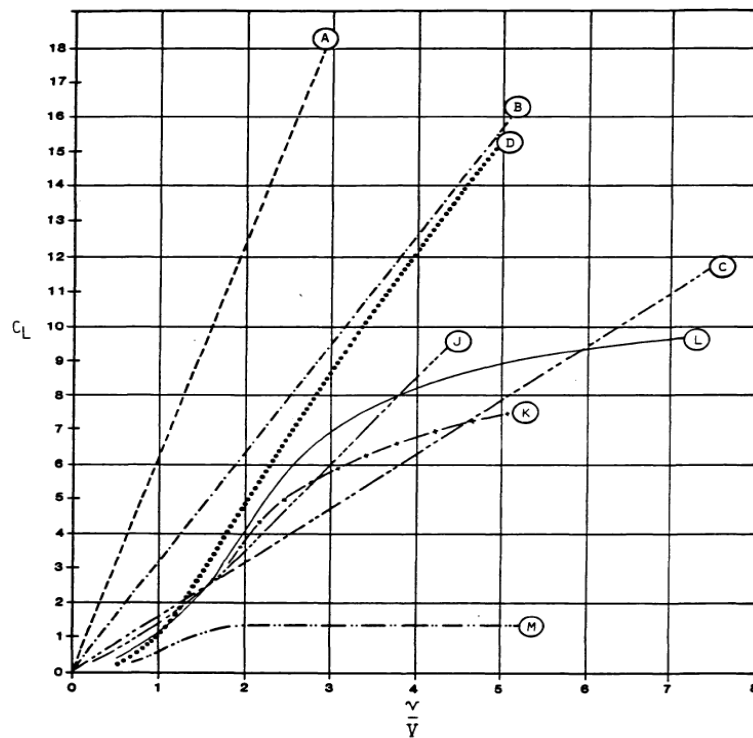


Figure 3.16: C_L curves presented in Borg-Luther report [111].

Curve	Sheet	Investigator No.	Ref. No.	Aspect Ratio	$\frac{de}{d^*}$	Reynolds Number	Remark
A	1,2	ideal fluid, $C_L = 2\pi v/V$		∞	-	∞	inviscid theory
B	1,2	50%A, $C_L =$ $2\pi v/V$		∞	-	∞	referrence curve
C	1,2	25%A, $C_L =$ $2\pi v/V$	-	∞	-	∞	referrence curve
D	1	Thom	26	12.5,26	3	$5.3 - 8.8 \times 10^3$	approaches curve B
E	2,3	Windship	16	6.2	1.58	4.5×10^5	full size curve B
F	2,3	Reid	31	13.3	None	$3.3 - 11.6 \times 10^4$	C_L equiv. to short cylinder with plates
G	2,3	Gottengen	32	4.7	1.7	5.2×10^4	Flettner sails
H	2,3	Gottengen	32	4.7	None	5.2×10^4	Flettner sails w/o plates
I	2,3	Borg	appendix B	4.0	2	11.15×10^4	tested in fresh water
J	1	Thom	26	5.7	None	$3 - 9 \times 10^4$	rough surface (sanded)
K	1	Thom	26	5.7	None	$3 - 9 \times 10^4$	smooth surface
L	1,3	Swanson	24	∞	None	$3.5 \times 10^4 - 3 \times 10^5$	
M	1	Swanson	24	2	None	5×10^5	continous end sections

Table 3.1: List of Past researches considered in Borg-Luther report [111]. Here $\frac{de}{d^*}$ refers to the ratio of the diameter of Thom disc to the Magnus cylinder, and sheet no. refers to the curves presented on pages of the report.

Thom Discs: The lift coefficient of the Magnus cylinder can be increased further by adding Thom discs to the cylinder [112]. In 1934, Alexander Thom published his works on the effects of discs on rotating cylinders. Through his experiments, he concluded that by the addition of discs along the length of the cylinder leads to the production of very high lift coefficient, C_L . In his experiments, he achieved C_L as high as 18. His work was based on the Prandtl's theory of circulation [102], which postulated that the eddies produced on the underside of rotating cylinder should be carried downstream for a general circulation through the flow field. But due to the presence of annular space around the cylinder, the eddies produced on the underside of the cylinder cannot be extracted as shown in figure 3.17a.

Thom came up with the idea that if the flow region on the underside could be minimized it would lead to an automatic reduction in drag and increase in lift. He found that the addition of discs along the cylinder leads to a very low enclosed region on the underside of the cylinder as shown in figure 3.17b. Hence, leading to a very high lift. His work led to numerous application of discs on rotating cylinders. The disc added to rotating cylinders are now called as 'Thom Discs'. Carrying forward his work, Betz presented his results on the rotating cylinders with Thom discs [113].

Thus, by the addition of Thom discs, a Magnus-based AWE system will be able to fly at much slower speeds as well as be less sensitive to the drag. Therefore, allowing the AWE

system to produce power even at lower wind speeds. However, the practical feasibility of this idea is needed to be validated experimentally.

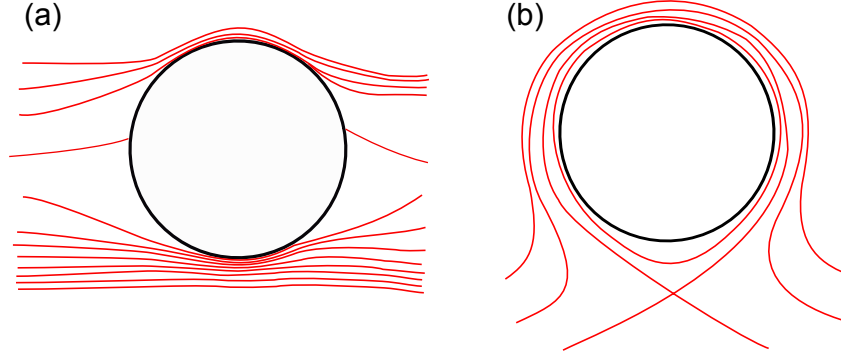


Figure 3.17: Flow past cylinder without Thom disc (a) and with Thom disc (b).

3.4 Aerodynamic Model

In [50], Milutinovic proposed an aerodynamic model for Magnus cylinders:

$$C_D = -0.0211X^3 + 0.1873X^2 + 0.1183X + 0.5 \quad (3.5)$$

$$C_L = 0.0126X^4 - 0.2004X^3 + 0.7482X^2 + 1.3447X \quad (3.6)$$

His aerodynamic model was in turn based on the work of Dr. T K Sengupta, published in Frank M. White book [114]. However, to the best of our knowledge, the proposed model is just an assumption. Hence, to study the Magnus-based AWE systems and to evaluate their power production capabilities, it is necessary to know the aerodynamic model for Magnus cylinder. As discussed in section 3.3, the study of the behaviour of cylinder in high Reynolds regime is a challenging problem. And as the extensive wind tunnel testing or CFD analysis of the aerodynamic properties of Magnus cylinder is not the focus of this work. Hence, to establish a good approximation of the aerodynamic model, a two-step approach is adopted in this thesis work.

The chief aims of this two-step approach are:

- To establish a general trend for C_L and C_D for Magnus cylinder by comparing the most prominent experimental results.
- To establish a minimum and maximum possible value for C_L and C_D for a particular spin ratio.
- To analyze if the polynomial model proposed by Milutinovic in [50] fits the general trend or not? If yes, then can it be assumed as a good approximation for the aerodynamic behavior of Magnus cylinder.

- To check if the proposed polynomial model is in line with the results obtained from the experiments conducted at GIPSA-lab.
- To propose an improved aerodynamic model, if necessary.

In the first step, **Comparison of Experimental Aerodynamic Data**, presented in detail in section 3.4.1, to establish a general trend for C_L and C_D , an analysis of the experimental data of some selected research papers on rotating cylinders in high Reynolds number regime is done. They are then compared with the polynomial aerodynamic model proposed by Milutinovic in [50].

In the second step, **Estimation of Aerodynamic Coefficients**, presented in detail in section 3.4.2, an estimation strategy based on Kalman filter is adapted to estimate the C_L and C_D trends from the data obtained from the experiments conducted with a small-scale Magnus cylinder. The experiments were conducted using an in-house wind tunnel built at GIPSA-Lab. The estimation results are then compared with the aerodynamic model proposed by Milutinovic in [50], to evaluate the validity of the proposed aerodynamic model and understand the aerodynamic behavior of the Magnus cylinder. Section 4.5, discusses in detail the experimental setup and results obtained.

It is necessary to note that the results obtained and discussed in section 3.5 are helpful in establishing a range of possible values for C_L and C_D for each spin ratio. They also help in establishing a general trend for C_L and C_D which is then used for simulation of Magnus-based AWE system. However, to develop an accurate understanding of the power production capabilities of Magnus-based AWE system, the aerodynamic model must be validated by extensive experimentation with full-scale prototypes.

3.4.1 Comparison of Experimental Aerodynamic Data

Reference	Re	AR	Data Type	Comments
[113]	5.2×10^4	4.7	Experimental	Without Thom disc
[111]	1.115×10^5	4	Experimental	Without Thom disc
[109]	4.5×10^5	•	Experimental	With Thom discs
[108]	5×10^4	13.3	Experimental	Without Thom discs
[50]	3.8×10^4	-	Identified.	From [115]
[92]	9.5×10^4	5.1	Experimental	With endplates

Table 3.2: Different references used in the study of C_L and C_D . Aspect ratio (AR) and Reynolds number (Re) are given.

Table 3.2, presents a list of aerodynamic data considered for the first step. The data chosen is experimental data for a range of high Reynolds number. Also, as explained previously in section 3.3, the performance of C_L and C_D can be significantly improved by incorporating Thom discs and end plates into the cylinder design. Thus, to demonstrate what could be the maximum potential of Magnus cylinder, the experimental data for Magnus cylinder with

Thom discs and end-plates is also considered. However, the Magnus-based AWE prototype considered in this thesis does not include Thom discs or endplates. Figures 3.18 and 3.19,

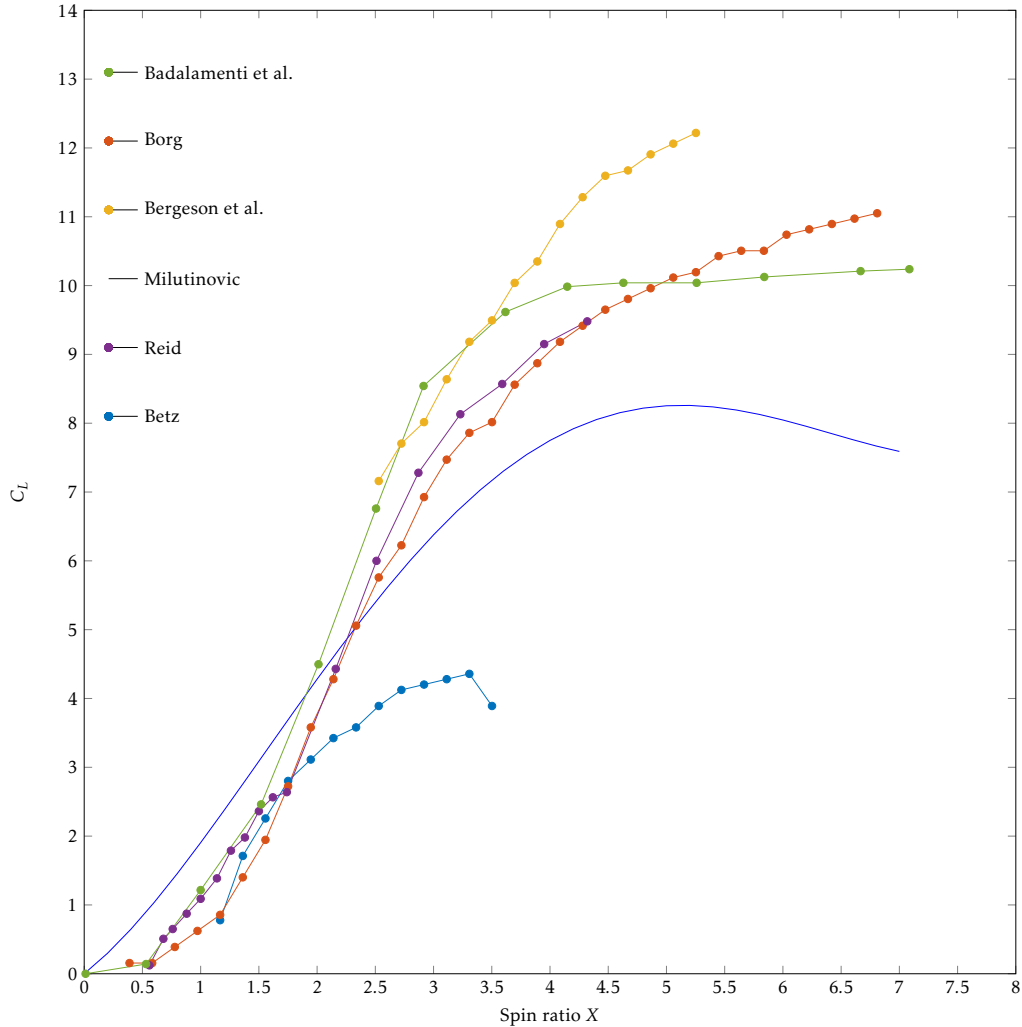


Figure 3.18: The lift coefficient C_L as a function of X . Data is taken from Milutinovic ([50]), Reid ([108]), Borg-luther ([111]), Bergeson ([109]), Betz ([113]), Badalamenti ([92]) for different Reynolds number as detailed in table 3.2.

and table 3.2, presents a selection of aerodynamic data of C_L and C_D for high Re number range. The data is considered from the following studies, [50], [108], [111], [109], [113], [92]. The general trend for C_L can be assumed to be increasing linearly with spin ratio until the maximum value is reached. Depending upon the aspect ratio of the cylinder, and the presence of Thom discs or not, $C_{L,max}$ can be between 8 to 13.

Unlike the C_L curves, C_D curves are more scattered which can be attributed to a higher sensitivity to parameters like the presence of Thom discs and aspect ratio. Also, as it is known that the addition of Thom discs significantly affects C_L and C_D . This is the reason it

can be seen why C_D is much higher for the cylinders with Thom discs or end plates. Surface roughness is another factor which directly influences the C_D of the Magnus cylinder. However, very little information is available about this. Hence, it is assumed that the surface roughness has no or almost negligible impact in these experiments.

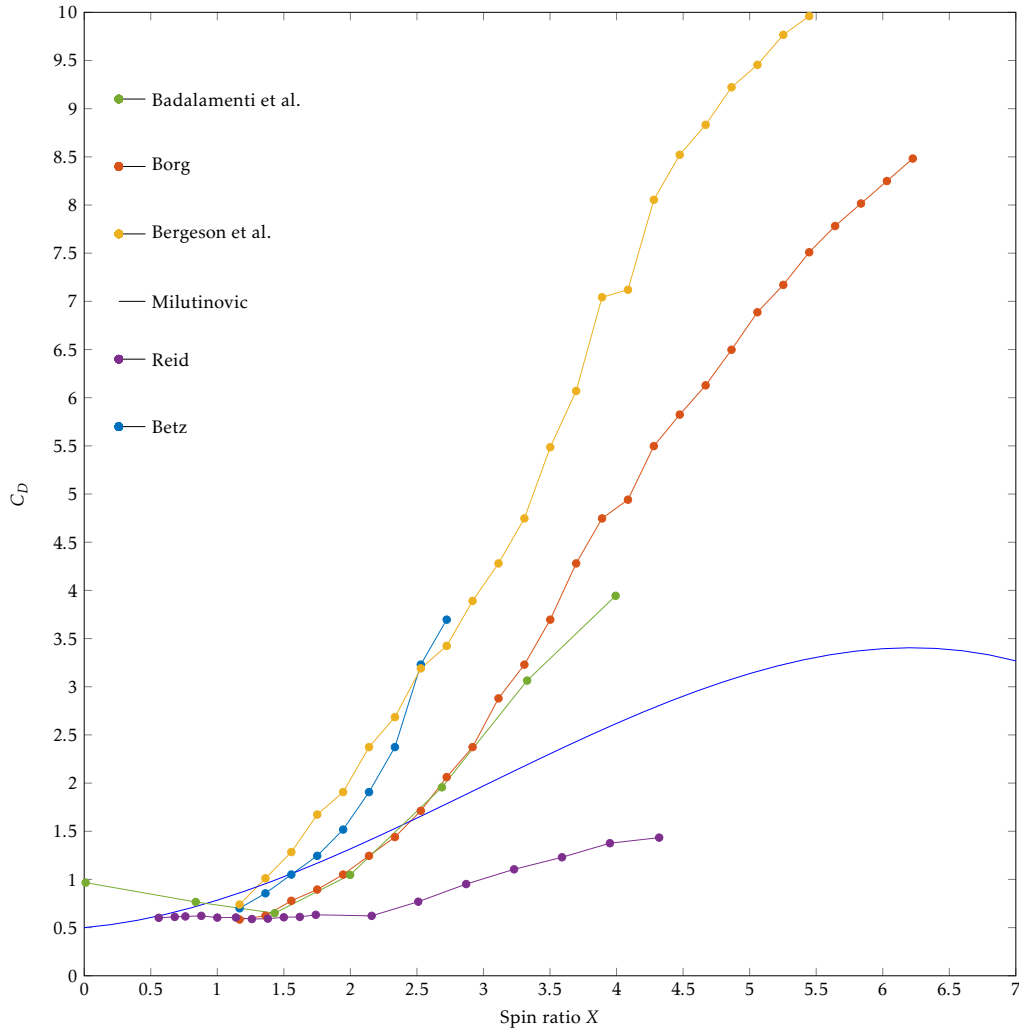


Figure 3.19: The drag coefficient C_D as a function of X . Data is taken from Milutinovic ([50]), Reid ([108]), Borg-luther ([111]), Bergeson ([109]), Betz ([113]), Badalamenti ([92]) for different Reynolds number as detailed in table 3.2.

Based on this analysis, it can be concluded that the polynomial aerodynamic model presented by equations 3.6 is somewhat in line with the other presented experimental data. Hence, the behavior presented by the C_L polynomial curve can be assumed to somewhat represent that of the real cylinder. However, the C_D polynomial curve does not exactly follow the increasing trend but due to lack of reliable data, the curve can be assumed to be an optimistic approximation of the real behavior. Thereupon, the polynomial model can be considered as a model representing C_L and C_D values for the considered Re number range. Nevertheless, this

aerodynamic model needs to be improved further in the future.

3.4.2 Estimation of Aerodynamic Coefficients using EKF

The second step of the approach as mentioned in section 3.3 adopts an estimation strategy to identify the aerodynamic coefficients, C_L , and C_D , from the data obtained from the experiments conducted at the in-house experimental setup built at Gipsa-Lab.

The approach is based on a filtering strategy for a kite based AWE systems. It was first proposed in [116] which in turn is based on an Extended Kalman Filter (EKF) presented in [117]. As a major difference from the works presented in literature, this approach utilizes the perfect measurement strategy described in [118] for the enforcement of an orthogonality constraint between the lift force and the apparent wind vectors. By jointly estimating the wind conditions at the flight level, and the aerodynamic forces of lift and drag, it is then able to compute variables such as the equivalent aerodynamic efficiency of the system, as demonstrated in both simulation and field experiments with a small-scale prototype.

One advantage of this method is that the identification of the aerodynamic model can be done in flight with the same set of sensors already used to monitor and control the system. Thus, eliminating the need for other high-end wind and force measuring devices. Besides this, an approach based on the EKF also allows for real-time estimation of the aerodynamic properties of the system using off-the-shelf embedded hardware and paves the way for the utilization of more sophisticated control mechanisms which rely on these data. Thus, a discrete time EKF is proposed and implemented. The EKF is used to estimate the various forces acting on the system as well as other important variables. The forces are presented in detail in chapter 4 and section 4.2.3.

Hence, the state vector \mathbf{x} of the EKF is given by:

$$\mathbf{x} = [\mathbf{r}^T, \dot{\mathbf{r}}^T, \ddot{\mathbf{r}}^T, \mathbf{v}_w^T, \mathbf{F}_L^T, F_D, F_r]^T, \quad (3.7)$$

Where, \mathbf{r} represents the position, $\dot{\mathbf{r}}$ is the velocity of the ABM, and $\ddot{\mathbf{r}}$ is the acceleration of the equivalent point-mass model of the ABM. The EKF structure also includes the nominal wind \mathbf{v}_w , the lift force \mathbf{F}_L , the equivalent drag force \mathbf{F}_D and the traction force \mathbf{F}_r developed in the tether. The evolution of these states in time is carried out by a simplified dynamical model presented in [119], and are described in discrete time by the following set of difference equations:

$$\begin{aligned} \mathbf{r}_{k+1} &= \mathbf{r}_k + \dot{\mathbf{r}}_k T_s \\ \dot{\mathbf{r}}_{k+1} &= \dot{\mathbf{r}}_k + \ddot{\mathbf{r}}_k T_s \\ \ddot{\mathbf{r}}_{k+1} &= (1/m_{eq})(\mathbf{F}_{Lk} + \mathbf{F}_{Dk} + \mathbf{F}_{gk} + \mathbf{F}_{buk} + \mathbf{F}_{rk}) \\ \mathbf{V}_{wk+1} &= \mathbf{V}_{wk} \\ \mathbf{F}_{Lk+1} &= \mathbf{F}_{Lk} \\ F_{Dk+1} &= F_{Dk} \\ F_{rk+1} &= F_{rk} \end{aligned} \quad (3.8)$$

Where, \mathbf{F}_g is the weight of the equivalent point-mass structure including the Magnus cylinder and the frame on which it is mounted, and T_s is the sampling period. The observation vector of EKF is given by:

$$\mathbf{y} = [\mathbf{r}^T, \dot{\mathbf{r}}^T, v_w, \theta_T, F_r, \delta]^T, \quad (3.9)$$

Where, θ_T is the elevation angle of the tether. The observation variable δ , represents the inner product between the lift vector and the apparent wind \mathbf{v}_a , i.e. $\delta = \mathbf{F}_L^T \mathbf{v}_a$, and is included in the filtering to enforce the orthogonality constraint between these two vectors according to the perfect measurement technique. The inclusion of such a constraint in the form of a measurement is a novel practice in AWE, being first reported in [116].

Regarding the other observed variables, it is assumed that measurements of both the position and velocity vectors of the ABM, \mathbf{r} and $\dot{\mathbf{r}}$ respectively, are available. Moreover, the magnitude of the tether traction F_r , as well as the nominal wind speed v_w and direction θ_T are assumed to be measurable quantities. This choice of observations takes into account the characteristics of a small-scale prototype built at Gipsa-lab, as discussed in detail in section 3.5.

All derivatives required for propagating the state and the covariance matrices in the EKF algorithm are numerically computed using forward finite difference method. Therefore, analytic expressions for the jacobians of the dynamic equations and of the observation functions are not necessary.

3.5 Gipsa-lab Experimental Setup

A small-scale experimental setup previously built at GIPSA-Lab was used to validate the proposed estimation approach. The set up has been used in the previous works [120],[121],[122],[123]. This setup consists of a custom wind tunnel, a Magnus cylinder, and a ground station equipped with instruments for the measurement of different flight parameters.

3.5.1 Wind tunnel

The wind tunnel was built to conduct indoor experiments irrespective of the weather conditions. It consists of nine 800 W brushless motors evenly distributed over a 1.2 m² surface, and capable of generating an air flow up to 9 m/s. The airspeed was sensed by a hot wire anemometer at a rate of 1 Hz through a serial interface, and the controllers are deployed on top of the xPC real-time toolbox for Matlab.

3.5.2 Ground station

The ground station consists of a Maxon 2260L DC 100W dynamo-motor system driven by an ADS 50/10 4 quadrants amplifier manufactured by the same company. The length and

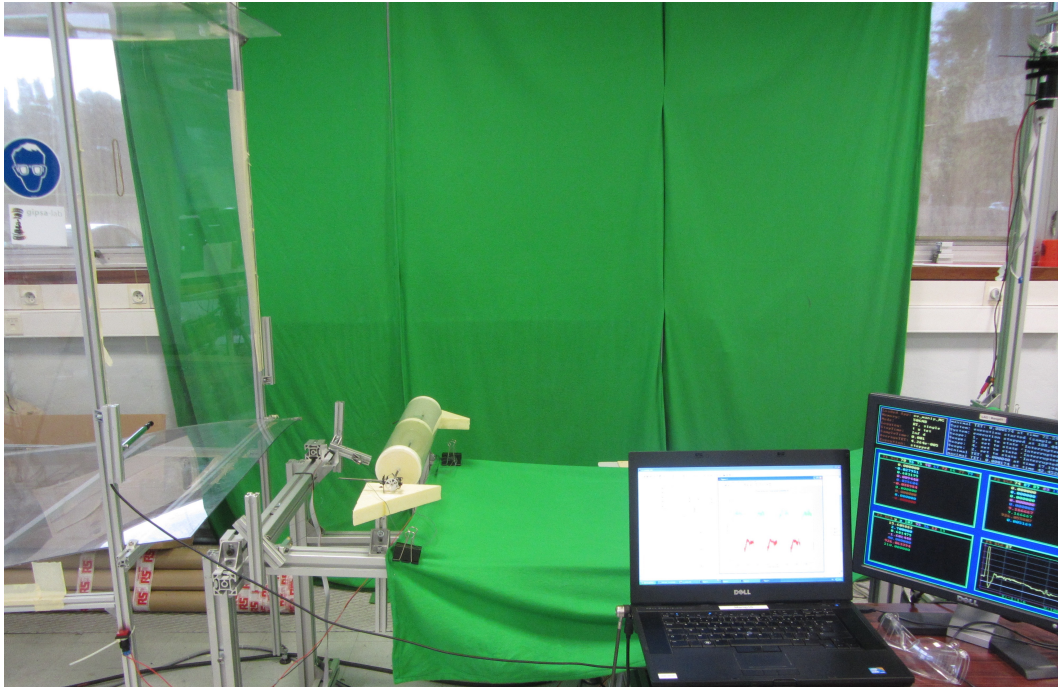


Figure 3.20: The Matlab/Simulink real-time setup used in the experiments.

elevation of the tether are measured by two incremental encoders mounted on the ground station. Tether tension is acquired using a rotative torque sensor, and the PCI DAS1200 DAC module is employed to communicate and send control references to the actuation drivers.

3.5.3 Magnus cylinder

A light weight Magnus cylinder built with carbon rods, polystyrene, and transparent plastic paper was used as ABM in the experiments. Figure 3.22 shows the Magnus cylinder prototype used to conduct the experiments. A mini DC motor is used to spin the cylinder. It can be seen in figure 3.22. Table 3.3 presents the specification of the custom hardware used for measuring and controlling the angular speed of the cylinder.

3.5.4 Results

A series of experiments were performed in the wind tunnel using the small Magnus cylinder prototype. In these experiments, the Magnus cylinder was exposed to varying wind conditions as shown in figure 3.24. The ABM was made to follow a predefined trajectory with a reel-in and reel-out phases. Figure 3.23 shows the trajectory followed by the ABM. The angular velocity, ω_{cyl} , of the ABM was made to vary continuously. During each cycle several variables

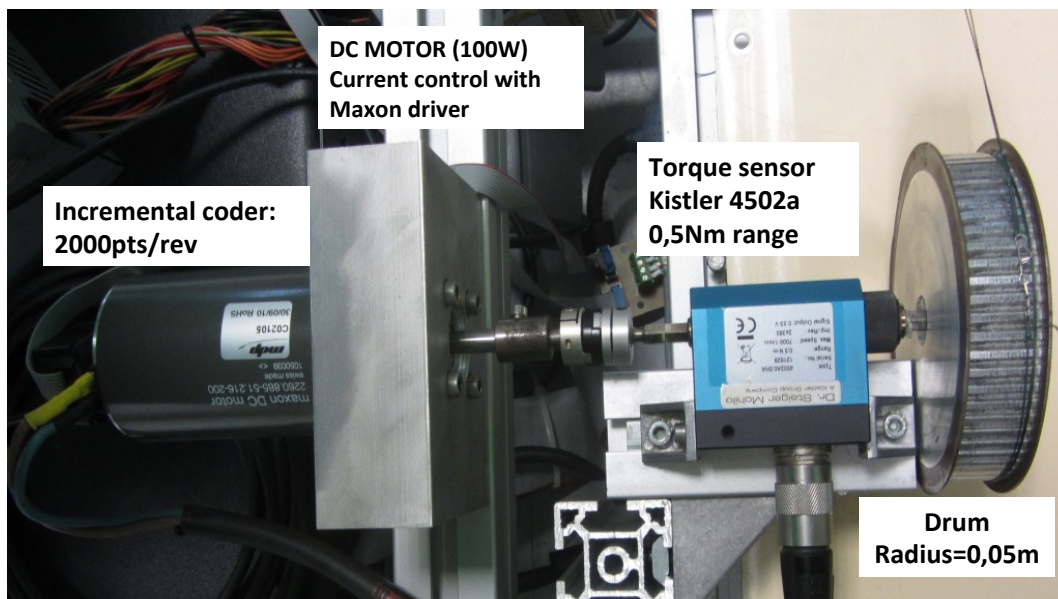


Figure 3.21: The Ground station to which the Magnus cylinder was tethered.

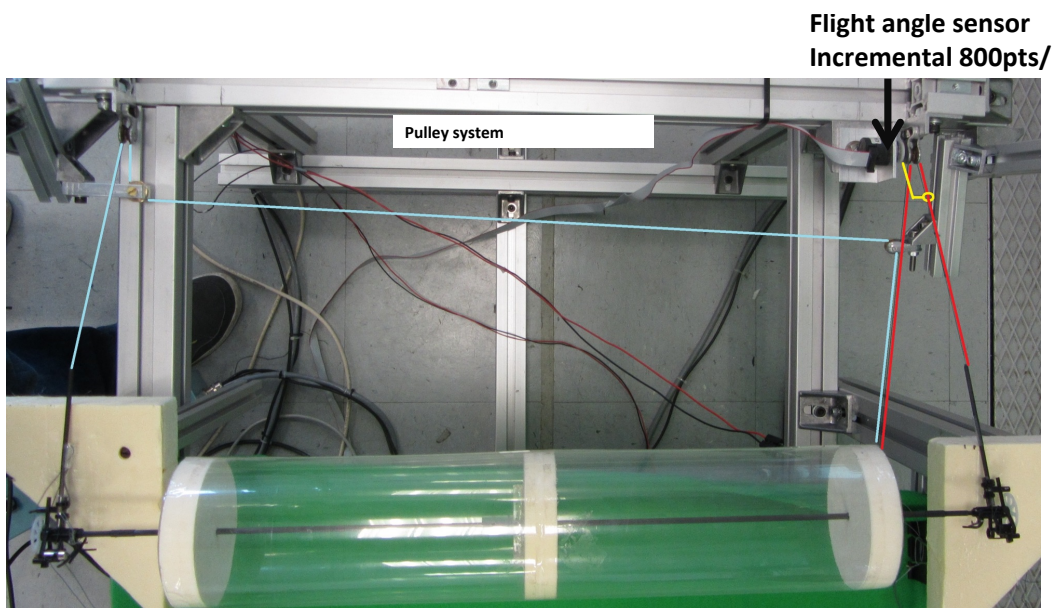
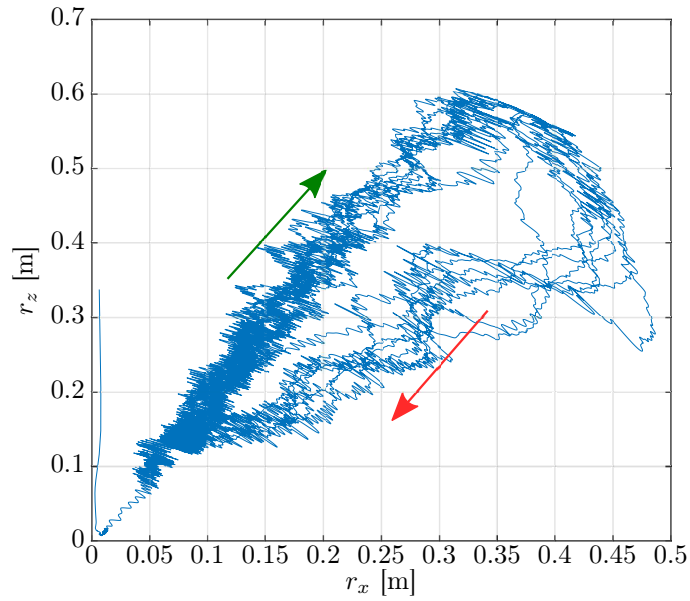


Figure 3.22: The Magnus cylinder used as ABM in the wind tunnel experiments.

were recorded including the tether length r_t , elevation angle of the tether θ_T , and the traction force F_r . The data collected from these experiments were used in the EKF to estimate the lift, F_L , and, F_D , drag forces acting on the ABM. Using equation 3.9 at each time instant the observation vector was computed for a time window of 100 seconds which was then fed into the EKF estimator to estimate the forces and compute the aerodynamic coefficients by using equation 4.1. Figure 3.24, presents the airspeed profile recorded over the course of

Table 3.3: Parameters of the Experiments

Symbol	Description	Value
M_{Mag}	Magnus cylinder's mass	0.11 Kg
MI	Tether's linear mass	0 Kg/m (neglected)
r_{cyl}	Magnus cylinder's radius	0.047 m
l_{cyl}	Magnus cylinder's length	0.45 m
M_{IM}	Rotor's mass	0.0481 Kg
ρ	Air density	1.225 Kg/m ³
Re	Reynolds Number	1.5
v_w	Average Wind Speed	7 m/s

**Figure 3.23:** Flight trajectory of the small-scale Magnus cylinder on the vertical plane

the experiments, as measured at 1 hz by the hot wire anemometer mounted inside the wind tunnel. Figure 3.24 also shows the wind speed estimate as obtained from the filter. It can be observed that the estimated wind speed almost perfectly follows the recorded signal by the hot wire anemometer. However, due to the estimator's dynamics, the estimated wind speed has a non-negligible dynamics in comparison to the recorded data.

The EKF estimator also estimates the spin ratio of the Magnus cylinder from equation

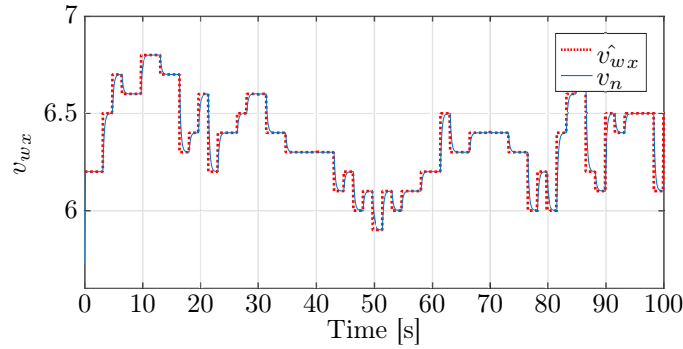


Figure 3.24: Wind speed measurement from the wind tunnel and estimates obtained from the filter.

3.3. Figures 3.26 and 3.27 present the evolution of the estimated coefficient of lift, C_L , and drag, C_D , for several pumping cycles. It can be observed from these curves that C_L and C_D assume values coherent to other results presented in the section 3.3, and in figures 3.18 and 3.19. As the ABM undergoes reel-in and reel-out phases, thus, for each phase, the spin-ratio varies as well, which in turn changes the C_L and C_D . This variation of C_L and C_D can be clearly observed in the figure 3.26 and 3.27. Thus, validating the estimator.

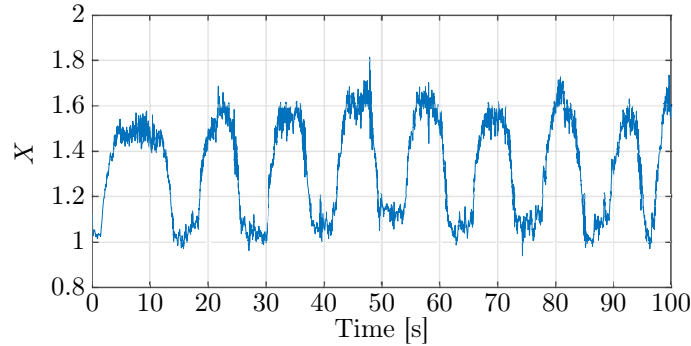


Figure 3.25: Estimated spin ratio of the Magnus cylinder

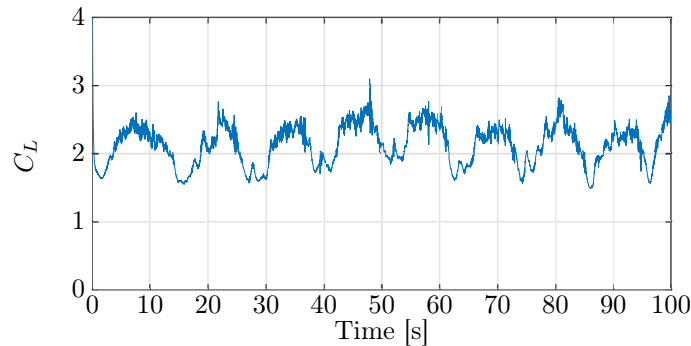


Figure 3.26: Estimated lift coefficient of the system

The second set of tests were conducted to identify specifically the aerodynamic characteristics of the Magnus cylinder. In these experiments, the angular velocity ω_{cyl} was continuously

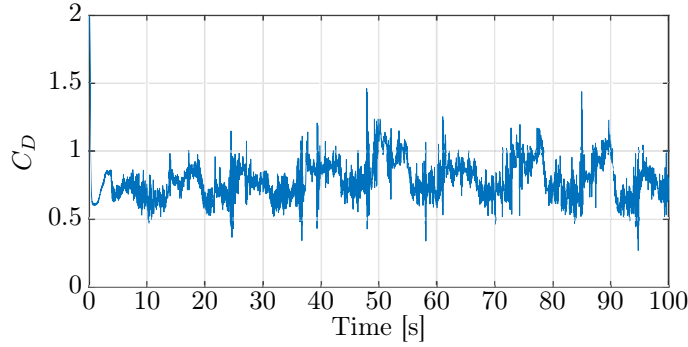


Figure 3.27: Estimated drag coefficient of the system

varied from 150 rad/s to 225 rad/s while the mean wind speed produced by the wind tunnel was varied from 4.5 m/s to 7 m/s resulting in the spin ratio between 1 and 2.5.

To ensure that the dry friction force Γ_s in the pulley system always act in the same direction for all the data sets, the tether length was made to increase slowly during these experiments. In a series of experiments previously conducted at the Gipsa-lab and presented in detail in [123] the dry friction was found to be approximately $\Gamma_s = 0.4$ N. In order to mitigate the influence of this effect and finally remove it from the tether traction measurements, the tether traction measurements were subjected to dry friction compensation. Thus, resulting in

$$\mathbf{F}'_{r_k} = \mathbf{F}_{r_k} + \Gamma_s \quad (3.10)$$

Where, \mathbf{F}'_{r_k} corresponds to the tether traction after the dry friction compensation which was then fed into the EKF.

Figure 3.28 presents the three sets of the aerodynamic coefficients C_L and C_D . The first set of data corresponds to the the pumping cycle experiments illustrated in figure 3.23. The second set of coefficients corresponds to the identification experiments using the EKF estimator mentioned above in this section. And the third set represents the polynomial aerodynamic model presented in [50] and discussed in section 3.4. And is given by the following equations:

$$\begin{aligned} C_L &= 0.0126X^4 - 0.2004X^3 + 0.7482X^2 + 1.3447X \\ C_D &= -0.0211X^3 + 0.1873X^2 + 0.1183X + 0.5 \end{aligned} \quad (3.11)$$

They are compared for the same range of spin ratios. It can be observed from the figure 3.28 that except for an offset of 0.4, the C_L values estimated during the identification experiments follow the same trend as predicted by the polynomial model for the considered range of the spin ratio.

However, in the case of C_D , it can be observed that the C_D estimated by EKF shows a different behavior. For spin ratios up to 1.5, the estimated C_D somewhat follows the polynomial model. But for spin ratios larger than 1.5 it does not follow the polynomial model

and can be observed to increase with the increase in spin ratio. Thus, suggesting that the cause leading to increase in C_D depends on the spin ratio. This deviation can also depend on the effect of tether drag, frame (on which the cylinder is mounted), and spinning mechanism. As the sideslip, β increases alongwith the tether length, the drag due to the tether and the structure also increases, leading to a change in C_D for higher spin ratios. But this is just a supposition and this must be confirmed by more experimental studies. Also, the polynomial

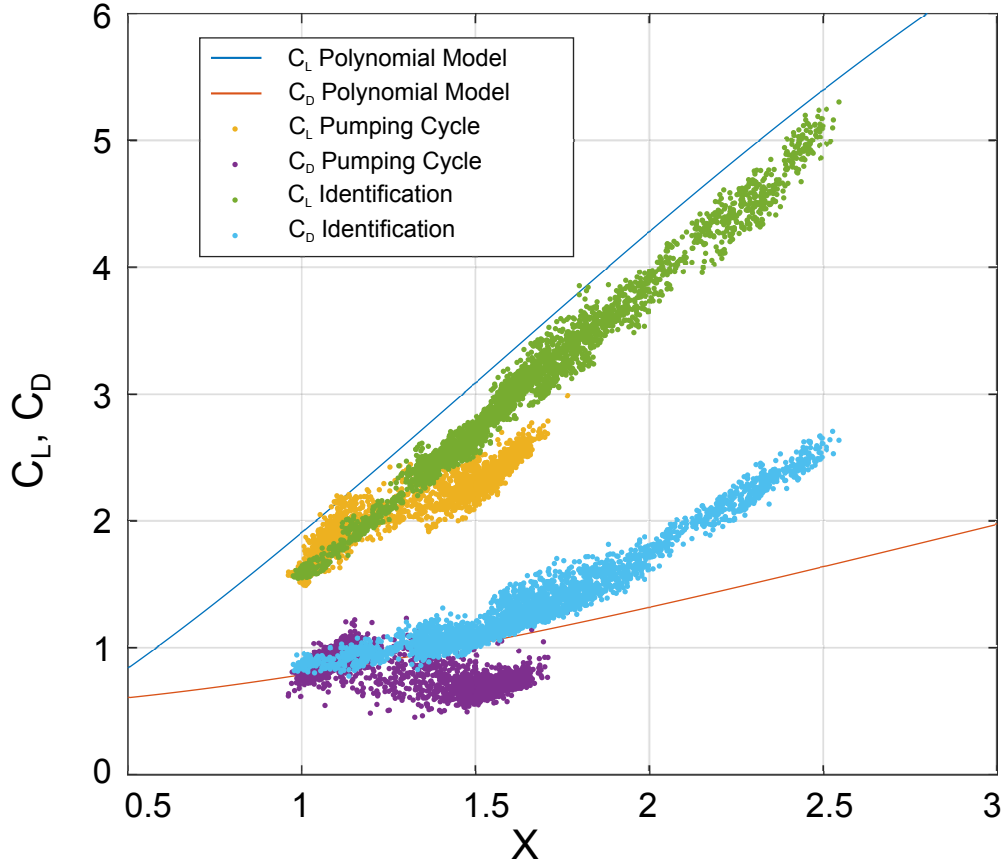


Figure 3.28: Comparison of the lift and equivalent drag coefficients estimated during the pumping cycles and identification experiments for $v_w = 7m/s$ and $Re = [12.5]$ with the values predicted by the polynomial model proposed in [50].

aerodynamic model presented by equation 3.11, assumes a theoretically endless cylinder with a single tether attached to its center of gravity. Thus, it neglects the effect of the spinning mechanism and edge effects which come into effect due to the finite length of the cylinder, and which may have a considerable effect on the overall C_D . These results indicate that in order to properly account for the influence of these effects on the overall drag of the system another model must be considered which takes into account all these effects.

Regarding the C_L and C_D values estimated during the pumping cycle experiments shown in figure 3.23, it can be observed that they present a slightly different behavior. These dis-

crepancies can be attributed to the dry friction present in the system but not accounted for. In the production phase when the tether is being reeled out and the spin ratio is kept at around $X = 1.5$, the dry friction leads to an underestimation of C_L and C_D since it causes a decrease in the value of measured tether traction as it can be understood by equation 3.10. On the other hand, during the retraction phase when the tether is being reeled-in, and the spin ratio oscillates around $X = 1.1$, the dry friction is responsible for causing an increase in the tether traction as measured by the sensor. Hence, leading to an overestimation of the aerodynamic coefficients. This can be clearly observed in figure 3.28. Moreover, the fact that the overestimation for low spin ratios is less than the underestimation for high spin ratios suggests that dry friction in the system depends on the traction force itself.

3.6 Conclusion

The two-step approach presented in this chapter has provided an important insight into the behavior of the aerodynamic coefficients of Magnus cylinder. In the first step, an overview of the experiments conducted in the past provides an interesting insight into the capabilities of the Magnus effect. The experimental results provide a reference point for this study and give credence to the polynomial aerodynamic considered in this study.

The second step of the approach presents an estimating method. The estimated C_L and C_D further widen the understanding of the aerodynamic behavior of Magnus cylinders. The findings support the initial understanding of the aerodynamic properties. Based upon these results it can be stated that an improved aerodynamic model is needed, especially for the drag coefficient for an accurate analysis of Magnus effect-based AWE systems.

Modelling of Magnus-Based AWE Systems

Contents

4.1	Introduction	57
4.2	System Model	58
4.2.1	2-D Mathematical Model	58
4.2.2	3-D Model of Magnus-based AWE system	61
4.2.3	Equation of Motion	63
4.3	Moments acting on Magnus-based AWE System	68
4.3.1	Aerodynamic Moments	70
4.3.2	Gyroscopic couple	76
4.3.3	Reactive Torque	77
4.4	Control Strategy	77
4.4.1	Global Control Scheme	77
4.4.2	Guidance strategy	79
4.5	Simulation Results	82
4.5.1	Performance under Static Assumption	82
4.5.2	Simulation Parameters	83
4.5.3	Simulation Results	84
4.6	Conclusion	88

4.1 Introduction

Modeling and simulation serves an important step in the analysis of any technical system. Mathematical models are widely used to describe and analyze the behavior of any system before conducting experiments. As the airborne wind energy prototypes involve the study of many multi-disciplinary subjects and their on-field testing involve high costs, development of high fidelity mathematical models becomes an important aspect in the study of such systems. In addition, to develop higher level control algorithms and estimate the power production

capabilities of AWE systems, mathematical analysis is a necessary step in the research on AWE systems.

This chapter discusses in detail the modeling of a Magnus-based AWE system. To the best of our knowledge, there are few articles or thesis work in the literature presenting a detailed model of Magnus-based AWE systems. Hence, this chapter is one of the first in literature. It is our contribution to the ongoing research on Magnus-based AWE system.

In this chapter, section 4.2 discusses in detail the Magnus-based AWE prototype considered in this thesis work. It also discusses a 3-D six degree of freedom model for the Magnus-based AWE system. In addition, this model is used to implement feedback controllers that aim to obtain figure-eight and circular crosswind flying paths such as the one proposed by [34]. This result (to the best of our knowledge) is the first contribution in the scientific literature on the control of Magnus effect-based AWE system in crosswind trajectories. In section 4.3, the mathematical model presented in the section 4.2 is further extended to include the torques acting on the Magnus cylinder. It discusses in detail the different types of torques that come into being and presents a modeling approach. In section 4.4, a guidance and control strategy is presented along with a guidance algorithm to perform eight figure and circular orbits in the sky. Section 4.5 discusses the simulation parameters and results of 3-D dynamic simulation for an MW-sized Magnus-based AWE system. The obtained results are finally compared with that of the simplified model under the static assumption. The chapter ends with section 4.6 presenting some conclusions, and discussing some inferences and perspectives.

4.2 System Model

There are several approaches in the literature which are used to model the airborne platform as discussed in chapter 2 section 2.2.1. Spherical coordinate system is a common approach used to describe the position and motion of the kite or UAVs as presented in in chapter 2 section 2.2.1. However, in order to analyze the attitude and model the different forces and moments, it is necessary to use two different frame of references as discussed in the subsequent sections.

In this section, two different modeling approaches are presented. The 2-D model is used to analyze the Magnus-based AWE system to understand the general behavior of such systems and is used to evaluate the general performance of such systems. The 3-D model presents a detailed analysis of the system forces and moments which are necessary to develop high fidelity simulations for Magnus-based AWE systems.

4.2.1 2-D Mathematical Model

The current literature on ABM chiefly, discusses 2-D model [50], [52], to describe the ABM dynamics. Figure 2.18 shows the prototype design under consideration for the development of the 2-D and 3-D model of the Magnus-based AWE system. The 2-D model presented here

is adapted from [52]. The dynamics of Magnus cylinder is described by using two frame of references, namely the inertial frame, (x_i, y_i, z_i) centered at the ground station O and the body frame, (x_b, y_b, z_b) , centered at the C_g of the Magnus cylinder, detailed in section 4.2.2. In the 2D model presented in this section the dynamics of the Magnus cylinder is restricted to the vertical plane and the rudder dynamics is not considered. Figure 4.1 presents different forces acting on the Magnus cylinder. The aerodynamic lift, \mathbf{F}_L , and drag force, \mathbf{F}_D , are produced

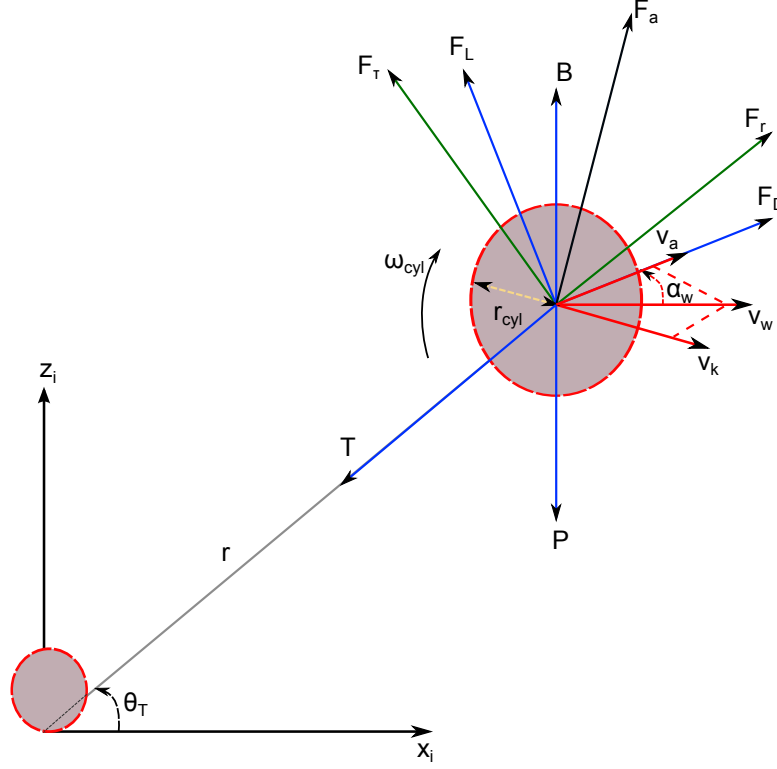


Figure 4.1: Forces acting on the Magnus Cylinder.

by the magnus effect and are given by:

$$F_L = \frac{1}{2}\rho S_{cyl}v_a^2 C_L, \quad F_D = \frac{1}{2}\rho S_{cyl}v_a^2 C_D \quad (4.1)$$

Where, ρ is the air density, S_{cyl} is the Magnus cylinder's projected surface area, v_a is the norm of the apparent wind velocity vector (equation 4.10), C_L and C_D are the respective coefficients of lift and drag as discussed in chapter 3 section 3.4. The resultant aerodynamic force, F_a , leads to the tether force, F_r , produced in the tether which in turn is used to drive the generator. The system dynamics can be modeled as :

$$\ddot{\theta}_T = \frac{1}{r_t} \left[-2\dot{\theta}_T \dot{r}_t + \frac{F_T}{M} \right] \quad (4.2)$$

$$\ddot{r}_t = \frac{1}{M_{Mag} + M_{IM}} \left[r_t \dot{\theta}_T^2 M_{Mag} + F_R - T \right] \quad (4.3)$$

$$\dot{T} = \beta_T (u_T - T) \quad (4.4)$$

Where, r_t is the tether length, θ_T is the elevation, M_{Mag} is the mass of the Magnus cylinder, $M_{IM} = \frac{I}{R_d^2}$ (where I is the moment of inertia of the rotor and R_d the radius of the drum), and T is the tether traction. Equation 4.4 models the dynamics of the actuators used in the experimental setup to control the tether force. Where, u_T is the control input and β_T is the frequency representing its dynamic response. In figure 4.1, P represents the weight of the Magnus cylinder, and B is the buoyant force produced by lighter than air gas filled inside the Magnus cylinder. F_R and F_T represents the radial and tangential component of the resultant force acting on the Magnus cylinder.

$$F_R = F_L \sin(\theta_T - \alpha_w) + F_D \cos(\theta_T - \alpha_w) - P \sin \theta_T + B \sin(\theta_T) \quad (4.5)$$

$$F_T = F_L \cos(\theta_T - \alpha_w) - F_D \sin(\theta_T - \alpha_w) - P \cos \theta_T + B \cos(\theta_T) \quad (4.6)$$

Where, α_w is the wind velocity angle defined in equation (4.10).

The mass of the Magnus cylinder is sum of the mass of cylinder, mass of the structure on which it is mounted, tether and the mass of the gas filled inside it.

$$M_{Mag} = M + V_o \rho_{gas} + M_{tether} \quad (4.7)$$

with M being the combined mass of the cylinder and the structure, M_{tether} is the mass of the tether, V_o is the volume of the Magnus cylinder and ρ_{gas} is the density of lighter than air gas. Using Archmiedes's principle the buoyant force can be calculated as:

$$B = \rho V_o g \quad (4.8)$$

The norm of the apparent wind velocity vector v_a and the angle of this vector with respect to the ground α_w is given by:

$$\alpha_w = \arctan \frac{v_h}{v_v} \quad (4.9)$$

$$v_a = \sqrt{(v_h)^2 + (v_v)^2} \quad (4.10)$$

Where, v_v , represents the vertical velocity, and v_h represents the horizontal relative velocity. Both of which depend on the motion of the Magnus cylinder. And they can be calculated as:

$$v_h = v_w + r\dot{\theta}_T \sin \theta_T - \dot{r} \cos \theta_T \quad (4.11)$$

$$v_v = -(r\dot{\theta}_T \cos \theta_T + \dot{r} \sin \theta_T) \quad (4.12)$$

Where, v_w is the wind velocity with respect to the ground acting in the x_i direction.

As discussed in section 3.3 for Magnus effect the aerodynamic lift, C_L , and drag coefficient, C_D , are functions of the spin ratio X given by:

$$X = \frac{\omega_{cyl} r_{cyl}}{v_a} \quad (4.13)$$

with ω_{cyl} representing Magnus cylinder's angular spin velocity and r_{cyl} its radius.

4.2.2 3-D Model of Magnus-based AWE system

To undertake a detailed analysis and simulate the Magnus-based AWE system, and evaluate the power produced by such systems, it is necessary to have a 3-D model which can be used to analyze all the forces and moments acting on such system. Several approaches derived from flight dynamics have been used to describe the dynamics of AWE systems, particularly kite and UAV based AWE systems. Each using different sets of reference frames to describe the position and dynamics of the airborne platform. One approach as stated in [48] uses a different set of frames of references to describe the dynamics of kite-based AWE system. It uses an earth centered earth fixed (ECEF) frame to describe the wind direction, and a second NED (North-east-down) frame to describe the location of the C_g of the airborne platform w.r.t which its dynamics is described.

In another approach, described in [58], the attitude of the kite and its position are decoupled by developing separate equations of motion for the bridle point and kite. It uses an inertial frame fixed at the ground station, a second frame fixed at the bridle point, and a third body-fixed frame is used to describe the attitude of the kite with respect to bridle point.

Several other similar models using spherical coordinate system and simple equations can be found in [124],[34],[10]. Such approaches are highly useful in describing the dynamics of the kite as the kite systems are a non-rigid structure consisting of a complex bridle system, often with multiple lines used to steer the system.

Figure 4.2 presents an illustration of the Magnus based AWE prototype considered in this thesis work. In this formulation, a Magnus cylinder (ABM) mounted on a rigid frame is considered. The frame is connected to the ground-based generator through a single tether and the force developed in the tether is used to drive the winch located at origin O .

The position of the ABM is described with respect to an inertial frame, represented by unit vectors $(\vec{x}_i, \vec{y}_i, \vec{z}_i)$ fixed at the ground station. Wind \vec{v}_w is described in the inertial frame. The attitude of the ABM is described with respect to body frame represented by unit vectors $(\vec{x}_b, \vec{y}_b, \vec{z}_b)$, centered at the center of gravity C_g of the ABM, which is assumed to coincide with the geometrical center of the Magnus cylinder. The tether orientation θ_T and ϕ_T is described with respect to the inertial frame. The cylinder is free to rotate around its own axis aligned with y_b , actuated by an electric motor with a control law controlling the speed of rotation of the cylinder ω_{cyl} . In figure 4.2, point O represents the location of the ground station at which the inertial frame is centered and the point A represents the bridle point where the tether is attached to the rigid structure on which the Magnus cylinder is mounted, shifted from C_g along z_b axis.

Using the sign conventions from flight dynamics, the body frame is assumed to be in the North-east-down direction (NED), and the attitude of ABM is described using Euler angles, ψ , θ , and ϕ defined with intrinsic ZYX convention as explained in section 4.2.2.1. The dynamics of the bridle point with respect to an inertial frame is neglected. Also, the tether elasticity, inertia, and drag are not considered in this formulation. In particular, as the drag coefficient, C_D , of the Magnus cylinder is several times higher than the C_D of the rigid and soft kites, it

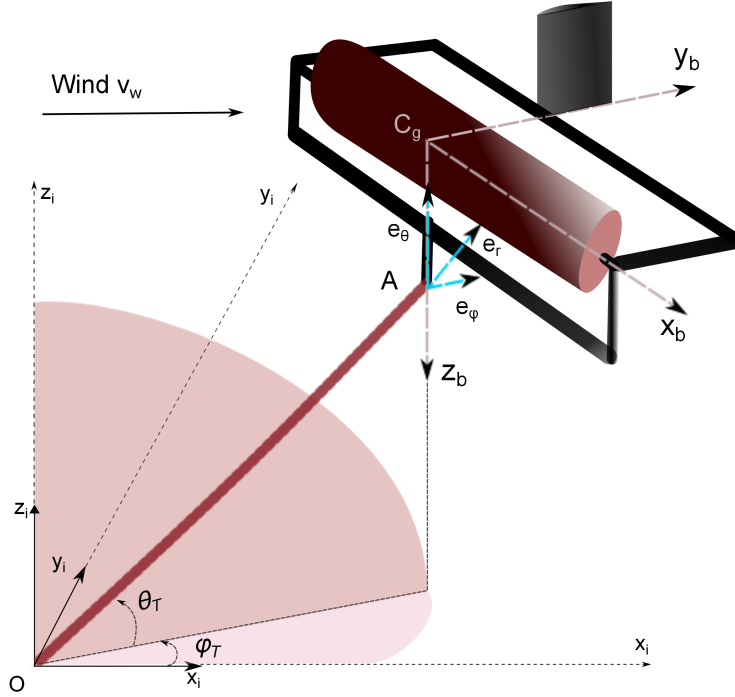


Figure 4.2: Magnus-based AWE systems.

is expected that the impact of tether drag on the whole performance of the system could be smaller than other pumping AWES. Nonetheless, the aerodynamic drag of the tether is known to have a considerable effect on the overall performance and hence, this assumption has to be evaluated for Magnus-based AWE systems.

4.2.2.1 Rotation matrices

The transformation of the inertial frame into the body frame is carried out by using the standard ZYX transformation, R_b which consists of a rotation around \vec{z}_i by ψ , followed by a second rotation around \vec{y}_1 by θ , and finally by ϕ around \vec{x}_2 . In addition to this, another matrix L_{flip} is used to flip the coordinate system to align it with the NED frame.

$$\vec{\Theta} = \psi \vec{z}_i + \theta \vec{y}_1 + \phi \vec{x}_2 \quad (4.14)$$

$$R_b = \begin{bmatrix} c_\theta c_\psi & c_\theta s_\psi & -s_\theta \\ s_\phi s_\theta c_\psi - c_\phi s_\psi & s_\phi s_\theta s_\psi + c_\phi c_\psi & s_\phi c_\theta \\ c_\phi s_\theta c_\psi + s_\phi s_\psi & c_\phi s_\theta s_\psi - s_\phi s_\psi & c_\phi c_\theta \end{bmatrix} \quad (4.15)$$

Where, "s" and "c" denote sine and cosine functions.

$$L_{flip} = \begin{bmatrix} 1 & 0 & 0 \\ 0 & -1 & 0 \\ 0 & 0 & -1 \end{bmatrix} \quad (4.16)$$

Hence,

$$R_b^i = R_b L_{flip} \quad (4.17)$$

Therefore, any set of inertial frame unit vectors $(\vec{x}_i, \vec{y}_i, \vec{z}_i)$ can be converted into body frame unit vectors $(\vec{x}_b, \vec{y}_b, \vec{z}_b)$ by:

$$\begin{bmatrix} \vec{x}_b \\ \vec{y}_b \\ \vec{z}_b \end{bmatrix} = R_b^i \begin{bmatrix} \vec{x}_i \\ \vec{y}_i \\ \vec{z}_i \end{bmatrix} \quad (4.18)$$

As presented in the section 4.4.2, the guidance law for the ABM uses spherical coordinate system which uses a different set of rotational matrices to transform the inertial frame into spherical coordinate system. Thus, any vector in inertial frame can be transformed into spherical coordinate system by using transformational matrix R_s^i which is given by:

$$R_s^i = \begin{bmatrix} -\cos(\phi_T) \sin(\theta_T) & -\sin(\phi_T) & -\cos(\phi_T) \cos(\theta_T) \\ -\sin(\phi_T) \sin(\theta_T) & \cos(\phi_T) & -\sin(\phi_T) \cos(\theta_T) \\ \cos(\theta_T) & 0 & -\sin(\theta_T) \end{bmatrix} \quad (4.19)$$

Where, ϕ_T and θ_T are the azimuthal and elevation angles of the tether and $(\vec{e}_r, \vec{e}_\theta, \vec{e}_\phi)$ are the unit vectors representing the spherical coordinate system as shown in figure 4.2. Therefore, any set of inertial frame unit vectors $(\vec{x}_i, \vec{y}_i, \vec{z}_i)$ can be converted into spherical frame unit vectors $(\vec{e}_{r_i}, \vec{e}_{\phi_T}, \vec{e}_{\theta_T})$ by:

$$\begin{bmatrix} \vec{e}_r \\ \vec{e}_{\phi_T} \\ \vec{e}_{\theta_T} \end{bmatrix} = R_s^i \begin{bmatrix} \vec{x}_i \\ \vec{y}_i \\ \vec{z}_i \end{bmatrix} \quad (4.20)$$

As explained in global control strategy, section 4.4.1, the body frame z_b axis is self-aligned with the tether. The remaining degree of freedom which can be controlled by a rudder is the last rotation around z_b axis, and in a stabilized situation it is aligned with the tether. Thus, to use this variable instead of ZYX a ZYZ transformation can be used. R_{bZYZ}^i , presents the rotation matrix to perform ZYZ transformation and it is described as:

$$R_{bZYZ}^i = \begin{bmatrix} c_\phi c_\psi c_\theta - s_\phi s_\psi & c_\theta c_\phi s_\psi + s_\phi c_\psi & -c_\phi s_\theta \\ -s_\phi c_\psi c_\theta - c_\phi s_\psi & -s_\phi c_\theta s_\psi + c_\phi c_\psi & -s_\phi s_\theta \\ c_\psi s_\theta & s_\theta s_\psi & c_\theta \end{bmatrix} \quad (4.21)$$

4.2.3 Equation of Motion

Assuming the Magnus cylinder as a rigid one, the position of the C_g of the cylinder in inertial frame can be presented by a position vector, \vec{r}_i as:

$$\vec{r}_i = x\vec{x}_i + y\vec{y}_i + z\vec{z}_i \quad (4.22)$$

Where, $\vec{x}_i, \vec{y}_i,$ and \vec{z}_i are unit vectors of their respective axis in the inertial frame. Hence, the position vector, \vec{r}_b , of the ABM in body frame is given by:

$$\vec{r}_b = R_b^i \vec{r}_i \quad (4.23)$$

The translational velocity of the C_g is given by:

$$\dot{\vec{r}}_i = \vec{v}_i \quad (4.24)$$

Applying the axis transformation, the body frame velocity of the ABM is expressed by:

$$\vec{v}_b = R_b^i \vec{v}_i \quad (4.25)$$

Hence, equation of translation of C_g of the Magnus cylinder w.r.t the inertial frame is given by:

$$\dot{\vec{r}}_i = (R_b^i)^{-1} \vec{v}_b \quad (4.26)$$

The attitude of the ABM is described using euler angles ψ , θ , and ϕ defined with intrinsic ZYX convention with Θ defining a non-orthogonal vector of euler angles. As in flight dynamics, the angular rates are measured about their respective axis of rotation, i.e. \vec{z}_i , \vec{y}_1 , and \vec{x}_2 . Where, \vec{y}_1 is obtained after the first rotation around \vec{z}_i , and \vec{x}_2 is obtained after second rotation around \vec{y}_1 axis. Therefore,

$$\dot{\Theta} = \dot{\psi} \vec{z}_i + \dot{\theta} \vec{y}_1 + \dot{\phi} \vec{x}_2 \quad (4.27)$$

Where, $\dot{\Theta}$, euler angle rate vector. Expressing \vec{x}_2 , \vec{z}_i and \vec{y}_1 with respect to body frame unit vectors \vec{x}_b , \vec{z}_b , and \vec{y}_b :

$$\begin{bmatrix} p \\ q \\ r \end{bmatrix} = W_i \begin{bmatrix} \dot{\phi} \\ \dot{\theta} \\ \dot{\psi} \end{bmatrix} \quad (4.28)$$

Where,

$$W_i = \begin{bmatrix} 1 & 0 & -\sin \theta \\ 0 & \cos \phi & \sin \phi \cos \theta \\ 0 & -\sin \phi & \cos \phi \cos \theta \end{bmatrix} \quad (4.29)$$

and p , q , and r represent the respective angular rates in body frame. As a result, the equation for rate of change of angular position is:

$$\dot{\Theta}_i = W_i^{-1} \tilde{\omega}_b \quad (4.30)$$

with,

$$\tilde{\omega}_b = \begin{bmatrix} p \\ q \\ r \end{bmatrix} \quad (4.31)$$

For the simplicity purposes, it is assumed that the center of pressure of the airborne platform including the Magnus cylinder and the rigid frame coincides with the center of gravity of the platform.

Applying Newton's second law of motion to the ABM and using Coriolis theorem, the equation of rate of change of translational velocity in body frame is given by:

$$\dot{\vec{v}}_b = \frac{1}{m} (\vec{F}_b - \tilde{\omega} \vec{v}_b) \quad (4.32)$$

Where,

$$\tilde{\omega} = \begin{bmatrix} 0 & -r & q \\ r & 0 & -p \\ -q & p & 0 \end{bmatrix} \quad (4.33)$$

and \vec{F}_b is the total body force acting on the ABM expressed in body frame, and is the sum of all the forces acting on the Magnus cylinder. Thus, F_b is expressed as:

$$\vec{F}_b = \vec{F}_L + \vec{F}_D + \vec{F}_{dy} + \vec{W}_b + \vec{F}_{bu} + \vec{F}_r \quad (4.34)$$

Where, \vec{F}_L and \vec{F}_D present the lift and drag force respectively. They are expressed in (x_b, z_b) plane. \vec{F}_{dy} is the drag force acting on the ABM in y_b direction.

To develop a model independent of the control surfaces, the forces acting due to the rudder is not considered in this section. Rudder forces are discussed in detail and incorporated into the model in section 4.3.1 with the new F_b given by equation 4.74.

The aerodynamic forces, \vec{F}_L , \vec{F}_D , and \vec{F}_{dy} are expressed as:

$$\vec{F}_L = \frac{1}{2} \rho S_{cyl} (\vec{v}_{axz})^2 C_L \vec{e}_{F_l} \quad (4.35)$$

$$\vec{F}_D = \frac{1}{2} \rho S_{cyl} (\vec{v}_{axz})^2 C_D \vec{e}_{F_d} \quad (4.36)$$

$$\vec{F}_{dy} = \frac{1}{2} \rho S_{cyl} (\vec{v}_{ay})^2 C_{dy} \vec{y}_b \quad (4.37)$$

Where, S_{cyl} is the projected surface area of the Magnus cylinder, C_L is the coefficient of lift, C_D is the coefficient of drag, and C_{dy} is the drag coefficient of the ABM along \vec{y}_b axis. \vec{e}_{F_L} , \vec{e}_{F_D} and \vec{y}_b are unit vectors in the direction of lift, drag and y_b axis. \vec{e}_{F_l} and \vec{e}_{F_d} are defined as:

$$\vec{e}_{F_d} = \begin{bmatrix} 1 \\ 0 \\ 1 \end{bmatrix} \cdot \frac{\vec{v}_a}{|(\vec{v}_a)|} \quad (4.38)$$

$$\vec{e}_{F_l} = \vec{y}_b \times \vec{e}_{F_d} \quad (4.39)$$

Where, "." is an element-wise product operator, and "×" represents the vector cross product. The apparent wind velocity \vec{v}_a , as shown in figure 4.3, is decomposed into two components, \vec{v}_{ay} acting in the \vec{y}_b direction and the other \vec{v}_{axz} acting in the (x_b, z_b) plane, and they are expressed in the body frame as:

$$\vec{v}_a = \vec{v}_{wb} - \vec{v}_b \quad (4.40)$$

$$\vec{v}_{axz} = \vec{v}_a \cdot \begin{bmatrix} 1 \\ 0 \\ 1 \end{bmatrix} = v_{axz} \vec{e}_{F_d} \quad (4.41)$$

$$\vec{v}_{ay} = \vec{v}_a \cdot \begin{bmatrix} 0 \\ 1 \\ 0 \end{bmatrix} = v_{ay} \vec{y}_b \quad (4.42)$$

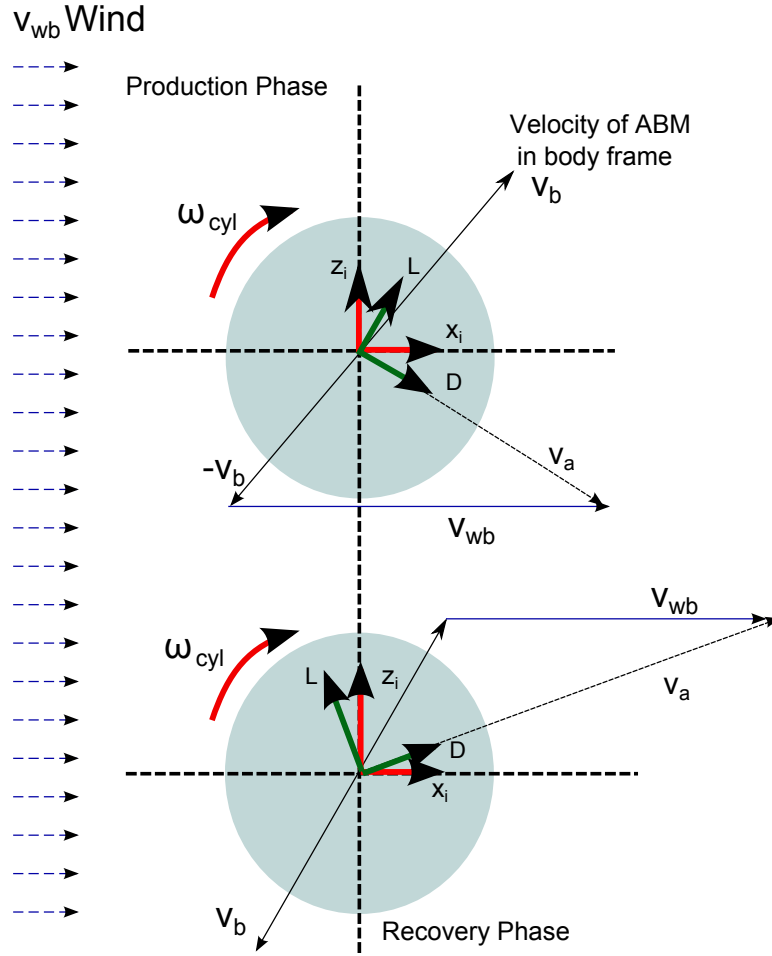


Figure 4.3: Apparent Wind velocity in different phases

Where, "." is an element-wise product operator, and \vec{v}_b is the translational velocity of the ABM expressed in body frame. \vec{v}_{wb} is the wind velocity also expressed in body frame as:

$$\vec{v}_{wb} = \vec{v}_w R_b^i \quad (4.43)$$

\vec{W}_b and \vec{F}_{bu} represent the weight and buoyancy forces acting on the ABM in the opposite direction. Since, the weight of the ABM and the buoyancy force are acting in the z_i direction, rotational matrices are used to express them in the body frame. They are expressed as:

$$\vec{g}_b = R_b^i \begin{bmatrix} 0 \\ 0 \\ -g \end{bmatrix} \quad (4.44)$$

$$\vec{W}_b = m \vec{g}_b \quad (4.45)$$

$$\vec{F}_{bu} = -\rho r_{cyl}^2 \pi l_{cyl} \vec{g}_b \quad (4.46)$$

Where, g is the gravitational constant, and m is the total mass of the ABM .i.e. the sum of the mass of the structure, m_{struct} , and the mass of the Magnus rotor filled with a gas of

density ρ_{gaz} :

$$m = m_{struct} + \rho_{gaz} r_{cyl}^2 \pi l_{cyl} \quad (4.47)$$

All the forces illustrated in figure 4.4 are expressed in the body frame. \vec{F}_r is the tether force applied at the ground station and is evaluated from the dynamic model of the winch:

$$\frac{J_z}{R_d} \ddot{r}_t = R_d \vec{F}_r + T_c \quad (4.48)$$

Where, J_z is the moment of inertia of the winch, R_d is its radius and T_c is the torque produced by the electric actuator. The length of the tether is given by $r_t = \sqrt{(x_i^2 + y_i^2 + z_i^2)}$ and F_r represents the norm of the tether force applied on the ABM:

$$\vec{F}_r = \frac{J_z}{R_d^2} \ddot{r}_t - \frac{T_c}{R_d} \quad (4.49)$$

As \vec{F}_r is evaluated at the ground station in the tether direction. It is expressed in body frame as:

$$\vec{F}_r = F_r R_b^i \frac{\vec{r}_i}{\|\vec{r}_i\|} \quad (4.50)$$

Finally, the winch torque T_c is controlled by the reference variable u_T which acts through a current loop modeled by a first order dynamic system:

$$\dot{T}_c = \beta_T (u_T - T_c) \quad (4.51)$$

where, β_T is homogeneous to a frequency representing its dynamic response.

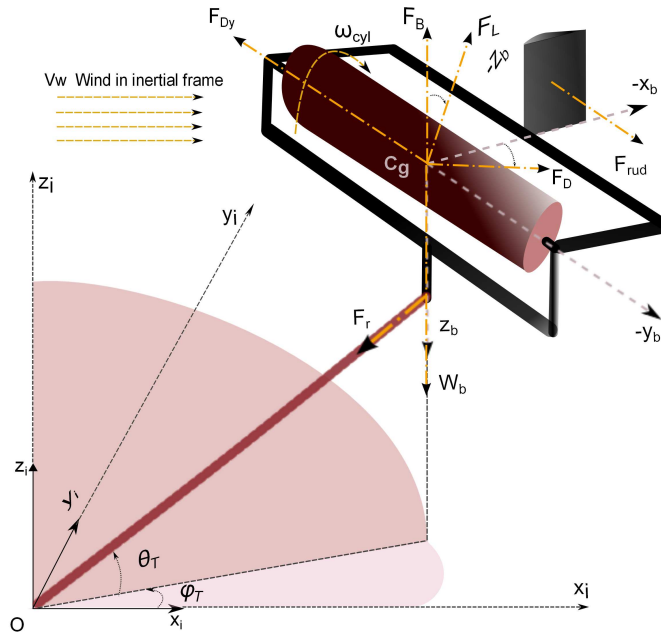


Figure 4.4: The forces acting on the Magnus cylinder.

4.3 Moments acting on Magnus-based AWE System

In order, to precisely analyze the attitude and the stability of the ABM, a thorough analysis of the rotational motion of the ABM is necessary, which calls for the analysis of the moments that come into being. In literature, there is very little data available on the body moments and their effect on the rotational stability of the Magnus cylinder. There are even lesser papers and books analyzing the effects of torque on rotating Magnus cylinder. However, there is an extensive literature available on airfoils describing the different moments in detail. Hence, simplified moment expressions, based on aircraft flight dynamics, are developed to fit the design of Magnus cylinder. The sign conventions used here are that of the flight dynamics.

Assuming the prototype as a rigid structure, the rate of change of angular position in body frame is given by:

$$\dot{\Theta} = W_i^{-1}\tilde{\omega} \quad (4.52)$$

with,

$$\tilde{\omega} = \begin{bmatrix} p \\ q \\ r \end{bmatrix} \quad (4.53)$$

and,

$$W_i = \begin{bmatrix} 1 & 0 & -\sin\theta \\ 0 & \cos\phi & \sin\phi\cos\theta \\ 0 & -\sin\phi & \cos\phi\cos\theta \end{bmatrix} \quad (4.54)$$

Where, p , q , r represent the angular rates about their respective axis in the body frame, and W_i is the result of the transformation of the local axis of rotation (i.e. p about y_1 and r about z_i axis) into body frame.

Applying Newton's second law to the rotational motion of the ABM, the equation of rate of change of angular velocity obtained is:

$$\dot{\omega} = I^{-1}(M_b - \tilde{\omega}I\omega) \quad (4.55)$$

Where, I represents the moment of inertial matrix and M_b is the sum of all the moments acting on the ABM expressed in the body frame.

The moment of inertia is evaluated around the principal axis. For simplicity sake, the contribution of the rigid structure to the Magnus rotor inertia is neglected.

$$I = \begin{bmatrix} I_{xx} & I_{xy} & I_{xz} \\ I_{yx} & I_{yy} & I_{yz} \\ I_{zx} & I_{zy} & I_{zz} \end{bmatrix} \quad (4.56)$$

Also, due to the symmetrical design of the Magnus cylinder the product moment of inertia i.e. I_{xy} , I_{xz} , I_{yx} , I_{yz} , I_{zx} , and I_{zy} , all are assumed to be zero. Hence, the inertial matrix I is expressed as :

$$I = \begin{bmatrix} I_{xx} & 0 & 0 \\ 0 & I_{yy} & 0 \\ 0 & 0 & I_{zz} \end{bmatrix} \quad (4.57)$$

The body moments M_b acting on the ABM can be broadly attributed to three effects :

- **Aerodynamic Moments:** They arise due to the interaction between the various aerodynamic forces which come into play due to the geometrical asymmetry of the Magnus prototype as well as due to the action of the control surfaces such as rudder, ailerons etc.
- **Gyroscopic Torque:** As the Magnus-based AWE comprises of a rotating cylinder, the well documented gyroscopic effect comes into being whenever the ABM undergoes precession about z_b or x_b axis.
- **Reactive Torque:** The reactive torque is produced by the tether force generated in the tether due to an offset between the C_g and the bridle point. This torque is responsible for aligning the ABM with the tether.

Hence,

$$M_b = \begin{bmatrix} l_b \\ m_b \\ n_b \end{bmatrix} = M_{aero} + M_{gyro} + M_{reac} \quad (4.58)$$

Where, l_b represents the total moments acting about x_b axis commonly referred as Rolling moment, m_b represents the total moments acting about y_b axis commonly referred as Pitch moment, and n_b represents the total moments acting about z_b axis commonly referred as Yaw moment.

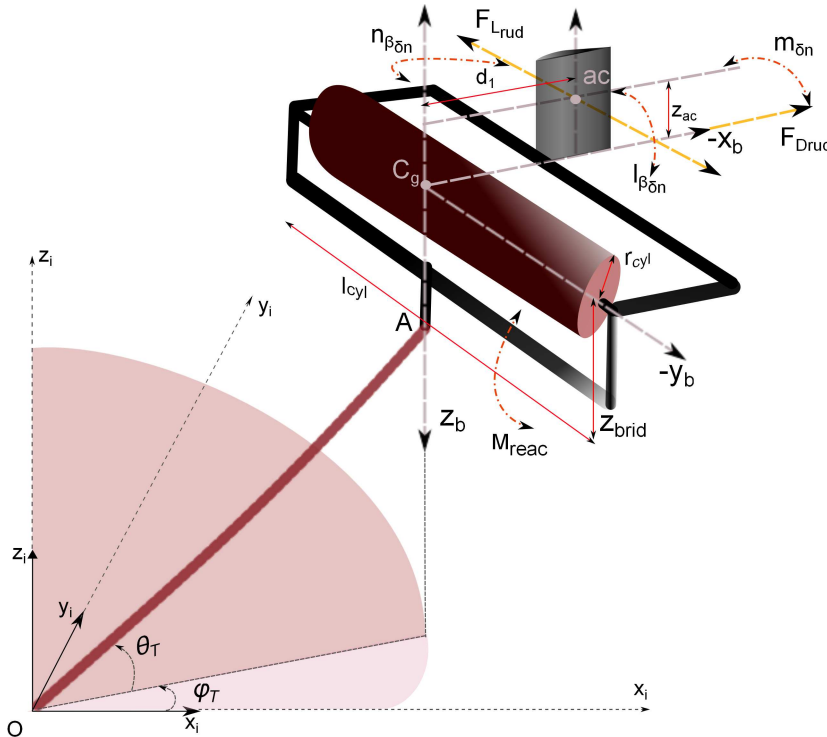


Figure 4.5: Various moments acting on the Magnus-based AWE system.

4.3.1 Aerodynamic Moments

Aerodynamic moments are the torques that come into being due to the differences in lift and drag forces produced by the different sections of any airborne system. These differences stem from various parameters such as changes in angular rates (p, q, r), action of control surfaces (such as rudder, ailerons, elevator etc.) or changes in side-slip (β) or angle of attack (α), etc. In flight dynamics, the coefficient of roll, pitch, and yaw, .i.e. C_l , C_m , and C_n are used to account for all the moments arising from these effects and they are usually expressed as:

$$C_l = C_{l0} + C_{l\alpha}\alpha + C_{l\beta}\beta + C_{lh}h + C_{lV}V + C_{lp}p + C_{lq}q + C_{lr}r \quad (4.59)$$

$$C_m = C_{m0} + C_{m\alpha}\alpha + C_{m\beta}\beta + C_{mh}h + C_{mV}V + C_{mp}p + C_{mq}q + C_{mr}r \quad (4.60)$$

$$C_n = C_{n0} + C_{n\alpha}\alpha + C_{n\beta}\beta + C_{nh}h + C_{nV}V + C_{np}p + C_{nq}q + C_{nr}r \quad (4.61)$$

These moment coefficients takes into account all the factors contributing to moments about their respective axis .i.e. x_b , y_b , and z_b . Each coefficient .i.e. C_l , C_m , and C_n is a linear combination of all the contributing factors. For example, $C_{n\beta}$ represents the yaw moment coming into being due to the presence of sideslip β (using flight dynamics sign conventions and notations). The estimation of these aerodynamic moment coefficients (such as $C_{n\beta}$, C_{lq} , C_{mr} , etc. presented in equations 4.61) is usually done by wind tunnel testing or CFD analysis. As this is beyond the scope of this work, the above mentioned formalism is not used in this work. Instead, moment expressions respective to each effect is determined seperately. Thus, to develop a good simulation model of the ABM simplified expression for some of the expected dominant effects are developed and presented in the subsequent sections.

The aerodynamic moments as experienced by the ABM is a combination of yaw, pitch and roll moments. The main contributors of aerodynamic moments which are expected to have a considerable effect on the ABM and which are considered in this study are:

- **Rudder Dynamics :** Resulting in a combination of roll, pitch and yaw, $(l_{\beta\delta_n}, m_{\beta\delta_n}, n_{\beta\delta_n})$, from the deflection of rudder and its geometry.
- **Aerodynamic Moments due to yaw rate :** Resulting in a combination of roll, (l_{pr}) , and yaw moment, (n_r) , from the changes in yaw rate.

Thus, the total aerodynamic moments can be expressed as:

$$M_{aero} = \begin{bmatrix} l_{aero} \\ m_{aero} \\ n_{aero} \end{bmatrix} = \begin{bmatrix} l_{\beta\delta_n} \\ m_{\beta\delta_n} \\ n_{\beta\delta_n} \end{bmatrix} + \begin{bmatrix} l_{pr} \\ 0 \\ n_r \end{bmatrix} \quad (4.62)$$

Where, l_{aero} represents the total aerodynamic roll moment acting about the x_b axis, m_{aero} represents the total aerodynamic pitch moment acting about the y_b axis, and n_{aero} represents the total aerodynamic yaw moment acting about the z_b axis.

4.3.1.1 Rudder Dynamics

To provide directional stability and controllability a rudder is added in the negative \vec{x}_b direction to the prototype as shown in figure 4.2, an addition to the design presented in [119]. Due to the rudder action and asymmetry of the point of action of different forces w.r.t to the C_g , the aerodynamic moments due to rudder action as experienced by the ABM is a combination of yaw, pitch and roll moments. In this case, a NACA 0012 series symmetric airfoil is considered for the design of the rudder. The coefficient of lift $C_{L_{rud}}$ and drag $C_{D_{rud}}$ for rudder is taken from the experimental data presented by Sandia national laboratories [125]. Figures 4.6 and 4.7 present the $C_{L_{rud}}$ and $C_{D_{rud}}$ data for the rudder extrapolated for -180 to 180 degrees.

Sandia presents the experimental data for both increasing and decreasing angle of attack varying from -24 to 32 degrees for a wind turbine in order to validate the symmetric nature of the airfoil and its respective aerodynamic coefficients. The study then presents the experimental data for C_L and C_D for increasing angle of attack from 0 to 180 degrees for different types of airfoils and for different Reynolds number ranging from 10^4 to 10^7 . The operating Reynolds number range of ABM is expected to be around 10^6 and as validated in the Sandia study symmetric behavior is observed for the negative angle of attack. Figures 4.6 and 4.7 presents this data extrapolated for negative angle of attack ranging from -180 to 180 degrees. For the negative angle of attack, it is observed that the $C_{L_{rud}}$ becomes negative and is maximum for about ± 15 degrees. The drag coefficient $C_{D_{rud}}$ is maximum at around ± 90 degrees as at such a high angle of attack airfoil behaves like a flat plate.

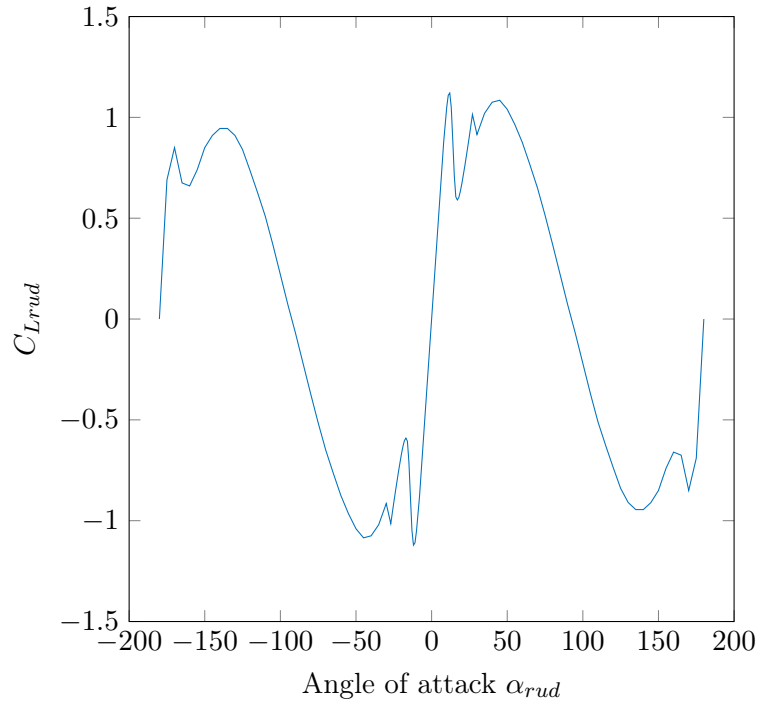


Figure 4.6: The lift coefficient $C_{L_{rud}}$ as a function of angle of attack

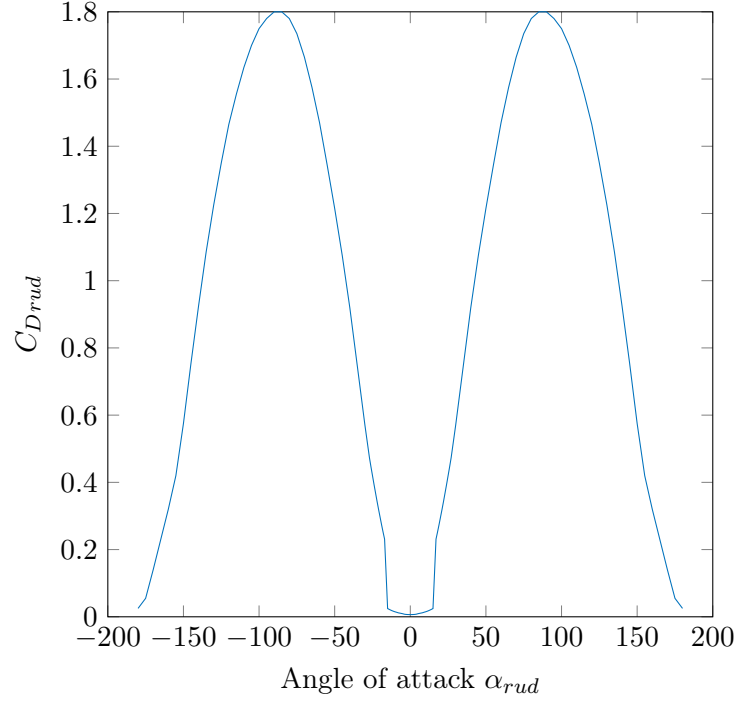


Figure 4.7: The lift coefficient $C_{D_{rud}}$ as a function of angle of attack.

\vec{F}_{dy} represents the drag force, also known as side force, acting on the ABM in y_b direction due to the Magnus effect. Rudder contributes an additional side force which can be approximated by:

$$\vec{F}_{L_{rud}} = \frac{1}{2} \rho S_{rud} (\vec{v}_{axy_{rud}})^2 C_{L_{rud}} \vec{e}_{Fl_{rud}} \quad (4.63)$$

Similarly, the drag force due to rudder is given by:

$$\vec{F}_{D_{rud}} = \frac{1}{2} \rho S_{rud} (\vec{v}_{axy_{rud}})^2 C_{D_{rud}} \vec{e}_{Fd_{rud}} \quad (4.64)$$

Where, $C_{L_{rud}}$ and $C_{D_{rud}}$ represent the coefficient of lift and drag for the rudder, $\vec{e}_{Fl_{rud}}$ and $\vec{e}_{Fd_{rud}}$ represent unit vectors in $\vec{F}_{L_{rud}}$ and $\vec{F}_{D_{rud}}$ direction respectively and are defined as:

$$\vec{e}_{Fd_{rud}} = \frac{\vec{v}_{axy_{rud}}}{\|(\vec{v}_{axy_{rud}})\|} \quad (4.65)$$

$$\vec{e}_{Fl_{rud}} = \vec{z}_b \times \vec{e}_{Fd_{rud}} \quad (4.66)$$

Where, "." is an element-wise product operator, and " \times " represents the vector cross product.

$\vec{v}_{axy_{rud}}$ is the apparent wind velocity experienced by the rudder in x_b - y_b plane, consisting of velocity components, v_{ar_x} and v_{ar_y} in x_b and y_b directions respectively and is defined as:

$$\vec{v}_{axy_{rud}} = \begin{bmatrix} v_{ar_x} \\ v_{ar_y} \\ 0 \end{bmatrix} = \begin{bmatrix} 1 \\ 1 \\ 0 \end{bmatrix} \cdot \vec{v}_a + \begin{bmatrix} 0 \\ rd_1 \\ 0 \end{bmatrix} \quad (4.67)$$

Where, rd_1 is the tangential velocity component arising due to the yaw rate r around z_b axis. And d_1 is the distance of the rudder from the center of gravity. This distance must be chosen such that the rudder lies ahead of the wake region of the Magnus cylinder. In this case, as the study of the aerodynamic properties of the Magnus cylinder is beyond the scope of this work, it is assumed that

$$d_1 > ar_{cyl} \quad (4.68)$$

Where, a is a constant whose value must be chosen such that it puts the rudder outside the wake region of the cylinder. In simulations, the value of (a) is set to as 1.5. However, this is just an assumption and for practical design this assumption must be validated by experimental aerodynamic data.

Here it is important to note that the apparent wind is limited to (x_b, z_b) plane for rudder because the aim is to take into account only the pure roll, pitch and yaw moment arising due to rudder dynamics. However, in reality due to the presence of the component of v_a in the direction of z_b .i.e. (v_{ar_z}) , it would result in $\vec{F}_{L_{rud}}$ and $\vec{F}_{D_{rud}}$ having components in all three directions .i.e. $(\vec{x}_b, \vec{y}_b, \vec{z}_b)$. The z_b component of $\vec{F}_{L_{rud}}$ and $\vec{F}_{D_{rud}}$.i.e. $\vec{F}_{L_{rud}Z}$ and $\vec{F}_{D_{rud}Z}$ would result in a combination of roll and pitch moment and it can be considered separately as F_{dy} is considered for the airborne platform in equation 4.37. However, the effects of these moments arising due to (v_{ar_z}) is for now neglected in this formulation and only the effect of the side force generated by the rudder action is considered in this model. Also, the yaw moment due to the side force (.i.e. $\vec{F}_{L_{rud}}$) produced by the rudder is much higher than other the roll and pitch moments resulting due to (v_{ar_z}) . Nonetheless, by considering:

$$\vec{v}_{axy_{rud}} = \vec{v}_a, \quad (4.69)$$

$$\vec{e}_{Fd_{rud}} = \frac{\vec{v}_a}{\|(\vec{v}_a)\|} \quad (4.70)$$

these effects can be taken into account by directly using the expressions for aerodynamic moments mentioned in subsequent sections. However, in this fomulation $\vec{v}_{axy_{rud}}$, and $\vec{e}_{Fd_{rud}}$ are expressed by equation 4.67 and 4.65.

In this design, rudder is considered as a vertical tail plane, therefore, the combined deflection of the rudder and the presence of sideslip leads to an effective angle of attack, α_{rud} , given by:

$$\beta_{rud} = \arctan\left(\frac{v_{ary}}{v_{arx}}\right) \quad (4.71)$$

$$\alpha_{rud} = \beta_{rud} - \delta_n \quad (4.72)$$

Where, α_{rud} is considered to be positive when the wind flow is coming from the right side of the \vec{x}_b direction and negative if the incoming wind is from the left side of the \vec{x}_b . δ_n represents the rudder deflection. It is considered to be positive when the rudder is deflected to left resulting in a positive side force, and is considered negative when the rudder is deflected to right. Therefore, a positive side-slip produces a negative side force $\vec{F}_{L_{rud}}$.i.e. in $-\vec{y}_b$ direction where as a negative side-slip leads to a positive $\vec{F}_{L_{rud}}$. And $\vec{F}_{L_{rud}}$ is zero when there is no sideslip, no yaw rate (r) and there is no rudder deflection i.e. the apparent wind velocity

$\vec{v}_{axy_{rud}}$ is perfectly aligned with x_b and $\delta_n = 0$. Hence, the total force due to rudder can be expressed as:

$$\vec{F}_{rud} = \vec{F}_{L_{rud}} + \vec{F}_{D_{rud}} \quad (4.73)$$

Thus, the total body force, F_b , acting on the ABM is:

$$\vec{F}_b = \vec{F}_L + \vec{F}_D + \vec{F}_{dy} + \vec{W}_b + \vec{F}_{bu} + \vec{F}_r + \vec{F}_{rud} \quad (4.74)$$

Aerodynamic moments due to rudder: As shown in the figure 4.5 the aerodynamic center of the rudder is located at a distance \vec{d}_r from the C_g of the ABM expressed as:

$$\vec{d}_r = \begin{bmatrix} d_1 \\ 0 \\ z_{ac} \end{bmatrix} \quad (4.75)$$

Where, d_1 is the distance of aerodynamic center of the rudder from C_g in $-x_b$ direction and z_{ac} is its distance in $-z_b$ direction. Due to the presence of effective angle of attack (α_{rud}) and the location of the aerodynamic center of the rudder, the rudder action results in a combination of roll, pitch and yaw moments expressed as:

$$\begin{bmatrix} l_{\beta\delta_n} \\ m_{\beta\delta_n} \\ n_{\beta\delta_n} \end{bmatrix} = \vec{d}_r \times \vec{F}_{rud} \quad (4.76)$$

Figure 4.8 shows the resulting yaw moment due to the combined effect of the side-slip and rudder deflection.

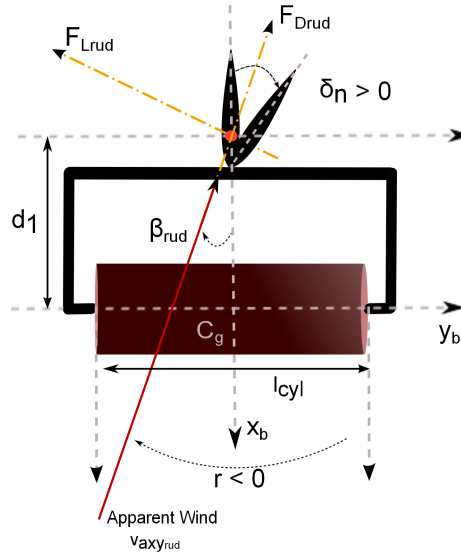


Figure 4.8: Yaw moment due to rudder

4.3.1.2 Aerodynamic Moments due to yaw rate

Another significant contributor to the aerodynamic moment is the moment produced due to the angular rates. When there is a rudder deflection or sideslip the ABM rotates around z_b

axis with a yaw rate r either in clockwise direction .i.e. when $r < 0$ or in anti-clockwise direction .i.e. when $r > 0$.

Supposing the ABM moves in the clockwise direction, then the right side of the Magnus cylinder rotates against the flow field leading to an increase in the apparent wind velocity. Similarly, the left side moves along the flow field leading to a decrease in the apparent wind velocity. This results in the production of greater lift and drag forces from the right side of the Magnus cylinder in comparison to that of the left side of the cylinder. Hence, resulting in both yaw and roll moment. This effect in flight dynamics is called as Weathercock effect. When the ABM moves in anti-clockwise direction the effect is reversed. Thus, the left side of the Magnus cylinder experiences greater lift and drag force as compared to the left side.

Assuming that the Magnus cylinder is made up of two different cylinders of equal length, $\frac{l_{cyl}}{2}$, seperated at the C_g of the larger cyinder, and assuming the Magnus cylinder rotates in clockwise direction. The relative wind velocity experienced by each cylinder at any time at their respective C_g will be:

$$\vec{V}_{rel_right} = \vec{v}_a \cdot \begin{bmatrix} 1 \\ 0 \\ 1 \end{bmatrix} + \begin{bmatrix} r \frac{l_{cyl}}{4} \\ 0 \\ 0 \end{bmatrix} \quad (4.77)$$

$$\vec{V}_{rel_left} = \vec{v}_a \cdot \begin{bmatrix} 1 \\ 0 \\ 1 \end{bmatrix} - \begin{bmatrix} r \frac{l_{cyl}}{4} \\ 0 \\ 0 \end{bmatrix} \quad (4.78)$$

Where, "." is the element wise operator. Note, here $r \frac{l_{cyl}}{4}$ represents the tangential velocity of the C_g of each cylinder while undergoing a rotation about z_b axis at an angular rate r .

Assuming the center of pressure for each cylinder coincides with the geometric center of each cylinder and as each cylinder experiences different relative wind, the lift and drag for each part of the cylinder acting on the C_g of each cylinder will be different and can be expressed as:

$$\vec{F}_{Lleft} = \frac{1}{2} \rho \left(\frac{S_{cyl}}{2} \right) (\vec{V}_{rel_left})^2 C_{L_{lt}} \vec{e}_{L_l} \quad (4.79)$$

$$\vec{F}_{Lright} = \frac{1}{2} \rho \left(\frac{S_{cyl}}{2} \right) (\vec{V}_{rel_right})^2 C_{L_{rg}} \vec{e}_{L_r} \quad (4.80)$$

$$\vec{F}_{Dleft} = \frac{1}{2} \rho \left(\frac{S_{cyl}}{2} \right) (\vec{V}_{rel_left})^2 C_{D_{lt}} \vec{e}_{D_l} \quad (4.81)$$

$$\vec{F}_{Dright} = \frac{1}{2} \rho \left(\frac{S_{cyl}}{2} \right) (\vec{V}_{rel_right})^2 C_{D_{rg}} \vec{e}_{D_r} \quad (4.82)$$

Where, \vec{e}_{L_r} , \vec{e}_{L_l} , \vec{e}_{D_l} and \vec{e}_{D_r} are unit vectors representing the direction of lift and drag for

each part of the cylinder, and are defined as:

$$\vec{e}_{D_l} = \frac{\vec{V}_{rel_{left}}}{\|(\vec{V}_{rel_{left}})\|} \quad (4.83)$$

$$\vec{e}_{L_l} = \vec{y}_b \times \vec{e}_{D_l} \quad (4.84)$$

$$\vec{e}_{D_r} = \frac{\vec{V}_{rel_{right}}}{\|(\vec{V}_{rel_{right}})\|} \quad (4.85)$$

$$\vec{e}_{L_r} = \vec{y}_b \times \vec{e}_{D_r} \quad (4.86)$$

Where, "." is an element-wise product operator, and "×" represents the vector cross product. $C_{L_{lt}}$, $C_{L_{rg}}$, $C_{D_{lt}}$, and $C_{D_{rg}}$ are the coefficient of lift & drag for each cylinder for their respective spin ratio .i.e. X_{lt} and X_{rg} , calculated as:

$$X_{lt} = \frac{\omega_{cyl} r_{cyl}}{V_{rel_{left}}} \quad (4.87)$$

$$X_{rg} = \frac{\omega_{cyl} r_{cyl}}{V_{rel_{right}}} \quad (4.88)$$

Thus, the resultant aerodynamic force acting on each part of the cylinder can be given as:

$$\vec{F}_{a_{left}} = \sqrt{(\vec{F}_{L_{left}})^2 + (\vec{F}_{D_{left}})^2} \quad (4.89)$$

$$\vec{F}_{a_{right}} = \sqrt{(\vec{F}_{L_{right}})^2 + (\vec{F}_{D_{right}})^2} \quad (4.90)$$

Hence, the roll and yaw arising due to the difference between the lift & drag produced by each cylinder can be expressed as:

$$\begin{bmatrix} \vec{l}_{pr} \\ 0 \\ \vec{n}_r \end{bmatrix} = \begin{bmatrix} 0 \\ \frac{l_{cyl}}{4} \\ 0 \end{bmatrix} \times \vec{F}_{a_{left}} + \begin{bmatrix} 0 \\ -\frac{l_{cyl}}{4} \\ 0 \end{bmatrix} \times \vec{F}_{a_{right}} \quad (4.91)$$

In a similar way, when the ABM undergoes a rolling movement, it will result in yaw and roll moments around their respective axis. However, this effect is neglected in this thesis work, and can be included in a similar way in the future analyses.

Also, as the Magnus cylinder is independent of the angle of attack and for now, the use of a horizontal stabilizer is not considered in this prototype. It is assumed that the longitudinal stability is provided only by the reactive torque produced by the tether, explained in section 4.3.3.

4.3.2 Gyroscopic couple

Gyroscopic effects come into being when a rotating body undergoes precession about another axis. As the Magnus cylinder is spinning about y_b axis, torque due to gyroscopic effects come into being whenever the ABM undergoes a rolling moment or a yaw moment .i.e. rotation

about x_b or z_b axis. In other words, a torque is produced around x_b axis whenever there is a precession about z_b axis or vice-versa. The gyroscopic couple can be expressed as:

$$\tau_{gyro_x} = I_{yy}\omega_{cyl}r \quad (4.92)$$

$$\tau_{gyro_z} = I_{yy}\omega_{cyl}p \quad (4.93)$$

Where, ω_{cyl} is the angular spin velocity of the Magnus cylinder about y_b axis, r is the angular rate about z_b axis, commonly referred to as yaw rate, p is the angular rate about x_b axis, commonly known as roll rate, and I_{yy} is the principal moment of inertia about y_b axis. As the Magnus cylinder is free to rotate about the y_b axis no gyroscopic couple comes into being about the y_b axis.

$$\tau_{gyro_y} = 0 \quad (4.94)$$

Hence, the total gyroscopic torque can be expressed as:

$$M_{gyro} = \begin{bmatrix} \tau_{gyro_x} \\ \tau_{gyro_y} \\ \tau_{gyro_z} \end{bmatrix} \quad (4.95)$$

4.3.3 Reactive Torque

A reactive torque acts on the ABM due to the forces generated in the tether. The bridle point is considered to be at a distance of \vec{R}_{bridle} from the C_g as shown in figure 4.5. The force components in the three directions produces a couple around C_g about x_b and y_b axis and is given by:

$$\vec{R}_{bridle} = \begin{bmatrix} 0 \\ 0 \\ z_{brid} \end{bmatrix} \quad (4.96)$$

Where, downward z_b is considered as positive. Therefore, the reactive torque, M_{reac} can be calculated as:

$$M_{reac} = \vec{R}_{bridle} \times \vec{F}_r \quad (4.97)$$

This reactive torque is responsible for aligning the ABM with the tether as at equilibrium it compensates all the other forces and moments acting about C_g . This results in natural self-alignment of the 3 points O , A and C_g , and \vec{z}_b with the tether.

4.4 Control Strategy

4.4.1 Global Control Scheme

The guidance strategy is adopted from that proposed in [34] and is discussed in section 4.4.2. To maximize the power production, the spin ratio X_{max} is used for the Magnus rotor and the ABM is made to follow an eight figured trajectory by controlling of a specific angle γ , also

known as heading angle in flight dynamics. Physically, γ represents the angle between the velocity vector of the ABM, given by equation 4.26 in the inertial frame, and the local north defined on the horizon. In this case, the local north is equivalent to the x_b direction obtained by ZYZ transformation of the inertial frame (x_i, y_i, z_i) as mentioned in section 4.2.2.1. In the spherical coordinate system, it corresponds to the angle expressing the rotation around the tether length r_t and can be directly obtained by transformation R_s^i presented in section 4.2.2.1. If $\gamma = 0$ it means that the ABM moves towards the zenith, and if $\gamma = \pi/2$ it means that the ABM follows the local east and moves parallel to the ground. If $\gamma = \pi$ it means that the ABM moves towards the ground. The γ can be controlled by a rudder or any other device that can produce torque around z_b . In the case of the usage of rudder as a control surface the apparent wind should be non-zero in x_b direction.

The reactive torque acting on the ABM is responsible for aligning the ABM and tether. It is assumed here that the self-alignment of the ABM is done smoothly and significantly faster than other considered system dynamics in order to neglect it. It is also assumed that an appropriate actuator, like a suitably sized rudder, is used to steer the ABM to the desired heading γ_{ref} .

In simulations subsequently presented in section 4.5, \vec{z}_b is forced in the direction of the origin, due to the self-alignment of the body axis z_b with the tether, and γ follows the reference γ_{ref} through a first-order dynamic system:

$$\dot{\gamma} = \beta_\gamma(\gamma_{ref} - \gamma) \quad (4.98)$$

Where, β_γ is homogeneous to a frequency representing its dynamic response. The reference γ_{ref} is computed by the guidance law and depends on the trajectory being followed by the ABM. It is defined in detail in section 4.4.2.

Finally, a control loop on the spin of the cylinder is assumed to be set properly and is modeled by a first order dynamic system:

$$\dot{\omega}_{cyl} = \beta_{\omega_{cyl}}(\omega_{cyl_{ref}} - \omega_{cyl}) \quad (4.99)$$

Where, $\beta_{\omega_{cyl}}$ is homogeneous to a frequency representing its dynamic response. ω_{cyl} represents the spin of the cylinder and $\omega_{cyl_{ref}}$ represents the reference spin of the cylinder.

In addition to this, a PID controller K_1 is used to control the reference position by controlling the tether length through the torque of the winch actuator. This outer control loop has a faster response time in order to compensate for the variations in other forces acting on the ABM. Figure 4.9 represents the control strategy adopted for controlling the tether length.

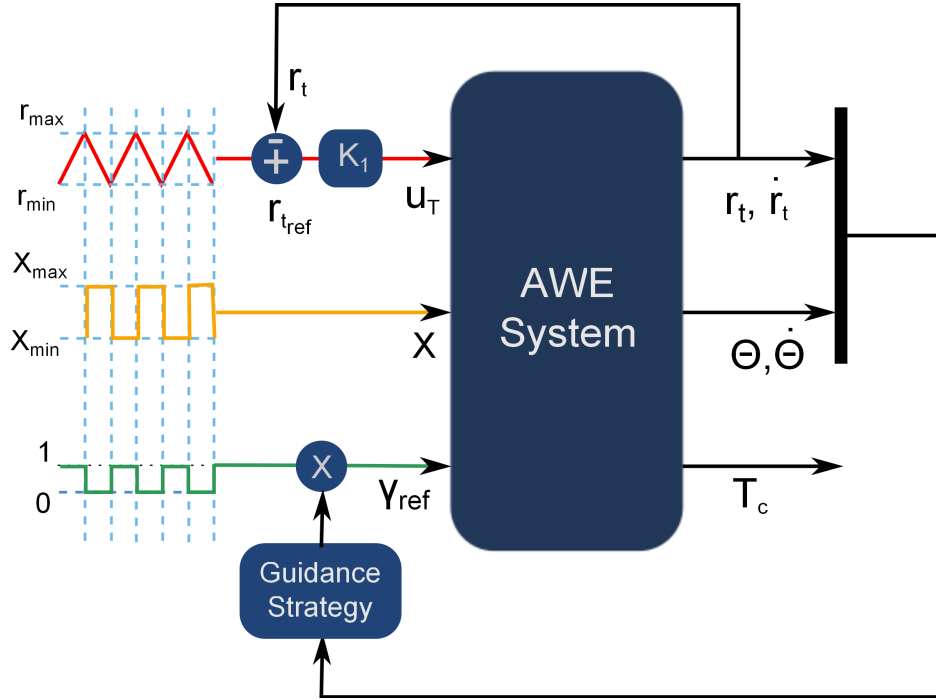


Figure 4.9: An overview of the control strategy. The Magnus rotor moves from minimum radial position r_{min} to a maximum radial position r_{max} .

4.4.2 Guidance strategy

4.4.2.1 Eight-Figure Trajectory Guidance Law:

The guidance strategy to make a figure eight loop as proposed in [34] is adopted to make the ABM follow a crosswind maneuver. The strategy is defined in the spherical coordinate system and utilizes the orientation of the tether with respect to the inertial frame to define a guidance algorithm. However, the effects of tether drag and curvature were not taken into account in this strategy.

In the spherical coordinate system, the position of any point is defined by the radial distance l , and two angles namely, azimuth angle ϕ and polar angle θ . Thus, the position of any point X is given by (l, ϕ, θ) . In this formulation for the ease of notation for the design purposes, the position of the C_g of the ABM is defined by the tether length r_t , azimuthal angle is represented by ϕ_T , and elevation angle by θ_T which is equivalent to $(90 - \theta)$.i.e. complement of the polar angle. Thus, the position of the C_g of ABM is given by (r_t, ϕ_T, θ_T) as shown in figure 4.10.

To make the eight-figured loop, two reference points denoted by $P_- = (\theta_{T-}, \phi_{T-})$ and $P_+ = (\theta_{T+}, \phi_{T+})$ are defined on the spherical horizon as shown in figure 4.10 with the origin representing the location of the ground station of the AWE system. Figure 4.10 shows the

Finally, in order to get the eight-figured trajectories of same width for different tether lengths, so that the power produced during the production phase is stable, ϕ_{Tref} is set as a function of tether length r_t :

$$\phi_{Tref} = \frac{K_{\phi_T}}{r_t} \quad (4.104)$$

Where, K_{ϕ_T} is a proportional gain on the azimuth angle reference. If it is necessary to fly at the same altitude, the same approach can also be done for θ_{Tref} .

4.4.2.2 Circular Trajectory Guidance Law:

Circular orbits is another way to make a crosswind maneuver in the air. The proposed guidance strategy utilizes the spherical coordinate system and the orientation of the tether.

To make a circular orbit a reference center of the circle is defined on the horizon about which the ABM is made to follow a circular orbit. Figure 4.11 presents a circular orbit with its center defined by an elevation angle θ_o and azimuthal angle ϕ_o . Any arbitrary point on the circle is defined by the elevation angle θ_T and the azimuth angle ϕ_T .



Figure 4.11: Circular orbit guidance law.

Assuming that at the initial time $\gamma = 0$.i.e. the ABM is headed towards the zenith. In order to follow a circular orbit of a defined radius, the velocity of the ABM should always be tangent to the circle. The heading angle γ as defined earlier in section 4.4.1 represents the angle between the local north and velocity. Thus, to make the circular orbit γ_{ref} should be:

$$\gamma_{ref} = \pi - \arctan\left(\frac{\theta_T - \theta_o}{\phi_T - \phi_o}\right) \quad (4.105)$$

It is important to note that for simulations a four quadrant tan function needs to be used to model the reference γ . Also, the proposed law continuously updates the γ_{ref} , a counter needs to be used when the ABM completes the first circle. Lastly, required protections need to be added in the code for cases when $\phi_T - \phi_o = 0$. Also, this control law does not consider the distance between the ABM and the center, and an extra term has to be included in the future work in order to control the radius of the circle.

4.5 Simulation Results

In section 4.5.1, a simplified model (of the system presented in section 4.2) under the static assumption is first presented. The control strategy presented in section 4.4 is used to set some of the parameters of the simulation which are discussed in section 4.5.2. Then the section 4.5.3 presents the results of the 3-D dynamic simulation for an hypothetical MW-sized Magnus effect-based AWE system. The results obtained are finally compared with that of the simplified model under static assumption as discussed in section 4.5.1.

4.5.1 Performance under Static Assumption

The motion of the Magnus cylinder is characterized into two phases, namely, production and recovery phase. A particular cycle consists of both the phases and is defined by the time period t_1 for the production phase, and t_2 for the recovery phase. The time period of each phase is calculated from the radial position of the ABM which varies between maximum r_{max} and minimum r_{min} . The reel-in r_{rec} and reel-out r_{prod} speed describes the unwinding and winding speed of the tether at the winch. By neglecting the transitional phase between the production and the recovery phase, the time period of each phase can be calculated by:

$$t_1 = \left| \frac{r_{max} - r_{min}}{r_{prod}} \right| = \frac{\Delta r}{r_{prod}} \quad (4.106)$$

$$t_2 = \left| \frac{r_{max} - r_{min}}{r_{rec}} \right| = \frac{\Delta r}{r_{rec}} \quad (4.107)$$

In the frame of equilibrium motion theory, the power that can be generated with a tethered airfoil in crosswind conditions was defined by Lyod in [10] and refined by Argatov in [126] to take into consideration the losses due to elevation angle θ_T :

$$P_{prod} = \frac{1}{2} \rho \frac{4}{27} S_{cyl} (v_w \cos(\theta_T))^3 C_L \left(\frac{C_L}{C_D} \right)^2 \quad (4.108)$$

One way to maximize this power is to maximize the ratio $C_L \left(\frac{C_L}{C_D} \right)^2$. In addition, one has to set the unwinding speed of tether during the production phase $\dot{r}_{prod} = v_w/3$. For the

considered magnus model, the maximum value of $C_L \left(\frac{C_L}{C_D}\right)^2$ is found to be for spin ratio $X = 3.6$ and is equal to 69.44. The power consumed can be calculated as the product of the winding speed of the tether \dot{r}_{rec} and the resulting drag force of the magnus rotor:

$$P_{rec} = \frac{1}{2} \rho S_{cyl} (v_w \cos(\theta_T) + \dot{r}_{rec})^2 C_{Drec} \dot{r}_{rec} \quad (4.109)$$

Where, C_{Drec} is the drag coefficient during the recovery phase. In order to get a minimal power consumption during this phase, one has to set C_L equivalent to 0 and C_D to its minimal value C_{Drec} . To achieve this, during the recovery phase the spin of the cylinder ω_{cyl} is set to 0 so that $C_L = 0$. For simulation purposes the transition phase between the production and recovery phase is neglected. Thus, the power produced during a full production cycle by the Magnus-based AWE system can be computed by:

$$P_{cycle} = \frac{P_{prod} \dot{r}_{rec} - P_{rec} \dot{r}_{prod}}{\dot{r}_{rec} + \dot{r}_{prod}} \quad (4.110)$$

Note that there is a trade-off with \dot{r}_{rec} because its augmentation not only increases the contribution of the production phase P_{prod} to the full production cycle, but also increases the power consumption P_{rec} .

The power generated by the winch during the production phase is given by :

$$P_g = r_{prod} \dot{r}_{prod} \frac{T_c}{R_d} \quad (4.111)$$

Where, r_{prod} is the unwinding of the tether, T_c is the winch torque, and R_d is the winch radius. Chapter 5 discusses in detail the static model and presents an optimization approach to obtain the optimal \dot{r}_{rec} and \dot{r}_{prod} for different wind speed so that the power produced during one complete cycle P_{cycle} is maximum.

4.5.2 Simulation Parameters

The control strategy presented in section 4.4 is applied on a 500 m^2 Magnus effect-based AWE system. Table 4.1 presents the specification of this system. Dynamics of winch current loop β_T given by equation 4.51 in section 4.2.3 has been neglected in these results as it is much faster than all the other dynamics considered in the simulation. On the other hand, the winch torque T_c is set to its maximum value T_{cmax} in order to evaluate its impact on the control strategy. Secondly, to smoothen the peaks of tension in the tether and yaw movements, a second order filter is applied on the reference tether length r_{tref} and reference heading angle γ_{ref} . Thirdly, it is important to note that as F_r is transmitted through the tether, thus, it is always negative and set between $-\infty$ and 0 to simulate this physical constraint. Finally, the respective gains of the PID controller K_1 are empirically set at $K_p = 5 \times 10^7$ N, $K_i = 0.02$ N/s, $K_d = 0.2$ Ns.

	Variable	Value
Environment Parameters		
Air density [kg/m^3]	ρ	1.225
Gravitational constant [m/s^2]	g	9.81
Wind-speed, along \vec{x}_i [m/s]	v_w	10
ABM Specifications		
Span of cylinder [m]	l_{cyl}	40
Radius of cylinder [m]	r_{cyl}	6.25
Aspect ratio	AR	3.2
Mass of airborne module [kg]	m_{struct}	6347
ABM lateral drag coefficient	C_{dy}	1.05
Maximum $C_L \left(\frac{C_L}{C_D}\right)^2$ for $X = 3.6$	$\max(C_L \left(\frac{C_L}{C_D}\right)^2)$	69.44
Reynolds number for $V = 10m/s$	Re	8.01×10^6
Winch Specifications		
Radius of winch's drum [m]	R_d	2
Maximum winch actuator torque [Nm]	$T_{c_{max}}$	4×10^6
Dynamic of winch current loop [Hz]	β_T	1000
Reel-out speed [m/s]	\dot{r}_{prod}	3.3
Reel-in speed [m/s]	\dot{r}_{rec}	13.2
Control Cycle Specifications		
Minimum radial position [m]	r_{min}	150
Maximum radial position [m]	r_{max}	300
Dynamic of speed of rotation loop [Hz]	$\beta_{\omega_{cyl}}$	1.43
Dynamic of yaw loop [Hz]	β_γ	1
Spin ratio for production phase	X_{max}	3.6
Spin ratio for recovery phase	X_{min}	0.05
Reference for elevation angle [rad]	θ_{Tref}	0.436
Coefficient for azimuth angle ref. [rad.m]	k_{ϕ_T}	13.09

Table 4.1: Simulation parameters for a 500 m^2 Magnus-based AWE system.

4.5.3 Simulation Results

The simulation results for 3 consecutive full cycles for eight-figure trajectory are presented in figure 4.12 and 4.14. It shows the 3-D trajectory of the ABM both in $(x_i - z_i)$ plane and $(y_i - z_i)$ plane. As it can be seen that the trajectory is stable and all the 3 cycles are overlapping perfectly. In the $x_i - z_i$ plane, it can be seen that the control of figure-eight trajectory is working perfectly with the elevation angle fixed at reference θ_{Tref} . In the recovery phase, the trajectory starts to go up because the cylinder takes time to go from X_{max} to X_{min} . When the spin ratio becomes equal to X_{min} the ABM starts to go down. In $(y_i - z_i)$ plane, it can be observed that the width of the figure-eight trajectory is constant. Thus, keeping

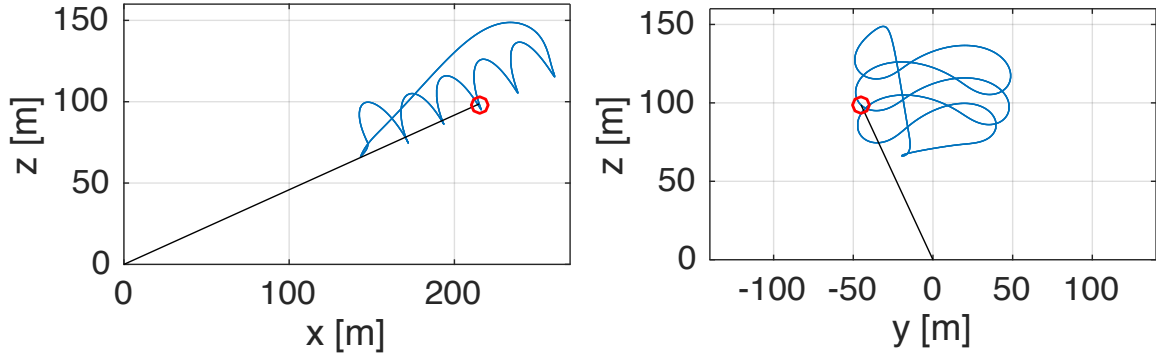


Figure 4.12: Trajectories of the Magnus rotor in $(x_i - z_i)$ and $(y_i - z_i)$ planes for 3 cycles.

the swept area constant for the whole production phase. Figure 4.15 presents a comparison between the swept area of the Magnus based AWE of surface area $500m^2$ with a conventional wind turbine of 1.5 MW.

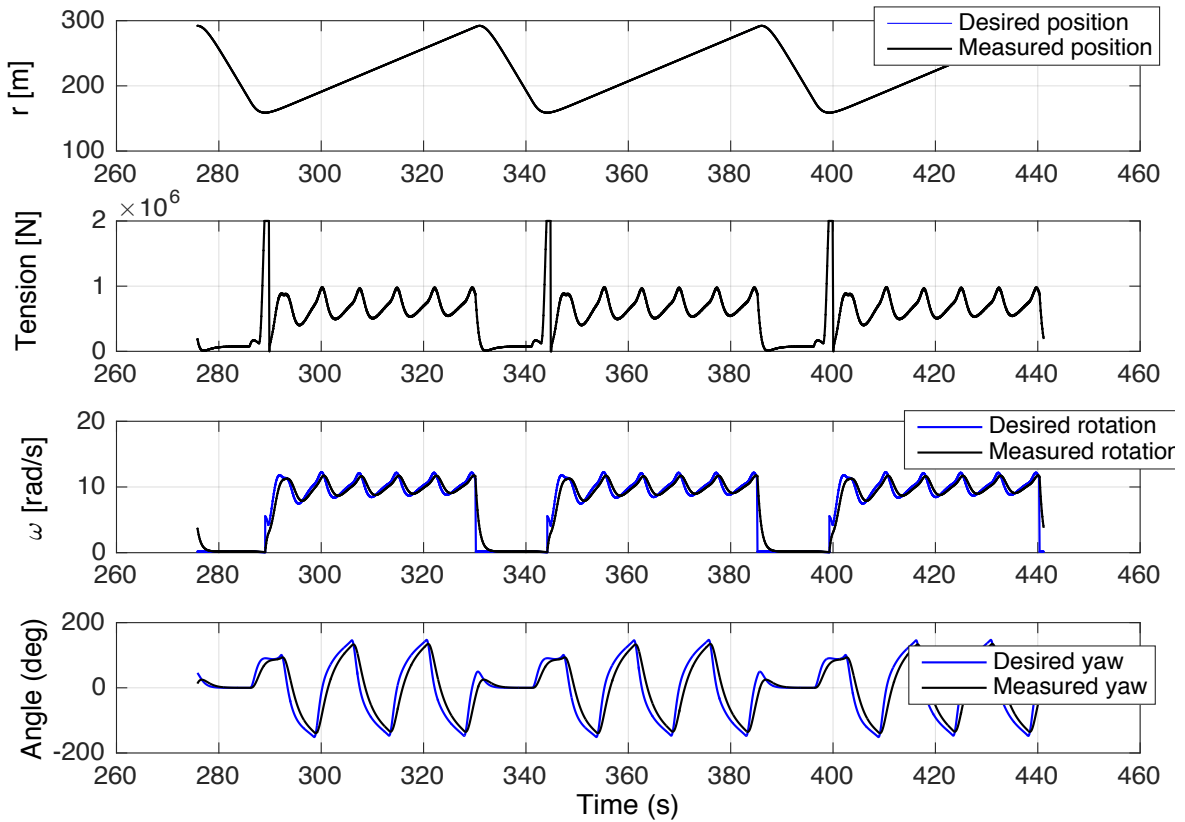


Figure 4.13: Reference and state variable for tether length $(r_t, r_{t_{ref}})$, tether tension F_r proportional to winch torque T_c , angular speed of the Magnus rotor $(\omega_{cyl}, \omega_{cyl_{ref}})$, and yaw angle (γ, γ_{ref}) , as function of time for the 3 cycles.

Figure 4.13 presents the main variables of the system. It can be seen that the tether length r_t overlaps perfectly with its reference due to the controller K_1 despite the saturation of the winch actuator. This saturation can be seen in the tether tension curve at the beginning of each production phase. From the evolution of speed of rotation curve it can be inferred that the system can follow the variations in the apparent wind speed by modifying its angular spin ω_{cyl} in order to keep the spin ratio $X = X_{max}$. Finally, the evolution of heading angle variables gives an insight into the control performance required to perform figure-eight trajectories with Magnus-based AWE system.

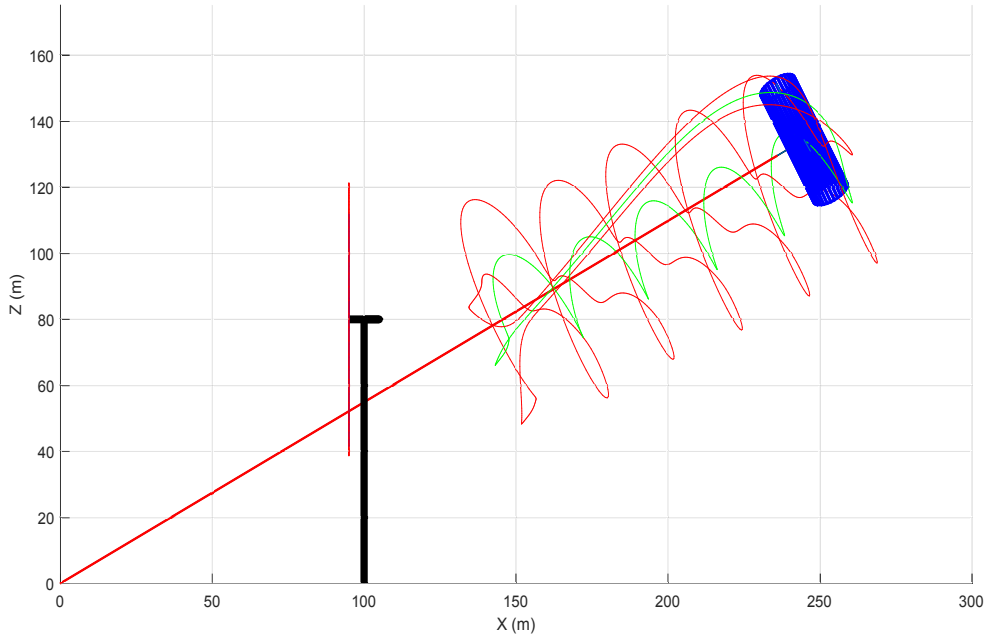


Figure 4.14: Eight figure crosswind trajectory of ABM in $(x_i - z_i)$ plane.

Figure 4.16 shows the evolution of output power P_g given by equation 4.111. It can be seen in the figure that the minimum value of the power P_g is -1.9 MW and the maximum is 3.9 MW. Therefore, the mean power for the full cycle comes out to be 1.47 MW. However, to obtain the net power, the power consumed by the embedded motor to spin the Magnus cylinder has to be subtracted, discussed further in chapter 5. But it is not considered in this study.

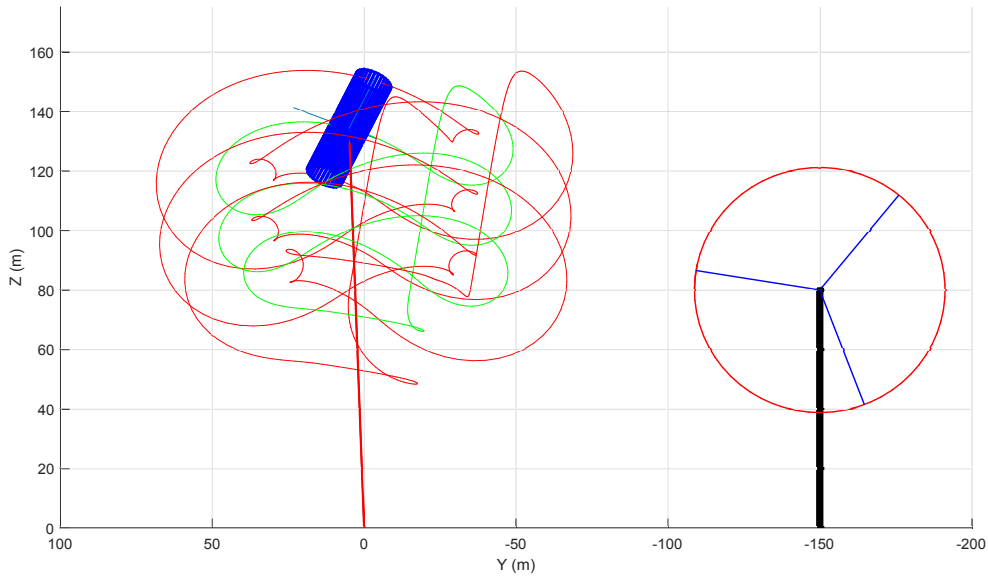


Figure 4.15: Swept area comparison of Magnus-based AWE and conventional wind turbine in $(y_i - z_i)$ plane.

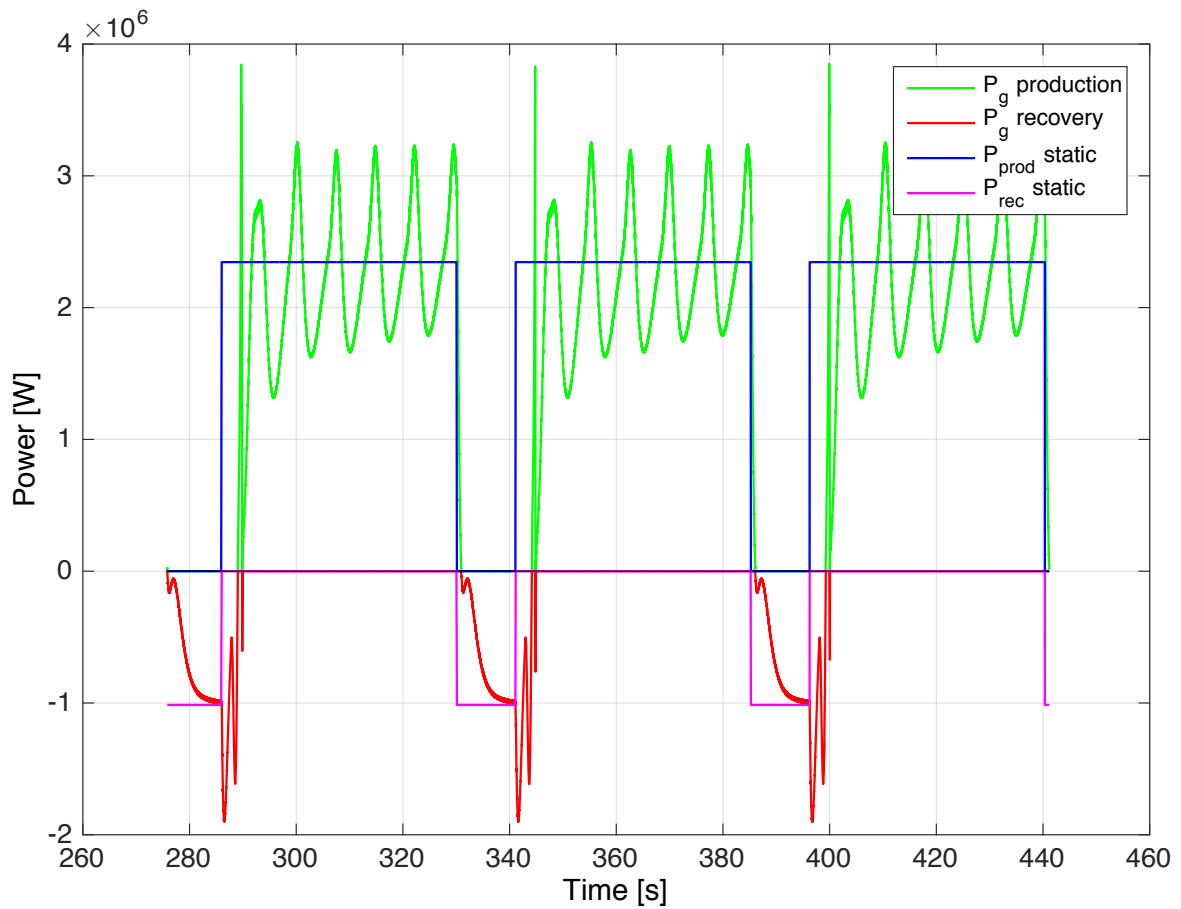


Figure 4.16: The output power simulated P_g during production and recovery phases for the 3 cycles with a comparison with the simplified model under the static assumption. The mean output power is 1469 kW for dynamic simulation and 1674 kW for the simplified model.

The figure 4.16 also presents the power output of the simplified model under static assumption as presented in section 4.5.1. It can be seen that the static power output is close to the mean output power P_g for the dynamically simulated system. The total mean power for the simplified model comes out to be $P_{cycle} = 1.67$ MW, which is only 14% more than the mean power output of the simulated system. Therefore, it can be inferred that for a Magnus-based AWE system with the specifications defined in table 4.1, in order to produce 1.5 MW nominal power at wind speed $10m/s$, the required generator must be able to produce minimum 4×10^6 Nm torque and have 6.6 rad/s of rotation speed. This leads to a generator with a capacity of 26.6 MW which would be very bulky as well as costly and, thus, elevating the cost of production.

Therefore, to prevent an escalation in the cost a trade-off has to be found to use a generator of reasonable capacity. This can be achieved by using novel power transmission techniques such as a two stage gearbox, generator linked to a motor or a hydraulic stage conversion discussed in detail in chapter 5. In case of a gearbox, the capacity of the required generator comes out to be 3.9 MW. As the gearbox can be used to increase the drum speed during the recovery phase as there is no need for high torque in this phase. Thus, the two extreme values are not required at the same time. Thus, decreasing the required capacity of the generator.

Finally, the maximum torque can be also limited to a much smaller value. However, in this case, a degradation of tether length control law will occur.

4.6 Conclusion

In this chapter, a 3-D model of Magnus effect-based AWE systems are discussed in detail taking into account both the translational and rotational dynamics of the system.

A bang-bang control strategy is discussed and simulation results for a $500 m^2$ Magnus-based AWE system are presented. It is assumed that the heading angle of the system is controllable and it has been shown that the Magnus effect-based AWE systems can perform crosswind figure-eight maneuver. The results of the static model have been found to be satisfactory and give results close to the performance of the 3-D dynamic simulation. This modeling approach can be adopted for any on-ground production AWE system.

Analysis of Power Curves for AWE Systems

Contents

5.1	Introduction	89
5.2	Modelling of Power Curves	91
5.2.1	Model of Wind Profile	91
5.2.2	Model of a Horizontal Axis Wind Turbine (HAWT)	91
5.2.3	Static Model of Ground-based AWE System	92
5.3	Ground Station Architecture	97
5.3.1	Ground Station Design Constraints	98
5.3.2	Output Power specific to Ground Station Design	100
5.4	Control and Optimization of Output Power	101
5.4.1	No saturation on actuators: Optimization of reel-in and reel-out speeds	102
5.4.2	Optimization of reel-in speed when reel-out speed is set	102
5.4.3	Optimization of reel-out speed when reel-in speed is set	103
5.4.4	Control of Output Power by Altitude Correction	103
5.4.5	Control of Output Power by Elevation (θ_T) or Azimuthal angle (ϕ_T) Correction	104
5.4.6	Summary of the High-Level Control Algorithm	104
5.5	Numerical Application	104
5.5.1	MW-size Systems	104
5.5.2	KW-size System	108
5.5.3	Discussion	112
5.6	Conclusion	114

5.1 Introduction

Power curves serve as a tool to analyze the economic feasibility of any type of wind turbine. In literature, there are many studies discussing the power curves of conventional wind turbines.

Over the years, the power curves have been validated and improved by incorporating the on-field data from the installed wind turbines. To evaluate the economic viability of airborne wind energy systems, and to draw valid comparisons with the conventional turbines, there is a need to develop accurate power curves for AWE systems, [127]. Currently, there are very few working prototypes of AWE systems and none of them is a fully functioning commercial unit. Thus, the power curves for AWE systems are still an open topic of discussion in the research community. In [128], a study is presented discussing the family of power curves for different altitudes derived from the fast model presented in [10]. The study also compares the power curves with the dynamic simulations of Enerkite AWE prototype EK30 and it concludes that the significant confidence can be placed on the approach presented in the work for estimating the power curves for AWE systems. In [129], a simplified model is analyzed to estimate the maximum feasible drag power for an on-board production system. In [130], an optimal control problem is discussed which is then used to obtain power curves for a rotary kite AWE system. In [122], a strategy to control the power production of a Magnus-based AWE system (by changing aerodynamic coefficients of the system) is proposed.

In the previous chapter 4, a 6-DOF mathematical model for the Magnus based AWE system is presented and validated by simulation (controlling the system in crosswind trajectories). A static model of the full cycle is presented and compared to the dynamic simulation. In this chapter, based on a static model proposed and validated in chapter 4, a structural analysis of ground station structure (including electrical and hydraulic solutions), and a generic static model of on-ground AWES is proposed, which can be applied to other kind of AWES such as kites, UAV's etc. A high-level algorithm is developed to maximize the net output power of the system, taking into consideration the necessary operational limitations of various sub-systems such as winch actuators, maximum permissible tether traction etc. This fast model is then used to calculate power curves for a generic AWE system (such as kite, UAV, Magnus etc.) as a function of different design parameters. As this thesis work is specifically based on Magnus-based on-ground AWE systems, numerical application for these type of systems is done to draw comparisons with conventional horizontal axis wind turbines. The 4 & 5-phase power curves calculated in this chapter give a valuable insight into the potential of AWE systems and expose some advantages over conventional wind turbines.

The chapter is organized as follows. Section 5.2 focuses on the modeling of the different parts of the system. In section 5.3, two type of ground station layout utilising gearbox and hydraulic stage are discussed. In section 5.4, control and optimization technique for the maximization of the output power is presented. A numerical application follows in section 5.5. The chapter ends with some conclusions in section 5.6.

5.2 Modelling of Power Curves

5.2.1 Model of Wind Profile

In this chapter, the wind profile power law is considered to describe the evolution of horizontal mean wind speed with altitude. This theoretical model is discussed in detail in literature [131] and provides a good approximation of the wind speed for altitudes between 100 to 2000 m. According to this model, the wind speed v_w at any altitude z can be given by:

$$v_w(z) = v_w(z_0) \left(\frac{z}{z_0} \right)^\alpha \quad (5.1)$$

Where, z_0 represents the operating altitude, $v_w(z_0)$ is the known wind speed at altitude z_0 , and α is an empirically derived coefficient that characterizes the surface. It depends on the stability of the atmosphere and is generally assumed to be equal to 0.143. To take into account the constant variation of the wind speed and to calculate the annual mean wind speed at a particular site, the well know Weibull distribution is used. The distribution basically tells at a particular site how often the wind blows and how strong it is. Thus, it is a good way to describe the wind speed variations and it is given by:

$$f(v_w) = \frac{k}{a} \left(\frac{v_w}{A} \right)^{k-1} e^{-\left(\frac{v_w}{A} \right)^k} \quad (5.2)$$

Where, $f(v_w)$ is a probability to have v_w wind speed over the year, A is the Weibull scale parameter expressed in m/s and is proportional to mean wind speed, and k is the Weibull form parameter describing the shape of the Weibull distribution with its value between 1 and 3. Smaller values of k show very variable winds while larger values show constant winds. Finally, v_w is the wind speed series whose probability distribution is calculated. Figure 5.1 shows an example of weibull distribution calculated for a series of wind speed measurements carried out over an year.

5.2.2 Model of a Horizontal Axis Wind Turbine (HAWT)

For conventional wind turbines, the power produced depends on the kinetic energy of the air and the power coefficient, C_p , of the turbine which is smaller than its theoretical Betz limit $\frac{16}{27}$.

$$P_{HAWT} = \frac{1}{2} \rho C_p A_{swept} v_w^3 \quad (5.3)$$

Where, A_{swept} is the total surface swept by the blades. Power produced, P_{HAWT} , is generally divided into four phases characterized by the design constraints of the system. The first phase is from zero wind speed to cut-in wind speed v_{ci} , where a conventional turbine does not produce any energy. The second phase is from v_{ci} to the nominal wind speed v_{nom} , where the maximum wind power extraction occurs by maximizing C_p coefficient. The third phase is from v_{nom} to the cut-off wind speed v_{co} , and during this phase power is curtailed to nominal power P_{nom} by reducing C_p coefficient. Finally, for any wind speed beyond v_{co} , the wind turbine is

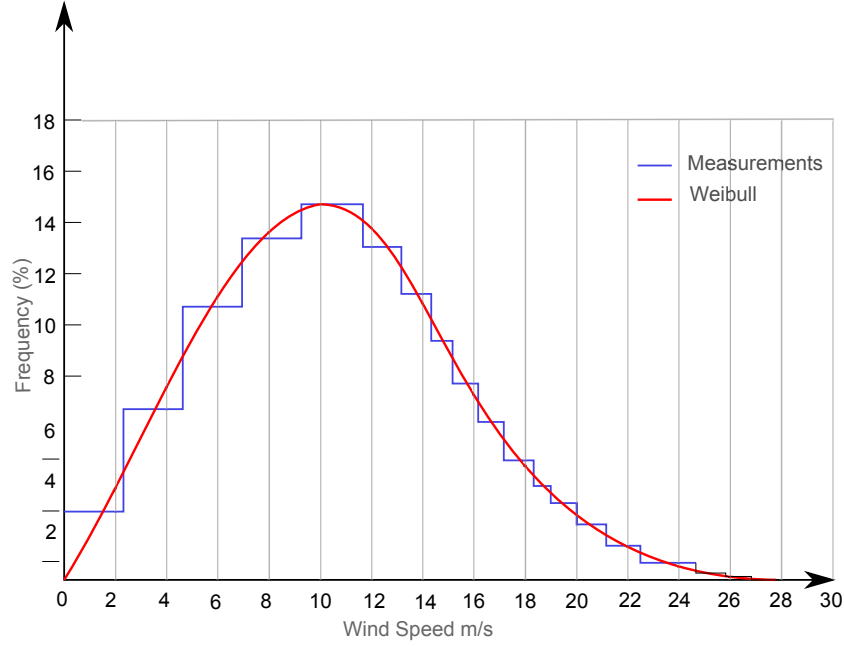


Figure 5.1: Weibull Distribution.

switched-off to avoid its mechanical and electrical degradation. Therefore, the power curves of a HAWT can be produced by the following set of equations:

$$P_{HAWT} = \begin{cases} \frac{1}{2}\rho C_{pmax} A_{swept} v_w^3 & \text{if } v_{ci} < v_w \leq v_{nom} \\ P_{nom} & \text{if } v_{nom} < v_w < v_{co} \\ 0 & \text{if } v_w \geq v_{co} \text{ or } v_w \leq v_{ci} \end{cases} \quad (5.4)$$

Figure 5.2 presents a classical power curve for a particular HAWT. As observed the from figure 5.2, the power curve consists of three phases, denoted as phase I, II, and III, each describing the operational constraints of HAWT as presented by equation 5.4.

5.2.3 Static Model of Ground-based AWE System

As stated in previous chapters, the operational cycle for any on-ground AWE system is divided into two phases, namely, the production phase and the recovery phase. In chapter 4, a static model is presented with section 4.5.1 presenting the simulated power produced. As stated in chapter 3, a part of the power produced during the production phase is consumed during the recovery phase. In order to minimize the energy consumption during this phase, the traction force has to be minimized.

As explained before in chapter 3, the aerodynamic lift and drag forces acting on any

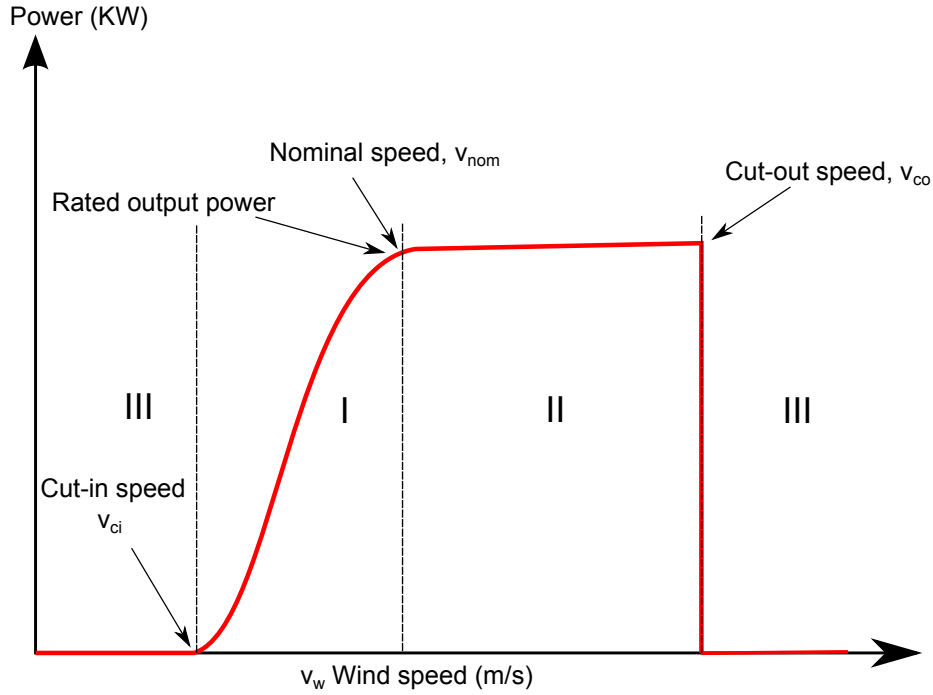


Figure 5.2: Power curve of a conventional wind turbine.

classical airborne platform can be expressed as:

$$L = \frac{1}{2}\rho S v_a^2 C_L, \quad D = \frac{1}{2}\rho S v_a^2 C_{Deq} \quad (5.5)$$

Where, C_{Deq} is the equivalent aerodynamic drag coefficient of the tether and any other structural components of the airborne platform. Note that C_{Deq} has to be expressed as a function of tether length to include any increment or decrement in the tether drag due to the winding or unwinding of the tether from the winch.

As discussed in the chapter 4, two frames of references are used to describe the motion of the Magnus based AWE system, inertial frame, (x_i, y_i, z_i) , and body frame (x_b, y_b, z_b) . It is assumed that the wind speed, v_w , as witnessed by the cylinder is in \vec{x}_i direction. Thus, the component of the wind speed, v_t , in the direction parallel to the tether is given by:

$$v_t = v_w \cos(\theta_T) \cos(\phi_T) \quad (5.6)$$

Where, θ_T and ϕ_T represents the elevation and the azimuthal angle of the tether with respect to the inertial frame. Figure 5.3 presents a 3D model of a Magnus-based AWE system described using two frames of references. The tether length r_t is calculated as:

$$r_t = \sqrt{x^2 + y^2 + z^2} \quad (5.7)$$

Where, (x, y, z) are the coordinates of C_g of the airborne platform in the inertial frame. In the static analysis presented in chapter 4, assuming straight taut tether, the traction force F_r developed in the tether is directly proportional to the resultant aerodynamic force acting

5.2.3.3 Magnus Motor consumption

As mentioned in chapter 3, section 3.3, in case of Magnus-based AWE systems a part of the power produced is also used to turn the Magnus rotor and it can be written as:

$$P_{rotor} = T_{motor}\omega_{cyl} \quad (5.14)$$

Where, T_{motor} is the on-board motor torque. To calculate the maximum theoretical power produced, the power consumed by the Magnus rotor is considered to be zero. However, it can be estimated as

$$T_{motor} = \frac{1}{2}\pi r_{cyl}^2 l_{cyl} v_a^2 C_m \quad (5.15)$$

Where, r_{cyl} is the radius of the Magnus cylinder, C_m is the torque coefficient of the rotor, l_{cyl} is the length of the Magnus cylinder. As the rotational speed of the Magnus cylinder depends on the non-dimensional quantity, spin ratio, X , expressed as:

$$X = \frac{\omega_{cyl} r_{cyl}}{v_a} \quad (5.16)$$

Thus, from equation 5.16 ω_{cyl} can be expressed as:

$$\omega_{cyl} = \frac{X v_a}{r_{cyl}} \quad (5.17)$$

Hence, the power consumed by the motor can be approximated as:

$$P_{motor} = T_{motor}\omega_{cyl} = \frac{1}{2} X r_{cyl} l_{cyl} v_a^3 C_{M_z} \quad (5.18)$$

5.2.3.4 Full Production Cycle

A given power cycle is thus defined by one complete production and recovery phase as shown in figure 5.4. The transitional phase between the production and the recovery phase is neglected in this formulation. The time for each phase can then be expressed as:

$$t_1 = \left| \frac{r_{max} - r_{min}}{\dot{r}_{prod}} \right| = \frac{\Delta r}{\dot{r}_{prod}} \quad (5.19)$$

$$t_2 = \left| \frac{r_{max} - r_{min}}{\dot{r}_{rec}} \right| = \frac{\Delta r}{\dot{r}_{rec}} \quad (5.20)$$

Where, t_1 and t_2 represent the duration of the production and recovery phase respectively. r_{max} and r_{min} represent the minimum and maximum tether length reached in the a particular operating cycle, Δr represents the absolute tether length for that particular phase. Note, here it is assumed that for a particular cycle during both the production as well as the recovery phase, the intial position is same. In other words, during the recovery phase the airborne platform is brought back to the same initial position .i.e. the position before the start of the production phase. Thus, the total time, t taken for one complete production cycle is:

$$t = t_1 + t_2 \quad (5.21)$$

The high level algorithm presented in figure (5.7) summarizes the optimization of all the considered variables.

5.4.1 No saturation on actuators: Optimization of reel-in and reel-out speeds

To maximize the net power production during one complete cycle, \dot{r}_{prod} and \dot{r}_{rec} have to be optimized simultaneously. In the considered optimization procedure, P_{cycle} is derived with respect to each \dot{r}_{rec} and \dot{r}_{prod} while considering the other variables as constant.

$$\frac{\partial P_{cycle}}{\partial \dot{r}_{rec}} = f(v_w, \dot{r}_{rec}, \dot{r}_{prod}, M) \quad (5.33)$$

While considering \dot{r}_{prod} , v_w and the vector of parameters M as constant. Vector M is given by:

$$M = [C_L, C_{Deq}, C_{Drec}, \phi_T, \theta_T, \eta_p, \eta_r, \eta_s, \eta_g, \rho, S] \quad (5.34)$$

Similarly,

$$\frac{\partial P_{cycle}}{\partial \dot{r}_{prod}} = f(v_w, \dot{r}_{rec}, \dot{r}_{prod}, M) \quad (5.35)$$

While considering this time that \dot{r}_{rec} as constant. The first order partial derivative results in a polynomial function, and solving the system of equation the optimal values of \dot{r}_{rec} and \dot{r}_{prod} can be obtained as:

$$\begin{cases} \dot{r}_{rec_{opt}} = f_s(v_w, \dot{r}_{prod}, M) \\ \dot{r}_{prod_{opt}} = g_s(v_w, \dot{r}_{rec}, M) \end{cases} \quad (5.36)$$

5.4.2 Optimization of reel-in speed when reel-out speed is set

As presented before, the power produced by an AWE system in production phase is given by:

$$P_{prod} = F_r \dot{r}_{prod} \quad (5.37)$$

Due to design and structural constraints, there exists an upper limit for traction force F_r denoted by F_{max} . This limit can be attributed to tether, winch and/or kite structural limitations. When this limit is reached during the production phase, and if $\cos(\theta_T) \cos(\phi_T)$ and $C_L(\frac{C_L}{C_{Deq}})^2$ are set at their maximum value, then \dot{r}_{prod} has to be set such that $F_r = F_{max}$. In this case, the optimal value of \dot{r}_{prod} can be calculated using equation (5.10) as:

$$\dot{r}_{prod_{opt}} = v_t - \sqrt{\frac{F_{max}}{\frac{1}{2}\rho S C_L (\frac{C_L}{C_{Deq}})^2}} \quad (5.38)$$

Where, $\dot{r}_{prod_{opt}}$ is the value of \dot{r}_{prod} which maintains $F_r = F_{max}$. In the case if \dot{r}_{prod} reaches $\dot{r}_{prod_{max}}$ then it has to be saturated while maintaining F_r equal to F_{max} . This can be done by reducing other parameters such as $\cos(\theta_T) \cos(\phi_T)$ or $C_L \left(\frac{C_L}{C_{Deq}}\right)^2$. Thus, in order to maximize

Kite parameters	Variable	Value
Span [m]	L	90
Radius [m]	R	9
Magnus Surface [m ²]	S	1620
Maximum $C_L \left(\frac{C_L}{C_{D_{eq}}} \right)^2$ for $X = 3.6$	$C_L \left(\frac{C_L}{C_{D_{eq}}} \right)^2$	69.44
Minimum drag coefficient	$C_{D_{rec}}$	0.5
Minimum elevation angle [deg]	θ_T	25
Cut-in wind speed [m/s]	V_{ci}	3
Cut-out wind speed [m/s]	V_{co}	22.5
Maximal traction force [kN]	F_{max}	2405
Maximal strength [N/m ²]	σ	1485
Working altitude [m]	z	160
Aspect ratio	AR	5
Reynolds number for $V_a = 10m/s$	Re	10.9e6

Case 1: Ground station with 2 electrical actuators

Electric generator nominal power [MW]	$P_{prod_{max}}$	10
Nominal Power for grid connection [MW]	P_{grid}	5.91
Electric motor nominal power [MW]	$P_{rec_{max}}$	5.56
Yield of generator	η_p	0.92
Yield of motor	η_r	0.88
Yield of storage device	η_s	1
Yield of grid connection	η_g	0.98
Maximal reel-in speed [m/s]	$\dot{r}_{rec_{max}}$	14.7
Maximal reel-out speed [m/s]	$\dot{r}_{prod_{max}}$	4.16

Case 2 : Ground station with hydraulic stage

Electric generator nominal power [MW]	P_{grid}	10.9
Hydraulic motor/pump nom. power [MW]	P_{max}	40
Yield of motor/Pump for production	η_p	0.92
Yield of motor/Pump for recovery	η_r	0.88
Yield of storage device	η_s	1
Yield of grid connection	η_g	0.98
Maximal reel-in and reel-out speed [m/s]	\dot{r}_{max}	16.65

Table 5.2: Parameters of the 90m span MGAWES.

P_{rec} increases as with an increase in the wind speed the drag also increases. Thus, more and more power is required to recover the airborne platform. This leads to a reduction in the net power output P_{cycle} as represented by dotted line in figures 5.8 and 5.9. Finally, solid lines in phase IV shows the use of elevation angle θ_T to maintain output power at its maximum by achieving the maximum permissible effective wind v_t .

In table 5.2, case 2 presents the case when there are no set limitations on the winch actuators. The parameters are chosen to illustrate hydraulic configuration and in this case both the phases use the same actuator. So, the winch actuator has to at least produce the high

force F_{max} and high speed $r_{rec_{max}}$ in the same time. This extends the phase III to maximum cut-out value v_{co} . The maximum output power is then produced at this maximum wind speed, and has to be used to size the grid connection P_{grid} . Note that the same power curve can be produced with a single 40MW electric motor/generator coupled with a single gearbox.

Using these theoretical power curves and wind distribution described in section 5.5.1.2, the theoretically expected energy produced during one year can be computed for HAWT V150 as well as for the same 90m span Magnus effect kite with different ground-station configurations.

Just for the sake of comparison, from figure 5.8 it can be noted that a generator and a motor that saturates at the same wind speed as HAWT (i.e. $P_{prod_{max}} = 6.7MW$ and $P_{rec_{max}} = 4MW$) will lead to a similar power curve and similar annual production. This configuration is considered as case 0.

Table 5.3 summarizes the different systems considered and associated size of actuators. It also gives the corresponding theoretical annual production and capacity factor, computed by dividing annual production by $8760P_{grid}$.

System	P_{Grid} [MW]	Generator [MW]	Motor [MW]	Annual prod. [GWh/year]	Capacity factor
Vestas V150	4.2	4.2	-	18.2	0.49
AWES Case 0	4.2	6.7	4	18.2	0.49
AWES Case 1	5.9	10	5.56	21.9	0.42
AWES Case 2	10.9	40	-	24.8	0.26

Table 5.3: Considered actuators configurations and corresponding theoretical annual production and capacity factor

5.5.2 KW-size System

As similar comparison is made for a KW-sized Magnus-based airborne wind energy systems with a HAWT of same size.

5.5.2.1 HAWT Parameters

In this section, a 12 kW pitch controlled horizontal axis wind turbine is considered, with the parameters detailed in table 5.4.

5.5.2.2 Wind Parameters

The evolution of wind with altitude as presented by equation (5.1) is used. Parameters used are $\alpha = 0.143$ and $z_0 = 10$ m, which is tower height of the considered HAWT. Similar to

Kite parameters	Variable	Value
Span [m]	L	6
Radius [m]	R	0.5
Magnus Surface [m ²]	S	6
Maximum $C_L \left(\frac{C_L}{C_{D_{eq}}} \right)^2$ for $X = 3.6$	$C_L \left(\frac{C_L}{C_{D_{eq}}} \right)^2$	69.44
Minimum drag coefficient	$C_{D_{rec}}$	0.5
Minimum elevation angle [deg]	θ_T	25
Cut-in wind speed [m/s]	V_{ci}	2
Cut-out wind speed [m/s]	V_{co}	24
Maximal traction force [kN]	F_{max}	3.96
Maximal strength [N/m ²]	σ	660
Working altitude [m]	z	10-100
Aspect ratio	AR	6
Reynolds number for $V_a = 10m/s$	Re	$6.61e5$

Case 1 : Ground station with 1 electrical actuators

Nominal Power for grid connection [kW]	P_{grid}	12
Electric motor/generator nom. power [kW]	P_{max}	43.9
Yield of motor/generator for production	η_p	0.92
Yield of motor/generator for recovery	η_r	0.88
Yield of storage device	η_s	1
Yield of grid connection	η_g	0.98
Maximal reel-in and reel-out speed [m/s]	\dot{r}_{max}	11.1

Case 2 : Ground station with hydraulic stage

Electric generator nominal power [kW]	P_{grid}	12
Hydraulic motor/pump nominal power [kW]	P_{max}	43.9
Yield of motor/Pump for production	η_p	0.92
Yield of motor/Pump for recovery	η_r	0.88
Yield of storage device	η_s	1
Yield of grid connection	η_g	0.98
Maximal reel-in and reel-out speed [m/s]	\dot{r}_{max}	11.1

Table 5.5: Parameters of the 6m span MGAWES.

output power, followed by the next phase using the elevation angle. One can note that phase II is greatly shortened, thereby lengthening phase III by starting it at a lower wind speed. This results in an MGAWES design for low wind speed sites by using the lower maximum strength parameter σ .

Moreover, during phases II and III, energy is harvested at an altitude of 100 m instead of 10 m. Also, the wind model shifts the wind by about 2 m/s, thus, shifting the power curve to the left, as depicted by the solid line in figure 5.10. Table 5.6 summarizes theoretical annual production and capacity factor, computed by dividing annual production by $8760P_{grid}$ for the considered kW-sized HAWT and MGAWES.

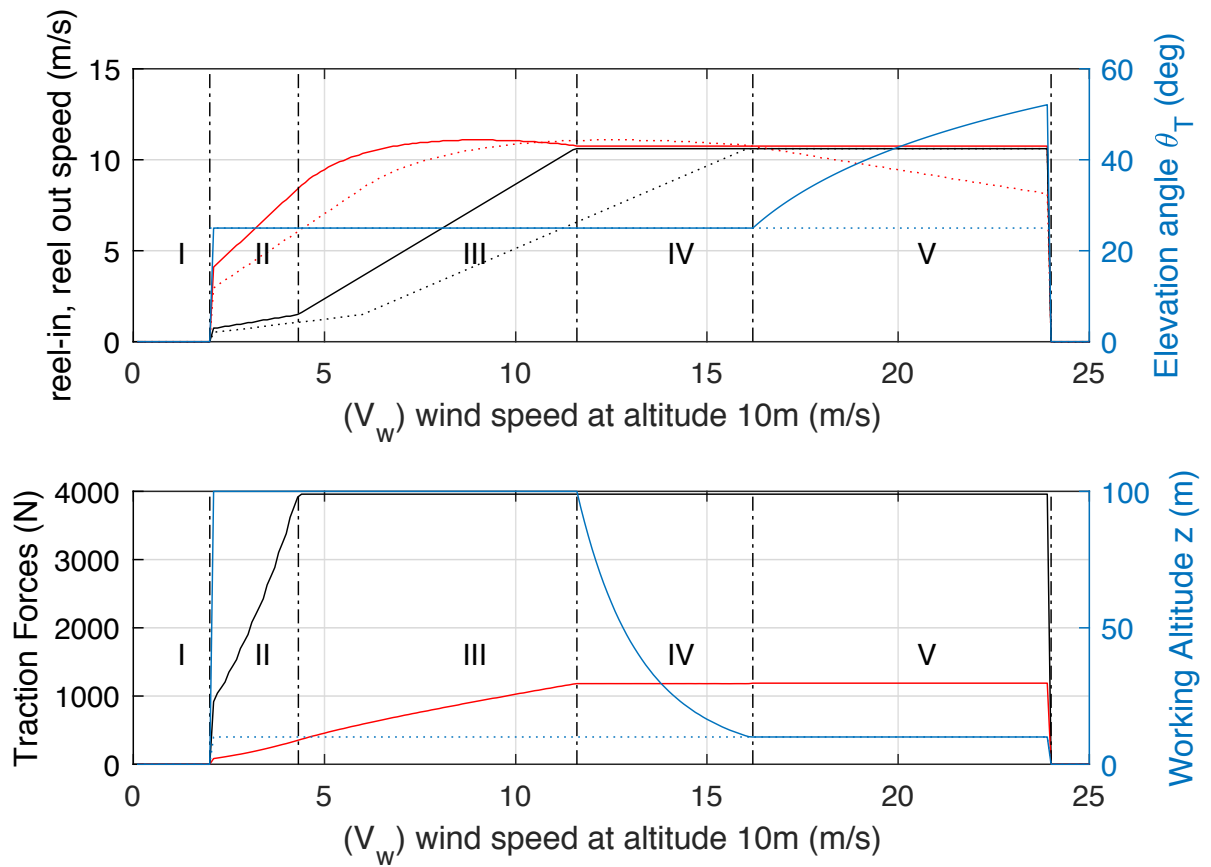


Figure 5.11: High-level control variables for 6m span MGAWES. Top: reel-out speed during production phase (black) and reel-in speed during the recovery phase (red) in function of wind speed. Down: Traction force during production (black) and recovery (red) phases. The dotted line represents variables when the kite stays at altitude 10m and control of elevation angle is not used

system. The power curves with its saturation's can be used to design a system as a function of its size and the wind distribution at the considered site.

AWE systems need fewer materials than an equivalent HAWT because there is no need of a tower and associated concrete foundation, but in some considered configurations, the ground station needs an electrical generator 3 to 4 times the nominal power of the system. The use of hydraulic stage seems to be a good alternative to this costly electric actuator over-sizing problem. But it has to be studied in detail in terms of yield and controllability. The five phases are shown in figure 5.10 illustrate the flexibility of on-ground AWES due to the higher number of control variables in comparison to the conventional wind turbines. This gives AWE systems the capacity to operate on a wide range of wind speed, and thus, can be designed for low wind speed operation as well.

Unlike the conventional wind turbines for AWES one can easily dissociate the maximum stress forces that the system can withstand and the maximum electric power of the generator.

For instance, the kite can be designed for low traction force, which will reduce its cost, and reduce the width of phase II. Then phase III can be extended by oversizing the actuators. This will also define the nominal output power which the system must respect for the remaining zone of the power curve, in order to produce the flat zone. In another scenario, one can design very short phase II and III, leading to lower cost, and wide phase IV and a flat zone in phase V. This leads to a production that will be more stable and easier to forecast by grid operators.

Moreover, theoretically, the power produced can be coupled with a high-level energy control algorithm (like the one presented in [123]) to make energy produced controllable by grid operators, from 0 to the maximum possible value at the current wind speed almost in real time.

Finally, numerical results on Magnus-based AWE system has to be seen in relation to that of other such systems. As some parameters used are theoretical and not verified experimentally in the same conditions. Also, the energy consumed by the motor as detailed in chapter 3 that is required to rotate the Magnus cylinder during the production phase can affect the global performance which for the sake of simplicity is not considered here. It is important to note that the approach presented can be used to obtain the same kind of results for any other on-ground AWES as the only change will be in the parameters $C_L \left(\frac{C_L}{C_{Deq}} \right)^2$, C_{Drec} and in some cases the static model of the recovery phase.

Also, the high-level algorithm presented can also be applied to any other On-ground AWE system resulting in power curves with the same 5 phases depicting the same behavior as presented by power curves calculated in this work.

5.6 Conclusion

In this chapter, the proposed static model represents a simple tool that can be used to predict the performance of the on-ground AWES in relation to the main design parameters. The proposed algorithm gives a strategy to maximize the energy produced by this kind of system for different configurations of actuator saturation under the static assumption. By coupling the static model with the high-level algorithm, a way to calculate power curves is presented. This approach is used to study the effects of design parameters on performances and can be used directly to control a system in real-time. The resulting power curves consist of 5 different phases where each phase corresponds to different control variables and illustrates the high flexibility of the on-ground airborne wind energy system. By adjusting different relative values of mechanical or electrical design parameters, one can easily adjust the 5 different modes in order to design the power curve for a specific zone with better-adapted shape. In particular, the beginning of phase III is directly linked to the maximum traction force developed in the kite and the tether. The end of this phase is defined by the saturation of the winch's power generator. The strategy presented can be used to evaluate other types of AWE systems and draw some valid comparisons with conventional wind turbines.

General Conclusions

6.1 Conclusions

Airborne Wind Energy is undergoing a rapid phase of development with more and more research groups taking up the challenges and proposing solutions to them. In this thesis work the main challenges that have been addressed are:

- Modelling and design of AWE systems,
- Autonomous operation of AWE systems,
- Ground station layout and configurations,
- Economic capability of AWE systems.

The main contributions of this work are:

1. **Study and validation of the aerodynamic model of the Magnus Effect:** In chapter 3, a two-step approach has been discussed with the aim of understanding the aerodynamic behavior of the Magnus effect and proposing a good aerodynamic model.

The approach has reconfirmed the high lifting potential of the Magnus effect. In the first step of the approach, the historical analysis of the experimental results on the Magnus effect presented some interesting insight into the lifting and drag capabilities of Magnus cylinder.

The second step, the EKF approach established the experimental results from the in-house experiments conducted at Gipsa-lab are in line with the previous results and further validates the theoretical model proposed in the literature.

The analysis also indicates an improved aerodynamic model for the Magnus effect is required in order to capture the phenomenon all the subtleties of the Magnus effect, particularly for the drag of the system.

2. **Development of a 3-D Mathematical model for Magnus-based AWE system:** In chapter 4, a 3-D modeling approach has been discussed. The 3-D model derived from the first principles of flight dynamics takes into account all the forces and moments acting on the Magnus-based AWE systems. The proposed model is based on the widely accepted approach in the aeronautics community. The proposed model incorporates

all the resulting effects which could be explored further in detail and coupled with the experimental data will provide an in-depth analysis of the dynamics of Magnus-based airborne wind energy systems. Hence, it can be considered as the base model for all the further future analysis.

3. **Design of guidance control for Magnus-based AWE system:** Chapter 4 also presents results obtained from the dynamic simulation of a Magnus-based AWE system. The guidance algorithm adopted in this work, and the obtained simulation results prove that a Magnus-based AWE system can successfully follow crosswind maneuvers provided that all the required control surfaces are suitably designed and incorporated in the prototype of MGAWES. Also, the proposed control strategy utilizing the tether length and spin ratio of the system has proved to meet all the objectives.
4. **Study of operational strategies for maximum power production by an AWE system:** In chapter 5, the power generation capabilities of AWE systems with an emphasis on Magnus-based AWE system is presented. The analysis based on the static model and the proposed expressions for mean power for one complete cycle presents a very useful approach towards the power generation analysis of such systems.

An optimization approach is presented to obtain the maximum mean power from one complete cycle of operation. The optimization strategy provides important insights into the optimal reel-in and reel-out speed of the tether from the winch and the actuator limitations that would be needed to be addressed in order to have an optimal power generation.

Based on this optimization approach, a higher level algorithm is also presented which takes into account the different saturations arising from the structural and functional limitations of AWE energy. Thus, the numerical results obtained for a targeted AWE system, provide some interesting insights into the power generation capabilities of the AWE system.

Also, based on these results, two set of configurations for a ground station have been discussed including a hydraulic stage in order to have a cost-effective AWE system.

5. **Development of the power curves for Magnus-based AWE systems:** The chapter 5 also proposes power curves for AWE system with a special focus on Magnus-based AWE systems. Following power curves of conventional wind turbines, power curves with 4 and 5 phases are proposed. The analytical approach utilizing the optimization of reel-in and reel- out speeds as well as different ground station configurations, provides a tool to evaluate the performance of AWE systems in general. Also, the proposed power curves enable a valid comparison between the conventional wind turbines. This marks a step towards the economic analysis of the AWE systems.

6.2 Perspectives

There are many issues which must be addressed before a fully automated 24x7 operational flight for AWE systems can be achieved. This thesis work tried to tackle some of the challenges

with a focus on Magnus-based AWE systems. But still, a lot needs to be done, in particular for Magnus-based wind energy systems. Directly, as a result of this thesis work some problems that must be addressed in future research work are:

1. **Aerodynamic model for Magnus effect:** Further analysis of Magnus effect should be undertaken, especially extensive wind tunnel testing or CFD analysis, to develop an accurate aerodynamic model for Magnus effect.
2. **Analysis of Moments acting on Magnus cylinder:** A thorough analysis of the aerodynamic moments affecting the Magnus cylinder must be undertaken supplemented with the wind tunnel testing. In order to establish the occurrence and effect of some of the well known aerodynamic phenomenon which affects the classical airfoils such as the weathercock effect, etc. Also, the phenomenon of drag crisis particular to the Magnus effect and its effect on the aerodynamic moments must be explored in the future analysis. In addition, from the experiments, the value of various moments acting on the Magnus cylinder must be determined in order to decide whether they can be neglected or not.
3. **Decision on control surfaces for Magnus-based AWE systems:** In this work the use of horizontal tailplane (HTP) for the prototype has been disregarded. The self-stabilization characteristic and tether traction are assumed as the controlling input. In the future work, the use of HTP must be fully explored.
4. **Ground station layout:** A ground station using a hydraulic stage has been proposed in this work. In the future work, the capabilities and the controllability of the hydraulic stage must be studied in detail to establish the expected advantages of this stage.
5. **Power curves for Magnus-based AWE system:** A 5 stage power has been proposed based on the static model. In order to improve the power curve and to have a better estimate of the mean power generated. The model must be refined taking into account other contributions to the proposed power expression such as the effect of centrifugal forces, efficiency of the drivetrain and other devices used in the ground station.
6. **Landing and Take-off strategy:** The landing and take-off strategy is an open question in the AWE research community. The landing & take-off strategy for Magnus-based AWE systems needs to be devised. Also, its effect on the performance must be studied in detail for evaluating the power generation capabilities of Magnus-based AWE systems.
7. **Other design aspects:** Several design aspects from the engineering point of view must be investigated for the future development of the Magnus-based AWE systems. These include: the onboard energy supply aspect, structural design, tether bridle design, safety aspects and system redundancy. As these aspects will have considerable effect on the system complexity, hence, the cost. Therefore, they must be studied in detail.
8. **Test flights:** To better evaluate the behavior of the Magnus-based AWE systems extensive testing with full-size to mid-size prototypes must be done in order to refine the model, support further analysis and collect more data on the working of Magnus-based AWE systems.

The author of this thesis believes that the EOFLY research group at Gipsa-lab is fully capable and motivated to tackle these issues in detail in future. It is author's belief the future Ph.D. students as well as the post-doctoral students along with the researchers at Gipsa-lab would contribute immensely to the development of Airborne Wind Energy Systems.

Publications

International Conferences

1. Yashank Gupta, Jonathan Dumon, and Ahmad Hably, “*Modeling and control of a magnus effect-based airborne wind energy system in crosswind maneuvers*”, in The 20th World Congress of the International Federation of Automatic Control, 2017, Toulouse, France, [119].
2. Eduardo Schmidt, Yashank Gupta, Jonathan Dumon, and Ahmad Hably, “*In-flight estimation of the aerodynamic characteristics of a Magnuseffect-based AWE system*”, in the Renewable Energy for Developing Countries, 2018, Beirut, Lebanon, [136].
3. Yashank Gupta, Jonathan Dumon, and Ahmad Hably, “*Power Curve Analysis Of On-ground Airborne Wind Energy Systems*”, in ICIT,2019, 20th IEEE- International Conference of Industrial Technology, Melbourne, Australia, [137].

Abstracts

1. Yashank Gupta, Jonathan Dumon, and Ahmad Hably, “*Modeling and control of Magnus effect-based AWE systems*”, 7th International Airborne Wind Energy Conference, October 2017, Freiburg, Germany.

Posters

1. Yashank Gupta, Jonathan Dumon, and Ahmad Hably, “*Magnus-based Airborne Wind Energy Systems*”, 7th International Airborne Wind Energy Conference, October 2017, Freiburg, Germany.

Appendix A

- **LCOE:** The levelized cost of energy (LCOE) is a measure of a power source which allows to compare different methods of electricity generation on a consistent basis. It is an economic assessment of the average total cost to build and operate a power-generating asset over its lifetime divided by the total energy output of the asset over that lifetime. The LCOE can also be regarded as the average minimum price at which electricity must be sold in order to break-even over the lifetime of the project (definition from wikipedia).
- **Capacity Factor:** The net capacity factor is the unitless ratio of an actual electrical energy output over a given period of time to the maximum possible electrical energy output over that period.[1] The capacity factor is defined for any electricity producing installation, such as a fuel consuming power plant or one using renewable energy, such as wind or the sun. The average capacity factor can also be defined for any class of such installations, and can be used to compare different types of electricity production (definition from wikipedia).

Bibliography

- [1] . [Online]. Available: https://en.wikipedia.org/wiki/United_Nations_Framework_Convention_on_Climate_Change (cit. on p. 1).
- [2] “Unccc”, [Online]. Available: https://en.wikipedia.org/wiki/Kyoto_Protocol (cit. on p. 1).
- [3] “Unccc”, [Online]. Available: https://en.wikipedia.org/wiki/Paris_Agreement (cit. on p. 1).
- [4] “Unccc”, [Online]. Available: https://en.wikipedia.org/wiki/Bali_Road_Map (cit. on p. 2).
- [5] “Unccc”, [Online]. Available: https://en.wikipedia.org/wiki/Copenhagen_Accord (cit. on p. 2).
- [6] “Unccc”, [Online]. Available: https://en.wikipedia.org/wiki/2010_United_Nations_Climate_Change_Conference (cit. on p. 2).
- [7] “Unccc”, [Online]. Available: https://en.wikipedia.org/wiki/2011_United_Nations_Climate_Change_Conference (cit. on p. 2).
- [8] “Global survey of renewables 2018”, [Online]. Available: http://www.ren21.net/wp-content/uploads/2018/06/17-8652_GSR2018_FullReport_web_final_.pdf (cit. on p. 2).
- [9] “International energy agency”, [Online]. Available: [http://publications.jrc.ec.europa.eu/repository/bitstream/JRC107944/kjna28798enn\(1\).pdf](http://publications.jrc.ec.europa.eu/repository/bitstream/JRC107944/kjna28798enn(1).pdf) (cit. on p. 2).
- [10] M. L. Loyd, “Crosswind kite power”, *Journal of Energy*, vol. 4, no. 3, pp. 106–111, 1980 (cit. on pp. 3, 8, 17, 21, 25, 61, 82, 90, 94).
- [11] M. Corongiu, “Hawe ip rights ownership world overview”, 2014 (cit. on p. 3).
- [12] B. Franklin, “The kite experiment”, <http://franklinpapers.org/franklin/framedvolumes.jsp?vol=4page=3> *The Pennsylvania Gazette*, vol. 4, 360a, 1752 (cit. on p. 7).
- [13] G. Pocock, *The Aeropleustic Art or Navigation in the Air by the use of Kites, or Buoyant Sails*. 1827 (cit. on p. 8).
- [14] P. Payne and C. McCutchen, *Self-erecting windmill*, US Patent 3,987,987, 1976. [Online]. Available: <https://www.google.com/patents/US3987987> (cit. on p. 8).
- [15] “Bryant roberts”, [Online]. Available: <http://news.bbc.co.uk/2/hi/science/nature/1248068.stm> (cit. on p. 8).
- [16] W. Ockels, ““laddermill, a novel concept to exploit the energy in the airspace””, *Aircraft design*, vol. 4, 81–97, 2001 (cit. on pp. 8, 9, 13, 14).
- [17] Makani-Power, “<https://www.solveforx.com/makani/>”, 2016 (cit. on pp. 9, 10, 12, 13, 17, 18, 28).
- [18] “Windlift”, [Online]. Available: <http://windlift.com/> (cit. on p. 9).

- [19] NTS, 2015. [Online]. Available: <https://www.x-wind.de/index.php/en/> (cit. on pp. 9, 10).
- [20] kitegen, 2015. [Online]. Available: <http://www.kitegen.com/en/> (cit. on pp. 9, 10, 15, 28).
- [21] *Twingtec*. [Online]. Available: <http://twingtec.ch> (cit. on pp. 9–11).
- [22] awesco, 2015. [Online]. Available: <http://www.awesco.eu/> (cit. on p. 9).
- [23] ampyx. [Online]. Available: <https://www.ampyxpower.com/> (cit. on pp. 9, 10, 17–19).
- [24] Enerkite, “[Http://www.enerkite.de/en/products](http://www.enerkite.de/en/products)”, 2016 (cit. on pp. 9, 10, 16).
- [25] Omnidea, “[Http://www.omnidea.net/hawe/](http://www.omnidea.net/hawe/)”, 2013 (cit. on pp. 9, 10, 19, 20, 31).
- [26] H2020. [Online]. Available: <http://ec.europa.eu/research/energy/index.cfm?pg=home> (cit. on p. 9).
- [27] R. Schmehl, *Airborne Wind Energy Advances in Technology Development and Research Editors: Schmehl, Roland (Ed.)* 2018 (cit. on p. 10).
- [28] skysails. [Online]. Available: <http://www.skysails.info/> (cit. on pp. 10, 14, 15).
- [29] *Kitepower*. [Online]. Available: <http://www.kitepower.eu/> (cit. on pp. 10, 15, 16).
- [30] Magenn, [Http://www.magenn.com/](http://www.magenn.com/), 2012 (cit. on p. 10).
- [31] Altaeros, [Http://www.altaiosenergies.com](http://www.altaiosenergies.com), 2015 (cit. on pp. 10, 12, 18, 19).
- [32] A. Cherubini, *Dual drone project*. [Online]. Available: <http://www.antonellocherubini.com> (cit. on pp. 10, 20).
- [33] A. Cherubini, A. Papini, R. Vertechy, and M. Fontana, “Airborne wind energy systems: A review of the technologies”, *Renewable and Sustainable Energy Reviews*, vol. 51, pp. 1461–1476, 2015 (cit. on pp. 13, 14, 17).
- [34] L. Fagiano, A. U. Zraggen, M. Morari, and M. Khammash, “Automatic crosswind flight of tethered wings for airborne wind energy: modeling, control design and experimental results”, *IEEE Transactions on Control System Technology*, vol. 22, no. 4, pp. 1433–1447, 2014 (cit. on pp. 13, 21, 22, 58, 61, 77, 79).
- [35] *Kitepower bv*. [Online]. Available: <https://kitepower.nl/> (cit. on p. 15).
- [36] “Awesco”, [Online]. Available: <http://www.awesco.eu/alufr.html> (cit. on p. 15).
- [37] “Enerkite”, [Online]. Available: <http://www.enerkite.de/en/products> (cit. on p. 16).
- [38] bladetip. [Online]. Available: <http://bladetipsenergy.com/index.php> (cit. on p. 20).
- [39] Windfisher. [Online]. Available: <http://www.wind-fisher.com/> (cit. on p. 20).
- [40] B. Lansdorp, “The laddermill - innovative wind energy from high altitudes in holland and australia,windpower 06,adelaide,australia”, 2006. [Online]. Available: [uuid:9ebe67f0-5b2a-4b99-8a3d-dbe758e53022](http://www.windpower06.com/australia) (cit. on p. 21).
- [41] B. L. Paul Williams and W. Ockesl, “Optimal crosswind towing and power generation with tethered kites”, journal of guidance, control, and dynamics”, *Journal of Guidance, Control, and Dynamics*, vol. 31, pp. 81–93, 2006. [Online]. Available: <https://arc.aiaa.org/doi/10.2514/1.30089> (cit. on p. 21).

- [42] D. S. P. Williams and P. Trivailo, “Constrained path-planning for an aerial- towed cable system”, *Aerospace Science and Technology*, vol. 5, pp. 347–354, 2008. [Online]. Available: <https://doi.org/10.2514/1.C031108> (cit. on pp. 21, 23).
- [43] R. S. E. J. Terink J. Breukels and W. J. Ockels, “Flight dynamics and stability of a tethered inflatable kiteplane”, *Journal of Aircraft*, vol. 48, pp. 503–513, 2011. [Online]. Available: <https://doi.org/10.2514/1.C031108> (cit. on p. 21).
- [44] P. Rautakorpi, “Mathematical modeling of kite generators”, 2013. [Online]. Available: <http://URN.fi/URN:NBN:fi:tty-201312201529> (cit. on pp. 21, 23).
- [45] H. Li, D. J. Olinger, and M. A. Demetriou, “Attitude tracking control of an airborne wind energy system”, in *2015 European Control Conference (ECC)*, 2015, pp. 1510–1515 (cit. on p. 21).
- [46] H. Li, D. J. Olinger, and M. A. Demetriou, “Attitude tracking control of a groundgen airborne wind energy system”, in *2016 American Control Conference (ACC)*, 2016, pp. 4095–4100 (cit. on p. 21).
- [47] S. S. Ruitkamp R., *Description and Preliminary Test Results of a Six Degrees of Freedom Rigid Wing Pumping System*. 2013 (cit. on p. 21).
- [48] C. Jehle and R. Schmehl, “Applied tracking control for kite power systems”, *JOURNAL OF GUIDANCE, CONTROL, AND DYNAMICS*, vol. 37, no. 4, 2014 (cit. on pp. 21, 22, 61).
- [49] H. S. Michael Erhard, “Control of towing kites for seagoing vessels”, 2012. [Online]. Available: <https://arxiv.org/abs/1202.3641> (cit. on p. 21).
- [50] M. Milutinović, M. Corić, and J. Deur, “Operating cycle optimization for a magnus effect-based airborne wind energy system”, *Energy Conversion and Management*, vol. 90, pp. 154–165, 2015 (cit. on pp. 21, 24, 31, 44–47, 54, 55, 58, 106, 109).
- [51] L. Perković, P. Silva, M. Ban, N. Kranjčević, and N. Duić, “Harvesting high altitude wind energy for power production: The concept based on magnus’ effect”, *Applied Energy*, vol. 101, pp. 151–160, 2013 (cit. on pp. 21, 31, 40, 41).
- [52] A. Hably, J. Dumon, and G. Smith, “Control of an airborne wind energy system with a magnus effect”, in *The 2016 American Control Conference*, Boston, United States, Jul. 2016. [Online]. Available: <https://hal.archives-ouvertes.fr/hal-01272253> (cit. on pp. 21, 31, 58, 59).
- [53] P. J. Y. B. Cadalen F. Griffon, “Modelling and control of a tethered kite in dynamic flight”, 2017 (cit. on p. 22).
- [54] L. Fagiano and Milanese, “Control of tethered airfoils for high-altitude wind energy generation - advanced control methods as key technologies for a breakthrough in renewable energy generation [doctoral dissertation]”, 2012. [Online]. Available: <http://hdl.handle.net/11311/1006424> (cit. on p. 22).
- [55] M. Milutinović, N. Kranjčević, and J. Deur, “Multi-mass dynamic model of a variable-length tether used in a high altitude wind energy system”, *Energy Conversion and Management*, vol. 87, pp. 1141–1150, 2014 (cit. on pp. 23, 24).

- [56] S. A. J. Krenciszek and H. Braun, "Mathematical modeling of the pumping kite wind generator: Optimization of the power output", [Online]. Available: <http://www.win.tue.nl/casa/meetings/special/ecmi08/pumping-kite.pdf>, 2008. (cit. on p. 22).
- [57] J. Breukels and W. Ockels, "A multi-body dynamics approach to a cable simulation for kites", 2007 (cit. on p. 23).
- [58] B. L. P. Williams and W. Ockels, "Modeling and control of a kite on a variable length exible inelastic tether, aiaa guidance, navigation and control conference, south carolina, usa", 2007 (cit. on pp. 23, 61).
- [59] J Breukels, "An engineering methodology for kite design", 2011 (cit. on p. 23).
- [60] U. Fechner, R. van der Vlugt, E. Schreuder, and R. Schmehl", "'dynamic model of a pumping kite power system'", *"Renewable Energy"*, vol. "83", "705 –716", "2015". [Online]. Available: "<http://www.sciencedirect.com/science/article/pii/S0960148115003080>" (cit. on p. 23).
- [61] I. Aziz, "Design of a high altitude wind power generation system", Linköping University, Machine Design, 2013, p. 54 (cit. on pp. 24, 25).
- [62] U. Fechner and R. Schmehl, *Fechner U., Schmehl R. (2013) Model-Based Efficiency Analysis of Wind Power Conversion by a Pumping Kite Power System. In: Ahrens U., Diehl M., Schmehl R. (eds) Airborne Wind Energy. Green Energy and Technology. Springer, Berlin, Heidelberg.* 2016 (cit. on p. 24).
- [63] "Uwe fechner, roland schmehl, downscaling of airborne wind energy systems", *Journal of Physics: Conference Series*, vol. 753, no. 10, p. 102 002, 2016. [Online]. Available: <http://stacks.iop.org/1742-6596/753/i=10/a=102002> (cit. on p. 24).
- [64] H. Polinder, F. F. A. van der Pijl, G.-J. de Vilder, and P. J. Tavner, "Comparison of direct-drive and geared generator concepts for wind turbines.", *IEEE transactions on energy conversion.*, vol. 21, no. 3, pp. 725–733, 2006. [Online]. Available: <http://dro.dur.ac.uk/6704/> (cit. on p. 24).
- [65] M. Scholkopf, "Design of a ground station for a kite power system.", 2011 (cit. on p. 24).
- [66] P. Faggiani, "Pumping kites wind farm", 2014 (cit. on p. 24).
- [67] L. Fagiano and S. Schnez", "'on the take-off of airborne wind energy systems based on rigid wings'", *"Renewable Energy"*, vol. "107", "473 –488", "2017". [Online]. Available: "<http://www.sciencedirect.com/science/article/pii/S0960148117301015>" (cit. on p. 28).
- [68] R. S. M. F. Antonello Cherubini Balazs Szalai, "'preliminary test on automatic take-off and landing of a multi-drone low-drag airborne wind energy system,airborne wind energy conference 2017 (awec 2017)'"", [Online]. Available: "[uuid:f91403d6-6244-42ec-9aa0-14f843d5688a](http://www.sciencedirect.com/science/article/pii/S0960148117301015)" (cit. on p. 28).
- [69] R. B. E. B. S. Sieberling R. Ruiterkamp, "Discussion of a rotating platform for takeoff and landing of a tethered aircraft,airborne wind energy conference 2017 (awec 2017)", [Online]. Available: [uuid:c8219157-c909-4380-9fca-23a1e1f786de](http://www.sciencedirect.com/science/article/pii/S0960148117301015)" (cit. on p. 28).
- [70] K. Geebelen, "Design and operation of airborne wind energy systems" (cit. on p. 28).

- [71] J. Breukels, "Kite launch using an aerostat", [Online]. Available: [uuid:1a0c6dfd-6115-461f-ac04-bd8751efd6fb](#) (cit. on p. 28).
- [72] U. F. A. d. W. W. O. R. Schmehl R. van der Vlugt, "'airborne wind energy system". dutch patent application nl 2009528. pp. 1-34, 2014", [Online]. Available: <http://www.kitepower.eu/images/stories/publications/NL2009528C.pdf> (cit. on p. 28).
- [73] J. W. Kolar, "Conceptualization and multi-objective optimization of the electric system of an airborne wind turbine", [Online]. Available: https://www.pes-publications.ee.ethz.ch/uploads/tx_ethpublications/12_Conceptualization_Multi-Objective_ISIE2011.pdf (cit. on p. 28).
- [74] R. J. M. Penedo, T. C. D. Pardal, P. M. M. S. Silva, N. M. Fernandes, and T. R. C. Fernandes, "High altitude wind energy from a hybrid lighter-than-air platform using the magnus effect", in *Airborne Wind Energy*, 2013 (cit. on p. 31).
- [75] T. Pardal and P. Silva, "Analysis of experimental data of a hybrid system exploiting the magnus effect for energy from high altitude wind", in *Book of Abstracts of the International Airborne Wind Energy Conference 2015*, 2015 (cit. on p. 31).
- [76] I. Newton, "Letters to oldenburg", *Philosophical Transactions of the Royal Society*, 1671.7:3075–87, 1671 (cit. on p. 32).
- [77] B. Robins, "New principles of gunnery", 1805 (cit. on p. 32).
- [78] TokatyGA, "A history and philosophie of fluid mechanics", *Dover Publications*, 1994 (cit. on p. 32).
- [79] G. Magnus, "'über die abweichung der geschosse, und: Über eine abfallende erscheinung bei rotierenden körpern" (on the deviation of projectiles, and: On a sinking phenomenon among rotating bodies)", *The Borg/Luther Group, Naval Sea Systems Command Contract*, 1853. [Online]. Available: <http://gallica.bnf.fr/ark:/12148/bpt6k15173v.pleinepage.r=Annales+der+Physic.f13.langFR> (cit. on p. 32).
- [80] J. Seifert, "A review of the magnus effect in aeronautics", *Progress in Aerospace Sciences*, vol. 55, pp. 17–45, 2012 (cit. on pp. 32, 36).
- [81] C. K. G. L. Bergenson, "Sail assist developments 1979-1985", *Journal of Wind Engineering and Industrial Aerodynamics*, vol. 19, pp. 45–114, 1985 (cit. on pp. 34, 40).
- [82] L. Rayleigh, "On the irregular flight of a tennis ball", *Messenger of Mathematics*, 7:14, 1877 (cit. on p. 33).
- [83] H. Föttinger, "Neue grundlagen für die theoretische und experimentelle behandlung despropellerproblems", *Jahrbuch der Schiffbautechnischen Gesellschaft*, 1918 (cit. on p. 33).
- [84] Gumbel, "Modelle zur versinnbildlichung der wirbelgesetze", *Schiffbau*, 338–9, 1922 (cit. on p. 33).
- [85] [Online]. Available: <https://commons.wikimedia.org/w/index.php?curid=1456220> (cit. on p. 34).
- [86] [Online]. Available: https://en.wikipedia.org/wiki/Anton_Flettner (cit. on pp. 34, 35).

- [87] [Online]. Available: <https://en.wikipedia.org/wiki/Turbosail> (cit. on p. 34).
- [88] [Online]. Available: <http://www.shipspotting.com/gallery/photo.php?lid=1174824> (cit. on p. 35).
- [89] “Norse power”, [Online]. Available: <https://www.norsepower.com/> (cit. on pp. 35, 36).
- [90] [Online]. Available: https://en.wikipedia.org/wiki/E-Ship_1 (cit. on p. 36).
- [91] A. Sedaghat, “Magnus type wind turbines: Prospectus and challenges in design and modelling”, *Renewable Energy*, 619–628, 2014 (cit. on pp. 36, 37).
- [92] C. Badalamenti and S. Prince, “The effects of endplates on a rotating cylinder in cross flow”, in *26th AIAA Applied Aerodynamics Conf., Honolulu, Hawaii*, 2008 (cit. on pp. 36, 37, 41, 45–47).
- [93] B. K. S. Mittal, “Flow past a rotating cylinder”, *Fluid Mech.*, vol. 476, 303–334, 2003 (cit. on p. 39).
- [94] S. Kang, “Laminar flow over a steadily rotating circular cylinder under the influence of uniform shear”, *Phys. Fluids*, 2006 (cit. on p. 39).
- [95] S. T. X.K. Wang, “Near-wake flow characteristics of a circular cylinder close to a wall”, *Fluids Struct.*, 605–627, 2007 (cit. on p. 39).
- [96] T. T. D.B. Ingham, “A numerical investigation into the steady flow past a rotating circular cylinder at low and intermediate reynolds numbers”, *Comput. Phys.*, vol. 87, 91–107, 1990 (cit. on p. 39).
- [97] P. D. C. M. M. Badr S.C.R. Coutanceau, “Unsteady flow past a rotating circular cylinder at reynolds numbers 103 and 104”, *Fluid Mech.*, 459–484, 1990 (cit. on p. 39).
- [98] S. L. Y.T. Chew M. Cheng, “A numerical study of flow past a rotating cylinder using a hybrid vortex scheme”, *Fluid Mech.*, 35–71, 1995 (cit. on p. 39).
- [99] M. Chou, “Numerical study of vortex shedding from a rotating cylinder immersed in a uniform flow field”, *Numer. Methods Fluids*, 545–567, 2000 (cit. on p. 39).
- [100] U. C. T.M. Nair T.K. Sengupta, “Flow past rotating cylinders at high reynolds numbers using higher order upwind scheme”, *Comput. Fluids* 27, 47–70, 1998 (cit. on p. 39).
- [101] S. Karabelas, B. Koumroglou, C. Argyropoulos, and N. Markatos, “High reynolds number turbulent flow past a rotating cylinder”, *Applied Mathematical Modelling*, vol. 36, no. 1, pp. 379–398, 2012 (cit. on pp. 39, 40).
- [102] L. Prandtl, “The magnus effect and windpowered ships, naturwissenschaften”, vol. 13, 93–108, 1925 (cit. on pp. 39, 43).
- [103] P. D. P.T. Tokumaru, “Rotary oscillation control of cylinder wake, j. fluid mech.”, vol. 224, 77–90, 1991 (cit. on p. 39).
- [104] G. Schewe, “On the force fluctuations acting on a circular cylinder in crossflow from subcritical up to transcritical reynolds numbers”, *Fluid Mech.*, 265–285, 1983 (cit. on p. 39).

- [105] S. Karabelas, “Large eddy simulation of high-reynolds number flow past a rotating cylinder”, *Heat Fluid Flow*, 518–527, 2010 (cit. on p. 39).
- [106] M. L.-A. Da-Qing Li and B. Allenström, “Performance and vortex formation of flettner rotors at high reynolds numbers, 29th symposium on naval hydrodynamics gothenburg, sweden, 26-31 august 2012”, (cit. on p. 40).
- [107] C. P. A. De Marco* S. Mancini*, “Preliminary analysis for marine application of flettner rotors, proceedings of 2nd international symposium on naval architecture and maritime yıldız technical university, istanbul 23-24 october 2014”, (cit. on p. 40).
- [108] E. G. Reid, “Tests of rotating cylinders”, *NACA TN*, 1924 (cit. on pp. 40, 45–47).
- [109] L Bergeson, C. Greenwald, and T. Hanson, “Magnus rotor test and evaluation for auxiliary propulsion”, *The Ancient Interface*, vol. 13, p. 125, 1974 (cit. on pp. 40, 45–47).
- [110] C Badalamenti, “On the application of rotating cylinders to micro air vehicles”, 2010. [Online]. Available: http://openaccess.city.ac.uk/8693/1/On_the_Application_of_Rotating_Cylinders_to_Micro_Air_Vehicles.pdf (cit. on p. 41).
- [111] J Borg, “The magnus effect—an overview of its past and future practical applications”, *The Borg/Luther Group, Naval Sea Systems Command Contract*, no. 00024, 1986 (cit. on pp. 41–43, 45–47).
- [112] A. Thom, S. Sengupta, and J. Cormack, *Air torque on a cylinder rotating in an air stream*. HM Stationery Office, 1933 (cit. on p. 43).
- [113] A Betz, “Der magnuseffekt, die grundlage der flettner—walze”, *Zeitschrift des vereins deutscher Ingenieure*. Translated to: *The “Magnus Effect” The Principle of the Flettner rotor*. *NACA Technical Memorandum, TM-310*, pp. 9–14, 1925 (cit. on pp. 43, 45–47).
- [114] F. M. White, “Fluid mechanics”, 2011 (cit. on p. 44).
- [115] —, “Fluid mechanics. 5th”, *Boston: McGraw-Hill Book Company*, 2003 (cit. on p. 45).
- [116] E. Schmidt, M. D. Lellis, R. Saraiva, and A. Trofino, “State estimation of a tethered airfoil for monitoring, control, and optimization”, 2017 (cit. on pp. 48, 49).
- [117] M. Ranneberg, “Sensor setups for state and wind estimation for airborne wind energy converters”, *ArXiv preprint arXiv:1309.1029*, 2013 (cit. on p. 48).
- [118] D. Simon, “Kalman filtering with state constraints: A survey of linear and nonlinear algorithms”, *IET Control Theory & Applications*, vol. 4, no. 8, pp. 1303–1318, 2010 (cit. on p. 48).
- [119] Y. Gupta, J. Dumon, and A. Hably, “Modeling and control of a magnus effect-based airborne wind energy system in crosswind maneuvers”, *IFAC-PapersOnLine*, vol. 50, no. 1, pp. 13 878–13 885, 2017 (cit. on pp. 48, 71, 119).
- [120] M. Ahmed, A. Hably, and S. Bacha, “Kite generator system modeling and grid integration”, *IEEE Transactions on Sustainable Energy*, vol. 4, no. 4, pp. 968–976, Oct. 2013. [Online]. Available: <https://hal.archives-ouvertes.fr/hal-00873094> (cit. on p. 49).

- [121] R. Lozano, J. Dumon, A. Hably, and M. Alamir, “Energy production control of an experimental kite system in presence of wind gusts”, in *2013 IEEE/RSJ International Conference on Intelligent Robots and Systems (IROS)*, IEEE, Nov. 3–7, 2013, pp. 2452–2459 (cit. on p. 49).
- [122] A. Hably, J. Dumon, and G. Smith, “Control of an airborne wind energy system with a magnus effect”, in *American Control Conference (ACC), 2016*, IEEE, 2016, pp. 4978–4983 (cit. on pp. 49, 90).
- [123] A. Hably, J. Dumon, G. Smith, and P. Bellemain, “Control of a magnus effect-based airborne wind energy system”, in *Airborne Wind Energy: Advances in Technology Development and Research*, R. Schmehl, Ed. Springer Singapore, 2018, pp. 277–301. [Online]. Available: https://doi.org/10.1007/978-981-10-1947-0_12 (cit. on pp. 49, 54, 114).
- [124] S. Costello, G. François, and D. Bonvin, “Directional real-time optimization applied to a kite-control simulation benchmark”, pp. 1594–1601, 2015 (cit. on p. 61).
- [125] P. C. K. Robert E. Sheldahl, “Aerodynamic characteristics of seven symmetrical airfoil sections through 180-degree angle of attack for use in aerodynamic analysis of vertical axis wind turbines”, 1981 (cit. on p. 71).
- [126] I. Argatov, P. Rautakorpi, and R. Silvennoinen, “Estimation of the mechanical energy output of the kite wind generator”, *Renewable Energy*, vol. 34, pp. 1525–1532, 2009 (cit. on pp. 82, 94).
- [127] A. . S. R. . T. A. . L. . . De Lellis M. Mendonça, “Electric power generation in wind farms with pumping kites: An economical analysis”, *Renewable Energy, Elsevier*, vol. 86(C), pp. 163–172, (cit. on p. 90).
- [128] A. B. P. R. F. B. Maximilian Ranneberg David Wölflé and I. Bastigkeit, “Fast power curve and yield estimation of pumping airborne wind energy systems”, 2017 (cit. on pp. 90, 95).
- [129] F. Bauer, R. M. Kennel, C. M. Hackl, F. Campagnolo, M. Patt, and R. Schmehl, “Drag power kite with very high lift coefficient”, *Renewable Energy*, vol. 118, pp. 290–305, 2018. [Online]. Available: <http://www.sciencedirect.com/science/article/pii/S0960148117310285> (cit. on p. 90).
- [130] J. De Schutter, R. Leuthold, and M. Diehl, “Optimal control of a rigid-wing rotary kite system for airborne wind energy”, Mar. 2018 (cit. on p. 90).
- [131] C. L. Archer, “An introduction to meteorology for airborne wind energy”, U. Ahrens, M. Diehl, and R. Schmehl, Eds., pp. 81–94, 2013 (cit. on p. 91).
- [132] M. A. Tattersfield, J. F. Atwater, and C. P. Houle, *Method and system for harnessing wind energy using a tethered airfoil*, US Patent 9,046,072, 2015 (cit. on p. 98).
- [133] B. W. Roberts, D. H. Shepard, K. Caldeira, M. E. Cannon, D. G. Eccles, A. J. Grenier, and J. F. Freidin, “Harnessing high-altitude wind power”, *Energy Conversion, IEEE Transactions on*, vol. 22, no. 1, pp. 136–144, 2007 (cit. on p. 98).
- [134] VESTAS, “[Https://www.vestas.com/en/products/turbines](https://www.vestas.com/en/products/turbines)”, 2018 (cit. on p. 104).

-
- [135] windparka, “[Http://www.windparka15lingewaard.nl](http://www.windparka15lingewaard.nl)”, 2018 (cit. on p. 104).
- [136] E. Schmidt, Y. Gupta, J. Dumon, and A. Hably, “In-flight estimation of the aerodynamic characteristics of a magnuseffect-based awe system,renewable energy for developing countries, beirut, lebanon”, 2018 (cit. on p. 119).
- [137] Y. Gupta, J. Dumon, and A. Hably, “Power curve analysis of on-ground airborne wind energy systems,icit, 2019, 20th ieee- international conference of industrial technology, melbourne, australia”, (cit. on p. 119).